Equation of state of nuclear matter with applications to rapid rotating neutron stars

Koliogiannis Koutmiridis Polychronis

A dissertation submitted for the degree of
Doctor of Philosophy

Department of Nuclear and Elementary Particle Physics
Faculty of Sciences
Aristotle University of Thessaloniki
Thessaloniki, Greece
March, 2023

The implementation of the doctoral thesis was co-financed by Greece and the European Union (European Social Fund-ESF) through the Operational Programme «Human Resources Development, Education and Lifelong Learning» in the context of the Act “Enhancing Human Resources Research Potential by undertaking a Doctoral Research” Sub-action 2: IKY Scholarship Programme for PhD candidates in the Greek Universities.

Author: *Polychronis Koliogiannis Koutmiridis*
Supervisor: *Dr. Charalampos Moustakidis*

Η ΚΑΤΑΣΤΑΤΙΚΗ ΕΞΙΣΩΣΗ ΤΗΣ ΠΥΡΗΝΙΚΗΣ ΥΛΗΣ ΚΑΙ ΕΦΑΡΜΟΓΕΣ ΣΤΟΥΣ ΓΡΗΓΟΡΑ ΠΕΡΙΣΤΡΕΦΟΜΕΝΟΥΣ ΑΣΤΕΡΕΣ ΝΕΤΡΟΝΙΩΝ

Κολιογιάννης Κουτμηρίδης Πολυχρόνης

Διατριβή που υποβλήθηκε για το πτυχίο του
Διδάκτορα της Φιλοσοφίας

Τομέας Πυρηνικής Φυσικής και Φυσικής Στοιχειωδών Σωματιδίων
Σχολή Θετικών Επιστημών
Αριστοτέλειο Πανεπιστήμιο Θεσσαλονίκης
Θεσσαλονίκη, Ελλάδα
Μάρτιος, 2023

Η υλοποίηση της διδακτορικής διατριβής συγχρηματοδοτήθηκε από την Ελλάδα και την Ευρωπαϊκή Ένωση (Ευρωπαϊκό Κοινωνικό Ταμείο) μέσω του Επιχειρησιακού Προγράμματος «Ανάπτυξη Ανθρώπινου Δυναμικού, Εκπαίδευση και Δια Βίου Μάθηση», 2014-2020, στο πλαίσιο της Πράξης «Ενίσχυση του ανθρώπινου δυναμικού μέσω της υλοποίησης διδακτορικής έρευνας Υποδράση 2: Πρόγραμμα χορήγησης υποτροφιών ΙΚΥ σε υποψηφίους διδάκτορες των ΑΕΙ της Ελλάδας».

Ευρωπαϊκή Ένωση
Ευρωπαϊκό Κοινωνικό Ταμείο

Επιχειρησιακό Πρόγραμμα
Ανάπτυξη Ανθρώπινου Δυναμικού,
Εκπαίδευση και Διά Βίου Μάθηση
Με τη συγχρηματοδότηση της Ελλάδας και της Ευρωπαϊκής Ένωσης

ΕΣΠΑ 2014-2020
ανάπτυξη - εργασία - αλληλεγγύη

Συγγραφέας: *Πολυχρόνης Κολιογιάννης Κουτμηρίδης*
Επιβλέπων: *Δρ. Χαράλαμπος Μουστακίδης*

Information

A dissertation submitted for the degree of Doctor of Philosophy

Author: Polychronis Koliogiannis Koutmiridis

Supervisor: Dr. Charalampos Moustakidis

Dissertation Defense Committee

Advisory committee

- Dr. Charalampos Moustakidis
- Dr. Theodore Gaitanos
- Dr. George Lalazisis

Committee

- Dr. Charalampos Moustakidis
- Dr. Theodore Gaitanos
- Dr. George Lalazisis
- Dr. Anastasios Petkou
- Dr. Dennis Bonatsos
- Dr. George Souliotis
- Dr. Vlasios Petousis

Date of public defense: **March 6, 2023**

Committee	Position	Contact Information
Dr. Charalampos Moustakidis	Professor Department of Nuclear and Elementary Particle Physics Faculty of Sciences Aristotle University of Thessaloniki	moustaki@auth.gr
Dr. Theodore Gaitanos	Associate Professor Department of Nuclear and Elementary Particle Physics Faculty of Sciences Aristotle University of Thessaloniki	tgaitano@auth.gr
Dr. George Lalazisis	Emeritus Professor Department of Nuclear and Elementary Particle Physics Faculty of Sciences Aristotle University of Thessaloniki	glalazis@auth.gr
Dr. Anastasios Petkou	Professor Department of Nuclear and Elementary Particle Physics Faculty of Sciences Aristotle University of Thessaloniki	petkou@auth.gr
Dr. Dennis Bonatsos	Senior Researcher National Center for Scientific Research “Demokritos”	bonat@inp.demokritos.gr
Dr. George Souliotis	Professor Department of Chemistry National and Kapodistrian University of Athens	soulioti@chem.uoa.gr
Dr. Vlasios Petousis	Senior Researcher Department of experimental physics Institute of Experimental and Applied Physics Czech Technical University in Prague	vlasios.petousis@cern.ch

Πληροφορίες

Διατριβη που υποβληθηκε για το πτυχιο του Διδακτορα της Φιλοσοφιας

Συγγραφέας: Πολυχρόνης Κολιογιάννης Κουτμηρίδης

Επιβλέπων: Δρ. Χαράλαμπος Μουστακίδης

Επιτροπή υποστήριξης διατριβής

Τριμελής επιτροπή

- Δρ. Χαράλαμπος Μουστακίδης
- Δρ. Θεόδωρος Γαϊτάνος
- Δρ. Γεώργιος Λαλαζήσης

Επταμελής επιτροπή

- Δρ. Χαράλαμπος Μουστακίδης
- Δρ. Θεόδωρος Γαϊτάνος
- Δρ. Γεώργιος Λαλαζήσης
- Δρ. Αναστάσιος Πέτκου
- Δρ. Διονύσιος Μπονάτσος
- Δρ. Γεώργιος Σουλιώτης
- Δρ. Βλάσιος Πετούσης

Ημερομηνια δημοσιας υποστηριξης: Μάρτιος 6, 2023

Acknowledgements

I would like to express my deepest gratitude to my professor and supervisor, Dr. Charalampos Moustakidis, Professor at the Aristotle University of Thessaloniki, for his continuous guidance and academic and moral support throughout my doctoral studies. I am also thankful for the knowledge that he shared with me in the section of nuclear astrophysics and his suggestion for pursuing the subject of my doctoral dissertation. I appreciate his endless efforts for my financial support, the achievement of being accepted by I.K.Y. scholarship foundation, and his encouragement and help to participate in conferences. I could not have undertaken this journey without him.

I would like to sincerely thank the rest of my three-member committee members, Dr. Theodore Gaitanos and Dr. George Lalazisis, for their academic support and guidance. In addition, I would like to acknowledge the review committee members for their valuable comments and suggestions and for the time they dedicated to my dissertation.

Special thanks should also be mentioned to Professor Dr. Luciano Rezzolla for his useful comments and suggestion in my research, as well as for his invitation to present my work in the AstroCoffee seminars. Furthermore, through this seminar, I had the pleasure of knowing and working with Dr. Veronica Dexheimer. I would like to thank her for the longstanding conversations and our collaboration.

I would like to extend my sincere thanks to Dr. Chrysovalantis Margaritis and Alkiviadis Kanakis-Pegios for our fruitful collaboration and to Arsenia Chorozidou for our useful conversations and help in proofreading my dissertation.

I would like to acknowledge the financial support by the I.K.Y. Scholarship foundation under Act number MIS 5113934.

Lastly, I would like to thank my family for their patience and unconditional support in this long journey of my doctoral studies.

Abstract

Neutron stars manifest one of the Universe's densest objects, where matter is compressed at high densities, and nuclear physics combines with general relativity. The dense nuclear matter is described by the yet unknown equation of state, simulating the fluid interior, where its combination with the Tolman-Oppenheimer-Volkoff equations provides the neutron star structure. Although cold non-rotating neutron stars are a valuable source of constraints, temperature, and high rotational frequencies will significantly improve and extend our knowledge. In particular, the research is focused on the construction of both cold and hot, lepton-rich matter equations of state and their implications on macroscopic as well as microscopic quantities of neutron stars. Specifically, universal relations are produced for each representative case, and a criterion for the final fate of compact objects is extracted. Furthermore, the research is extended to proto-neutron stars and the hot and rapidly rotating remnant of a binary neutron star merger as insightful tools to provide constraints from the aspect of thermal and rotation effects. The former is directly related to neutron stars' internal structure and stability. Finally, the theoretical study of uniformly rotating neutron stars containing either cold or hot matter, and the observation of isolated or binary neutron stars, along with the present research, will shed light and provide constraints on the equation of state of dense nuclear matter.

Περίληψη

Οι αστέρες νετρονίων αποτελούν ένα από τα πιο πυκνά αντικείμενα του Σύμπαντος, όπου η πυρηνική φυσική συνδυάζεται με τη γενική θεωρία της σχετικότητας. Η πυκνή πυρηνική ύλη περιγράφεται από την άγνωστη ακόμη καταστατική εξίσωση, η οποία αναπαριστά την ύλη στο εσωτερικό του αστέρα και ο συνδυασμός της με τις εξισώσεις Tolman-Oppenheimer-Volkoff παρέχει τη δομή του αστέρα νετρονίων. Αν και οι ψυχροί μη περιστρεφόμενοι αστέρες νετρονίων είναι μια χρήσιμη πηγή περιορισμών, η θερμοκρασία και οι υψηλές περιστροφικές συχνότητες βελτιώνουν σημαντικά και επεκτείνουν το επίπεδο της γνώσης μας. Ειδικότερα, η έρευνα επικεντρώνεται στην κατασκευή τόσο ψυχρών όσο και θερμών, πλούσιων σε λεπτονική ύλη καταστατικών εξισώσεων και τις επιπτώσεις τους στα μακροσκοπικά και μικροσκοπικά μεγέθη που περιγράφουν τους αστέρες νετρονίων. Συγκεκριμένα, παράγονται καθολικές σχέσεις για κάθε αντιπροσωπευτική περίπτωση και εξάγεται ένα κριτήριο για το τελικό στάδιο των συμπαγών αντικειμένων. Επιπλέον, η έρευνα επεκτείνεται στους πρωταστέρες και στο θερμό και ταχέως περιστρεφόμενο υπόλειμμα μιας συγχώνευσης ενός δυαδικού συστήματος αστέρων νετρονίων, μια και αποτελούν ιδιαίτερα χρήσιμα μέσα για να εξάγουμε περιορισμούς με βάση την θερμοκρασία και την περιστροφή. Το προαναφερθέν σχετίζεται άμεσα με την εσωτερική δομή και τη σταθερότητα των αστέρων νετρονίων. Τέλος, η θεωρητική μελέτη ομοιόμορφα περιστρεφόμενων αστέρων νετρονίων, που περιέχουν είτε ψυχρή είτε θερμή ύλη, και η παρατήρηση μεμονωμένων ή δυαδικών αστέρων νετρονίων, μαζί με την παρούσα έρευνα ρίχνουν φως και παρέχουν περιορισμούς στην καταστατική εξίσωση της πυκνής πυρηνικής ύλης.

Εκτεταμένη Περίληψη

Η τέφρα των φωτεινών άστρων αποτελεί το τελικό στάδιο της αστρικής εξέλιξης και περιλαμβάνει λευκούς νάνους, αστέρες νετρονίων, καθώς και μελανές οπές. Όποιο από αυτά τα αντικείμενα σχηματιστεί στο τέλος της ζωής ενός φωτεινού αστέρα, το συμπαγές αυτό αντικείμενο θα ζήσει αμετάβλητο από την κατάσταση που σχηματίστηκε. Τα συμπαγή αστέρια διαφέρουν από τα συνηθισμένα, καθώς δεν καίνε πυρηνικά καύσιμα, επομένως δεν υποστηρίζονται από την θερμική πίεση ενάντια στην έλξη της βαρύτητας. Ειδικότερα, οι λευκοί νάνοι υποστηρίζονται από την πίεση εκφυλισμού των ηλεκτρονίων, οι αστέρες νετρονίων από τις απωστικές αλληλεπιδράσεις μεταξύ των νουκλεονίων, ενώ οι μελανές οπές είναι αστέρες που έχουν καταρρεύσει και δεν χρειάζεται ύλη για τη λύση τους. Επιπλέον, ενώ οι λευκοί νάνοι μπορούν να λάβουν διαφορετικές μορφές μόνο στα κυρίαρχα πυρηνικά είδη, οι αστέρες νετρονίων μπορούν να υποστηρίξουν διάφορες μορφές, όπως αστέρες που περιέχουν υπερόνια, παράξενη ύλη, ύλη κουάρκ καθώς και υβριδικοί αστέρες. Στην τελευταία περίπτωση, αυτή μιας μαύρης τρύπας, που είναι πιθανώς η μοίρα των μεγαλύτερων αστεριών, σχηματίζεται μια απρόσιτη περιοχή στον χωροχρόνο.

Στην περίπτωση των αστέρων νετρονίων, και οι τέσσερις θεμελιώδεις δυνάμεις (ισχυρή, αδύναμη, ηλεκτρομαγνητική, βαρύτητα) εμπλέκονται και αντιπροσωπεύουν έναν τρόπο για το σύμπαν να εκδηλώνει τα πιο πυκνά του αντικείμενα με εσωτερική δομή. Οι αστέρες νετρονίων βρίσκουν τη θέση τους ανάμεσα στα πιο εκπληκτικά αστροφυσικά αντικείμενα, καθώς συνδυάζουν την πυρηνική φυσική με τη γενική σχετικότητα. Η πρώτη εισάγει την καταστατική εξίσωση (ΚΕ), η οποία είναι υποχρεωτική για την περιγραφή του ρευστού στο εσωτερικό τους, ενώ η δεύτερη παρέχει τις εξισώσεις Tolman-Oppenheimer-Volfkoff (TOV) όπου εφαρμόζεται η ΚΕ. Ο συνδυασμός τους οδηγεί στην τελική δομή του αστέρα νετρονίων. Ωστόσο, πρέπει να τονιστεί ότι η ΚΕ είναι ακόμα άγνωστη, τόσο από θεωρητική όσο και από πειραματική άποψη. Η άγνωστη ΚΕ έχει σημαντική επίδραση στις ιδιότητες του αστέρα νετρονίων. Για να εξαλείψουμε την αβεβαιότητα της ΚΕ, βασιζόμαστε στα δεδομένα παρατήρησης τόσο μεμονωμένων αστέρων νετρονίων όσο και συγχωνεύσεων δυαδικών συστημάτων αστέρων νετρονίων, συστημάτων αστέρων νετρονίων-μαύρων τρυπών, εκρήξεων σουπερνόβα κλπ.

Η ύπαρξη αστεριών νετρονίων εξάγεται από την εμφάνιση εκρήξεων σουπερνόβα, καθώς και δυαδικών ακτίνων Χ όπου η εκπεμπόμενη ακτινοβολία, ως συνέπεια μιας ύλης που συσσωρεύεται από ένα συνοδό αστέρι, αποτελεί την αντίστοιχη ένδειξη. Η πρώτη παρατήρηση ενός αστέρα νετρονίων ήταν με τη μορφή ενός πάλσαρ, που είναι ένας ταχέως περιστρεφόμενος και εξαιρετικά μαγνητισμένος αστέρας νετρονίων. Αυτά τα αντικείμενα τροφοδοτούνται από ακτινοβολία μαγνητικής διπολικής ακτινοβολίας που προέρχεται από την ποσότητα της περιστροφικής ενέργειας που χάνεται.

Τα αστέρια νετρονίων μπορούν να θεωρηθούν ως γιγάντιοι πυρήνες με Ν περίπου 10^{57}. Ανατρέχοντας στη δομή του αστέρα νετρονίων, συναντάμε πέντε κύριες περιοχές, οι οποίες είναι: (α) ο εσωτερικός πυρήνας, (β) ο εξωτερικός πυρήνας, (γ) ο φλοιός, (δ) το περίβλημα και (ε) η ατμόσφαιρα (Lattimer, 2010, 2014). Ξεκινώντας την περιγραφή από τα εξωτερικά στρώματα, η ατμόσφαιρα ενός αστέρα νετρονίων έχει πάχος ~ 1 cm και ελέγχει την παρατηρούμενη φασματική κατανομή ενέργειας και τη διαμόρφωση του αναδυόμενου φάσματος φωτονίων. Προχωρώντας προς το εσωτερικό, συναντάμε τον φάκελο, όπου ο ρόλος του είναι

η θερμομόνωση. Στην πραγματικότητα, επηρεάζει τη μεταφορά και την απελευθέρωση της θερμικής ενέργειας από την επιφάνεια του αστέρα. Η θερμοκρασία του αστέρα ορίζεται μέσω της ιδιαίτερης σύνθεσης των στοιχείων του, δηλαδή τα αστέρια που έχουν ατμόσφαιρα αποτελούμενη από υδρογόνο φαίνονται πιο ψυχρά από εκείνα με περιβλήματα υψηλών στοιχείων. Οι προαναφερθείσες περιοχές περιέχουν ύλη με τη μορφή πλάσματος. Έπειτα, καθώς περάσουμε το φάκελο, εμφανίζεται ο φλοιός. Ο φλοιός εκτείνεται για $\sim 1-2$ km και σχηματίζεται κυρίως από πυρήνες. Για να είμαστε ακριβείς, τα κυρίαρχα είδη πυρήνων εξαρτώνται από την πυκνότητα. Συγκεκριμένα, κυμαίνεται από ^{56}Fe για ύλη με πυκνότητες μικρότερες από περίπου 10^6 g cm^{-3} έως πυρήνες με αριθμό μάζας περίπου 200. Το κλάσμα πρωτονίου στη διεπαφή φλοιού-πυρήνα σε $\mathrm{n} \sim \mathrm{n}_0/3$ (n_0, όπου το $\mathrm{n}_0 = 0.16$ fm^{-3} υποδηλώνει την πυκνότητα κορεσμού, απλώνεται μεταξύ των τιμών $(0.1-0.2)$. Σημειώνουμε εδώ ότι τέτοιοι εξαιρετικά «πλούσιοι» πυρήνες δεν μπορούν να παρατηρηθούν στο εργαστήριο, αλλά επιταχυντές σπάνιων ισοτόπων θα μπορούσαν ίσως να δημιουργήσουν κάποιους από αυτούς. Μετακινηνούμενοι δια μέσω του φλοιού, τη στιγμή που η πυκνότητα συναντά την πυκνότητα «neutron drip», $\mathrm{n_{nd}} = 4\ 10^{11}$ g cm^{-3} (όπου το χημικό δυναμικό νετρονίων είναι μηδέν), τα νετρόνια διαρρέουν από τους πυρήνες. Λαμβάνοντας υπόψη το τελευταίο, σε υψηλότερες πυκνότητες η πλειονότητα της ύλης βρίσκεται στο ρευστό νετρονίων. Φτάνοντας στη διεπιφάνεια φλοιού-πυρήνα, οι πυρήνες είναι τόσο στενά τοποθετημένοι που με έναν τρόπο εφάπτονται «εικονικά». Ωστόσο, θα μπορούσε να είναι σε χαμηλότερες πυκνότητες όπου το πυρηνικό πλέγμα γυρίζει «μέσα - έξω» και σχηματίζει ένα πλέγμα από κενά, τα οποία τελικά συμπιέζονται σε πυκνότητες κοντά σε n_0. Σε αρκετά υψηλές πυκνότητες, ξεκινώντας από $0.1\ \mathrm{n}_0$, εμφανίζονται οι λεγόμενες «φάσεις ζυμαρικών», όπου οι παραμορφώσεις γίνονται ακραίες και οι σφαιρικοί πυρήνες μετατρέπονται σε ράβδους ή πλάκες. Επιπλέον, σε αυτό το όριο, όπου η πυκνότητα είναι περίπου $\rho_\mathrm{s}/3$, με ρ_s περίπου ίσο με 3×10^{14} g cm^{-3} να είναι η πυκνότητα πυρηνικού κορεσμού, η ανομοιογενής φάση στους πυρήνες μετατρέπεται σε μια ομοιογενή φάση νουκλεονίων στον εξωτερικό πυρήνα. Επιπλέον, η ύλη είναι ουδέτερη ως προς το φορτίο, οδηγώντας σε ίσο αριθμό πρωτονίων και ηλεκτρονίων. Για μεγαλύτερες πυκνότητες από ρ_s, εκτός των πρωτονίων και των ηλεκτρονίων, εμφανίζονται τα μιόνια. Τέλος, λαμβάνοντας υπόψη τη σύνθεση του εσωτερικού πυρήνα, η υπάρχουσα γνώση περιέχει υψηλές αβεβαιότητες. Έτσι, θα μπορούσε να κυμαίνεται από μια προέκταση του εξωτερικού πυρήνα και να αποτελείται κυρίως από νουκλεόνια, ή θα μπορούσε να είναι ένα μείγμα νουκλεονίων και παράξενης ύλης με τη μορφή υπερονίων ή μη περιορισμένων κουάρκ. Ωστόσο, ορισμένες θεωρίες, σε ακραίες περιπτώσεις, υποδηλώνουν ότι τα νουκλεόνια μπορεί να δώσουν τη θέση τους εξ ολοκλήρου σε μη καθορισμένα κουάρκ στο κέντρο του άστρου, δημιουργώντας ένα πολύ διαφορετικό αστέρι.

Τα ακραία χαρακτηριστικά που διέπουν τα αστέρια νετρονίων τα τοποθετούν σε διαφορετικές φυσικές αρχές από τα υπόλοιπα αστέρια, οι οποίες απαιτούνται για την κατανόησή τους. Συγκεκριμένα, τα περισσότερα αστέρια μπορούν να περιγραφούν πλήρως στη Νευτώνεια Βαρύτητα λαμβάνοντας υπόψη την πυρηνική φυσική χαμηλής και ατομικής ενέργειας. Οι συνθήκες σε αυτή την περίπτωση είναι ουσιαστικά γνωστές στο εργαστήριο. Τα αστέρια νετρονίων ωθούν την ύλη σε τέτοιες ακραίες πυκνότητες που η πυρηνική και η σωματιδιακή φυσική είναι πράγματι απαραίτητες για την ακριβή περιγραφή τους. Η Νευτώνια υδροστατική ισορροπία, η οποία είναι επαρκής για τα περισσότερα αστέρια, αποτυγχάνει για τα αστέρια νετρονίων. Πιθανώς το μεγαλύτερο ελάττωμα είναι η αδυναμία πρόβλεψης ύπαρξης της μέγιστης μάζας. Επιπλέον, ο Laplace έδειξε ότι η ταχύτητα διαφυγής, $\sqrt{GM/R}$, θα μπορούσε τελικά να υπερβεί την ταχύτητα του φωτός, οδηγώντας στην ύψιστη σημασία των ορίων συμπαγότητας που περιγράφονται από τον ίδιο. Ωστόσο, η εισαγωγή της γενικής σχετικότητας, επέβαλε ένα όριο στη μάζα μαζί με ένα όριο για τη μέγιστη πυκνότητα μέσα σε οποιοδήποτε αστέρι νετρονίων. Με αυτό τον τρόπο, οδηγούμαστε σε ένα όριο για την τελική ενεργειακή πυκνότητα της ψυχρής βαρυονικής ύλης στο σύμπαν μας. Συμπερασματικά, η έντονη συγκέντρωση ύλης στα αστέρια νετρονίων μπορεί να περιγραφεί μόνο στη γενική σχετικότητα, τη θεωρία της βαρύτητας του Αϊνστάιν που από μόνη της περιγράφει τον τρόπο με τον οποίο η πιο αδύναμη δύναμη στη φύση οργανώνει την

κατανομή της μάζας και των συστατικών των πιο πυκνών αντικειμένων στο σύμπαν.

Η συνολική δομή των άστρων νετρονίων ελέγχεται μέσω της εξίσωσης TOV, όπως ήδη αναφέρθηκε. Η σύνθεσή τους δεν επηρεάζει τις προαναφερθείσες εξισώσεις. Συγκεκριμένα, οι εξισώσεις αστρικής δομής TOV που παρέχονται μέσω της γενικής σχετικότητας εκφράζονται ως

$$\frac{dP(r)}{dr} = -\frac{G\mathcal{E}(r)M(r)}{c^2r^2}\left(1+\frac{P(r)}{\mathcal{E}(r)}\right)\left(1+\frac{4\pi P(r)r^3}{M(r)c^2}\right)\left(1-\frac{2GM(r)}{c^2r}\right)^{-1}, \quad (1)$$

$$\frac{dM(r)}{dr} = \frac{4\pi r^2}{c^2}\mathcal{E}(r), \quad (2)$$

όπου P είναι η πίεση, $\mathcal{E}$, που ισούται με ρc^2, είναι η ενεργειακή πυκνότητα και M είναι η εσωτερική βαρυτική μάζα στην ακτίνα r. Ωστόσο, οι εξισώσεις TOV δεν μπορούν πάντα να παρέχουν φυσικές λύσεις. Για να έχουμε φυσικές λύσεις, αυτές οι εξισώσεις διέπονται από οριακές συνθήκες. Ειδικότερα,

- Για $r = 0$, όλοι οι όροι και η M είναι μηδέν,
- $P = 0$ στην επιφάνεια όπου $r = R_{\text{max}}$ και $M = M_{\text{max}}$.

Μία ΚΕ με τη μορφή $P(\mathcal{E})$, που προέρχεται από την πυρηνική φυσική, περιγράφοντας όλα τα στρώματα ενός αστέρα νετρονίων, υπαγορεύει μία μοναδική καμπύλη ακτίνας-μάζας. Δύο γενικά χαρακτηριστικά μπορούν να εξαχθούν: (α) είναι συνέπεια της γενικής σχετικότητας ότι η μέγιστη μάζα υπάρχει για οποιαδήποτε αιτιατή ΚΕ. Είναι ευρέως γνωστό ότι ο όρος *μέγιστη μάζα* δεν υπάρχει στη Νευτώνεια βαρύτητα και (β) η κλίση της καμπύλης μάζας-ακτίνας υπαγορεύεται από τη φύση της ΚΕ. Αυτό φαίνεται από την αδιάστατη ανάλυση των δομικών εξισώσεων, αγνοώντας φυσικά τους σχετικιστικούς όρους.

Ο προσδιορισμός της μέγιστης μάζας αστέρων νετρονίων είναι ένα μακροχρόνιο ζήτημα στην αστροφυσική, καθώς σχετίζεται άμεσα με την αναγνώριση μελανών οπών και την άγνωστη συμπεριφορά της πυρηνικής ύλης σε υψηλές πυκνότητες. Μέχρι αυτή τη στιγμή, η παρατήρηση μη/αργά περιστρεφόμενων αστεριών νετρονίων μας παρείχε σοβαρούς περιορισμούς στην πυκνή πυρηνική ύλη μέσω της μέγιστης δυνατής μάζας τους. Οι μετρήσεις με τη μεγαλύτερη μάζα αστεριών νετρονίων περιλαμβάνουν: (α) το PSR J1614-2230 ($M = 1.97 \pm 0.04\ M_\odot$) (Demorest et al., 2010) (ή από πρόσφατη επεξεργασία της παρατήρησης $M = 1.928 \pm 0.017\ M_\odot$ (Fonseca et al., 2016) και επίσης $M = 1.908 \pm 0.016 M_\odot$ (Arzoumanian et al., 2018)), (β) το PSR J0348+0432 ($M = 2.01 \pm 0.04\ M_\odot$) (Antoniadis et al., 2013), (γ) το PSR J0740+6620 ($M = 2.14^{+0.10}_{-0.09}\ M_\odot$) (Cromartie et al., 2019), και (δ) το PSR J2215+5135 ($M = 2.27^{+0.17}_{-0.15}\ M_\odot$) (Linares et al., 2018). Επιπλέον, υπάρχει μια λεπτομερής μελέτη σχετικά με τη συχνότητα περιστροφής των περιστρεφόμενων αστεριών νετρονίων (για μια ανασκόπηση βλέπε την Αναφορά (Patruno et al., 2017)). Το ταχύτερα περιστρεφόμενο πάλσαρ που έχει βρεθεί είναι το J1748-244ad με συχνότητα περιστροφής 716 Hz (Hessels et al., 2006). Ωστόσο, το ζήτημα παραμένει ανοιχτό: *γιατί δεν έχουμε παρατηρήσει πάλσαρ με υψηλότερες τιμές συχνότητας που προβλέπει η πλειονότητα των θεωρητικών μοντέλων;* Και ακόμη περισσότερο, *τι περιορίζει τις συχνότητες περιστροφής των πάλσαρ και γιατί;* (Prakash, 2015). Οι μελλοντικές μετρήσεις της ροπής αδράνειας (Bejger et al., 2005) και της συχνότητας Kepler μπορεί να είναι η απάντηση σε αυτά τα ερωτήματα βελτιώνοντας σημαντικά τις γνώσεις μας σχετικά με τις ιδιότητες των αστέρων νετρονίων στη μέγιστη περιστροφή.

Οι επιδράσεις της ΚΕ στις ιδιότητες των περιστρεφόμενων αστέρων νετρονίων (βλέπε Αναφορά (Paschalidis and Stergioulas, 2017; Stergioulas, 1998) για εισαγωγή και σχετική βιβλιογραφία) είχαν αρχίσει να κερδίζουν έδαφος σχεδόν πριν από 30 χρόνια από τους Shapiro, Teukolsky και τους συναδέλφους τους (Cook et al., 1992, 1994a,b,c; Shapiro et al., 1989). Σημαντική συμβολή σε αυτά τα ζητήματα είχε επίσης γίνει από τον Friedman και τους συναδέλφους του (Friedman and Ipser, 1987; Friedman et al., 1986, 1988, 1989; Koranda et al., 1997),

τον Haensel και τους συνεργάτες του (Haensel and Zdunik, 1989; Haensel et al., 1995, 1999; Lasota et al., 1996; Salgado et al., 1994a,b), καθώς και τον Glendenning και τους συνεργάτες του (Glendenning, 1992; Glendenning and Weber, 1994; Weber and Glendenning, 1991; Weber and Glendenning, 1992). Η ταχεία περιστροφή και τα αποτελέσματά της στην ΚΕ είχαν επίσης μελετηθεί στις Αναφορές (Abramowicz and Wagoner, 1978; Hashimoto et al., 1994; Iida and Sato, 1997; Lattimer et al., 1990; Lindblom, 1986; Shibata et al., 2000) και πιο πρόσφατα στις Αναφορές (Agrawal et al., 2008; Bejger et al., 2017; Benhar et al., 2005; Breu and Rezzolla, 2016; Chakrabarti et al., 2014a; Cipolletta et al., 2015, 2017; Dhiman et al., 2007; Haensel et al., 2008, 2009, 2016; Haskell et al., 2018; Krastev et al., 2008; Lo and Lin, 2011; Riahi et al., 2019; Zhang et al., 2013). Επιπλέον, στην πυρηνική αστροφυσική, οι θερμοί αστέρες νετρονίων σε συσχέτιση με την ταχεία περιστροφή είχαν μελετηθεί στην Αναφορά (Batra et al., 2018; Marques et al., 2017). Ακόμη, οι αστέρες νετρονίων σε μέγιστη περιστροφή σε τροποποιημένες θεωρίες βαρύτητας έχουν μελετηθεί λεπτομερώς από τον Κόκκοτα και τους συνεργάτες του (Doneva et al., 2013; Yazadjiev et al., 2015).

Στην παρούσα διατριβή, επεκτείνεται η προηγούμενη θεμελιώδης εργασία των Cook, Shapiro και Teukolsky (Cook et al., 1994b), καθώς και η πιο πρόσφατη εργασία των Cipolletta et al. (Cipolletta et al., 2015). Συγκεκριμένα, ένας μεγάλος αριθμός σύγχρονων ΚΕ οι οποίες, τουλάχιστον οριακά, προβλέπουν το ανώτερο όριο της μέγιστης μάζας αστέρων νετρονίων $M = 1.908 \pm 0.016\, M_{\odot}$ (Arzoumanian et al., 2018), ενώ παράλληλα αναπαράγονται με ακρίβεια οι μακροσκοπικές ιδιότητες της συμμετρικής πυρηνικής ύλης (για περισσότερες λεπτομέρειες βλέπε Αναφορά (Koliogiannis and Moustakidis, 2019)). Τα μοντέλα αυτών των ΚΕ είναι φαινομενολογικά, θεωρίας πεδίου και μικροσκοπικά. Στην κατηγορία των φαινομενολογικών μοντέλων, υπάρχουν τα: MDI (Moustakidis and Panos, 2009; Prakash et al., 1997), HHJ (Heiselberg and Hjorth-Jensen, 2000), Ska, SkI4 (Chabanat et al., 1997; Farine et al., 1997) και DH (Douchin and Haensel, 2001), στη θεωρία πεδίου, υπάρχουν τα: NLD (Gaitanos and Kaskulov, 2013, 2015) και W (Walecka, 1974) και στο μικροσκοπικό, υπάρχουν τα: HLPS (με βάση πυρηνικές αλληλεπιδράσεις που προέρχονται από τη χειραλική αποτελεσματική θεωρία πεδίου) (Hebeler et al., 2013), SCVBB (χρησιμοποιώντας το δυναμικό Argonne v18 συν δυνάμεις τριών σωμάτων που υπολογίζονται με το μοντέλο Urbana) (Sharma et al., 2015), BS (Balberg and Shapiro, 2000), BGP (σχετικιστική ανταλλαγή πιονίων) (Bowers et al., 1975), BL (Bombaci and Logoteta, 2018), WFF1,WFF2 (Wiringa et al., 1988) και PS (Pandharipande and Smith, 1975). Πρέπει να τονιστεί ότι η πλειονότητα των αναφερθέντων ΚΕ έχουν κατασκευαστεί για να αναπαράγουν τις μακροσκοπικές ιδιότητες της ομοιόμορφης συμμετρικής πυρηνικής ύλης και επίσης να επεκταθούν στην καθαρή ύλη νετρονίων. Η επέκταση στην ύλη του αστέρα νετρονίων πραγματοποιείται σε σχέση με τη βήτα ισορροπία. Όσον αφορά τον λεπτονικό βαθμό ελευθερίας, στα περισσότερα από αυτά θεωρείται ότι η κύρια συνεισφορά των λεπτονίων οφείλεται στα ηλεκτρόνια. Όλες οι χρησιμοποιούμενες ΚΕ περιγράφουν σωστά τον ρευστό πυρήνα ενός αστέρα νετρονίων. Θα πρέπει επίσης να σημειωθεί ότι λίγες από αυτές έχουν εφαρμοστεί αρχικά για τη μελέτη πεπερασμένων πυρήνων. Μεταξύ του αριθμού των εξισώσεων που χρησιμοποιούνται, έχουμε κατασκευάσει δύο ΚΕ, τις APR-1 και APR-2 (μικροσκοπικά μοντέλα) (Akmal et al., 1998), που προβλέπονται από το μοντέλο αλληλεπίδρασης που εξαρτάται από την ορμή (MDI). Αυτό το μοντέλο αναπαράγει τα αποτελέσματα των μικροσκοπικών υπολογισμών της συμμετρικής πυρηνικής ύλης και της ύλης αστέρων νετρονίων σε μηδενική θερμοκρασία με το πλεονέκτημα της επέκτασής του σε πεπερασμένη θερμοκρασία. Για την περιοχή στερεού φλοιού όλων των ΚΕ, χρησιμοποιούνται οι ΚΕ των Feynman, Metropolis and Teller (Feynman et al., 1949) καθώς και των Baym, Bethe και Sutherland (Baym et al., 1971).

Έγινε προσπάθεια να μελετηθούν συστηματικά οι περισσότερες από τις μακροσκοπικές ιδιότητες των ομοιόμορφα περιστρεφόμενων αστέρων νετρονίων στην ακολουθία Kepler (η ακολουθία στην οποία η κατάσταση μέγιστης μάζας αντιστοιχεί στη συχνότητα Kepler), συμπεριλαμβανομένης της μάζας, της πολικής και της ισημερινής ακτίνας, της γωνιακής ταχύτητας, της ροπή αδράνειας, της παραμέτρου Kerr, της εκκεντρότητας, του δείκτης πέδησης κλπ. Επιπλέον,

για λόγους πληρότητας και σύγκρισης, επειδή οι εφαρμόσιμες ΚΕ είναι αδρονικές, εισήχθει μία ΚΕ με εμφάνιση υπερονίων σε υψηλές πυκνότητες (FSU2H) (Tolos et al., 2017a) και μία κατάλληλη για να περιγράψει αστέρια κουάρκ με βάση το μοντέλο bag του MIT (QS57.6) (Glendenning, 2000; Haensel et al., 2007).

Επιπλέον, διερευνάται η δυνατότητα ενημέρωσης των προηγούμενων εμπειρικών καθολικών σχέσεων που συνδέουν την συχνότητα Kepler με τη μάζα και την ακτίνα στην κατάσταση μέγιστης μάζας. Μελετάμε συστηματικά την εξάρτηση της παραμέτρου Kerr από την ΚΕ και επίσης παρέχουμε την εξέλιξη της γωνιακής ορμής ενός αστέρα νετρονίων προκειμένου να εξετάσουμε την περίπτωση όπου αστέρια νετρονίων θεωρούνται πρόγονοι μελανών οπών. Συγκεκριμένα, εξετάζουμε (σύμφωνα με την ορολογία της Αναφοράς (Cook et al., 1994b)) δύο αλληλουχίες ισορροπίας περιστρεφόμενων αστέρων νετρονίων, *normal* και *supermassive*. Ενώ οι *normal* εξελικτικές ακολουθίες έχουν ένα σφαιρικό, μη περιστρεφόμενο (σταθερό) τελικό σημείο, οι *supramassive*, οι οποίες εξ ορισμού έχουν μάζες μεγαλύτερες από τη μέγιστη μάζα του μη περιστρεφόμενου αστέρα νετρονίων, δεν έχουν ένα σταθερό τελικό σημείο και κατά συνέπεια, η κατάρρευση σε μελανή οπή είναι αναπόφευκτη. Ωστόσο, πρέπει να σημειωθεί ότι η κατασκευή ακολουθιών *normal* και κυρίως *supramassive* είναι μια περίπλοκη διαδικασία στο πλαίσιο της γενικής σχετικότητας (Cook et al., 1994b).

Επιπροσθέτως, γίνεται συστηματική μελέτη της ροπής αδράνειας, μιας ποσότητας που παίζει σημαντικό ρόλο στις ιδιότητες των περιστρεφόμενων αστέρων νετρονίων, και της εκκεντρότητας που μπορεί να μας πληροφορήσει για την παραμόρφωσή τους. Ακολουθώντας την προηγούμενη εργασία των Lattimer και Prakash (Lattimer and Prakash, 2005), παρέχουμε ένα απόλυτο ανώτερο όριο της υψηλότερης πυκνότητας ψυχρής βαρυονικής ύλης στο Σύμπαν, με βάση το ανώτερο όριο που επιβάλλεται από τη μέγιστη μάζα ενός αστέρα νετρονίων. Στην πραγματικότητα, λαμβάνει χώρα μια προσπάθεια βελτίωσης του ορίου που εισήχθη στην Αναφορά (Lattimer and Prakash, 2005), με τη χρήση ενημερωμένων ΚΕ και συμπεριλαμβανομένης της περίπτωσης των αστεριών νετρονίων με τη μέγιστη περιστροφή. Κλείνοντας, εξετάζονται οι επιπτώσεις της ΚΕ στον δείκτη πέδησης των πάλσαρ. Εστιάζουμε κυρίως σε τιμές κοντά στην συχνότητα Kepler (70% και περισσότερο) όπου ο δείκτης πέδησης αρχίζει να επηρεάζεται από τη μάζα ηρεμίας.

Ωστόσο, η πρόσφατη παρατήρηση βαρυτικών κυμάτων από ένα συγχωνευόμενο δυαδικό σύστημα αστέρων νετρονίων (GW170817; Abbott et al. (Abbott et al., 2017)) εμφάνισε μια νέα, πολύ σημαντική πηγή για να διερευνήσουμε και να βελτιώσουμε τις γνώσεις μας για την ΚΕ με πολλούς τρόπους. Συγκεκριμένα, η ΚΕ τόσο της ψυχρής όσο και της θερμής πυρηνικής ύλης επηρεάζει σημαντικά τη δυναμική διαδικασία της φάσης πριν και μετά τη συγχώνευση των δυαδικών αστέρων νετρονίων, που οδηγούν σε ένα θερμό υπόλειμμα. Αυτή η διαδικασία περιλαμβάνει επίσης την παλιρροιακή πολωσιμότητα κατά την περιστροφή ενός δυαδικού συστήματος. Επιπλέον, μετά τη συγχώνευση, η μέγιστη ευσταθής μάζα, η περίοδος περιστροφής και η διάρκεια ζωής του υπολείμματος εξαρτώνται σε μεγάλο βαθμό από τις ιδιότητες της πυκνής ύλης σε υψηλή θερμοκρασία και εντροπία. Ειδικότερα, η εξέλιξη και το πιθανό τελικό στάδιο του υπολείμματος είναι ευαίσθητα στην ΚΕ, συμπεριλαμβανομένων (α) της χρονικής κλίμακας για τη βαρυτική κατάρρευση σε μια μελανή οπή, (β) της πιθανότητα μετάβασης φάσης σε άλλους βαθμούς ελευθερίας (υπερόνια, κουάρκ κλπ.), που μπορεί να οδηγήσουν σε κατάρρευση σε μελανή οπή και (γ) της δημιουργία ενός δίσκου γύρω από το υπόλλειμα, την εκτόξευση και την εκπομπή νετρίνων.

Τα προηγούμενα χρόνια, πρωτοποριακή έρευνα πραγματοποιήθηκε για τη μελέτη μιας θερμής ΚΕ για αστροφυσικές εφαρμογές, συμπεριλαμβανομένων των μελετών των Bethe et al. (Bethe et al., 1979), Brown et al. (Brown et al., 1982), Lamb et al. (Lamb et al., 1978), Lattimer & Ravenhall (Lattimer and Ravenhall, 1978) και Lattimer (Lattimer, 1981). Με την πάροδο των ετών, οι πιο χρησιμοποιημένοι ΚΕ της ύλης θερμών αστέρων νετρονίων ήταν (α) το μοντέλο υγρού τύπου σταγόνας που κατασκευάστηκε από τον Lattimer & Swesty (Lattimer and Swesty, 1991) και (β) αυτό από τους Shen et al. (Shen et al., 1998), όπου χρησιμοποιείται το σχετικιστικό μοντέλο μέσου πεδίου. Αργότερα, οι Shen et al. (Shen et al., 1998) επέκτεινε τη μελέτη τους

για να δημιουργήσει ΚΕ πυρηνικής ύλης για ένα ευρύ φάσμα θερμοκρασιών, πυκνοτήτων και κλασμάτων πρωτονίων για εφαρμογές σε σουπερνόβα, συγχωνεύσεις αστέρων νετρονίων και προσομοιώσεις σχηματισμού μελανών οπών χρησιμοποιώντας επίσης ένα πλήρες σχετικιστικό μέσο πεδίο (Shen et al. 2011).

Οι Wellenhofer et al. (Wellenhofer et al., 2015) ερεύνησαν την εξάρτηση από την πυκνότητα και τη θερμοκρασία της ελεύθερης συμμετρικής πυρηνικής ενέργειας χρησιμοποιώντας μικροσκοπικά πυρηνικά δυναμικά δύο και τριών σωμάτων που κατασκευάστηκαν από τη θεωρία πεδίου Chiral. Οι Constantinou et al. (Constantinou et al., 2014, 2015) παρήγαγαν μία θερμή ΚΕ κατάλληλη για να περιγράψει τις ιδιότητες των σουπερνόβα και των θερμών αστέρων νετρονίων. Οι επιδράσεις της θερμοκρασίας στην ΚΕ του αστέρα νετρονίων διερευνήθηκαν στο πλαίσιο της Θεωρίας του πεδίου Chiral από τους Sammarruca et al. (Sammarruca et al., 2020). Οι ιδιότητες της θερμής $\beta-$ευσταθούς πυρηνικής ύλης, χρησιμοποιώντας ΚΕ που προέρχονται από την προσέγγιση Brueckner-Hartree-Fock σε πεπερασμένη θερμοκρασία, έχουν παρασχεθεί σε μια σειρά εργασιών (Nicotra et al. (Nicotra et al., 2006); Burgio & Schulze (Burgio and Schulze, 2010); Baldo & Burgio (Baldo and Burgio, 2016); Fortin et al. (Fortin et al., 2018); Lu et al. (Lu et al., 2019), (Li et al., 2021); Figura et al. (Figura et al., 2020); Shang et al. (Shang et al., 2020); Wei et al. (Wei et al., 2020)). Οι Raithel et al. (Raithel et al., 2019) ανέπτυξαν ένα μοντέλο που επιτρέπει την επέκταση οποιουδήποτε ψυχρής νουκλεονικής ΚΕ, συμπεριλαμβανομένων των τμηματικών πολυτροπών ΚΕ, σε αυθαίρετη θερμοκρασία και κλάσματα πρωτονίων για χρήση σε υπολογισμούς και αριθμητικές προσομοιώσεις αστροφυσικών φαινομένων.

Περαιτέρω, μια λεπτομερής μελέτη της εξέλιξης των πρωταστέρων νετρονίων προβλέφθηκε από τους Pons et al. (Pons et al., 1999) και Prakash et al. (Prakash et al., 2001). Οι συγγραφείς εστίασαν στη θερμική και χημική εξέλιξη της γέννησης των αστέρων νετρονίων χρησιμοποιώντας συγκεντώσεις νετρίνων υπολογισμένες με συνέπεια με την υποκείμενη πυρηνική ΚΕ (Pons et al. (Pons et al., 1999)). Για μια πρόσφατη ανασκόπηση της θερμής ΚΕ της πυκνής ύλης και των αστέρων νετρονίων, δείτε Lattimer & Prakash (Lattimer and Prakash, 2016).

Τα τελευταία 40 χρόνια, αρκετή θεωρητική έρευνα έχει αφιερωθεί στη μελέτη των διαδικασιών των φάσεων συγχώνευσης και μετά τη συγχώνευση ενός συστήματος δυαδικού αστέρα νετρονίων, και έχει επιτευχθεί σημαντική πρόοδος. Ωστόσο, υπάρχουν πολλά σχετικά ζητήματα που παραμένουν άλυτα ή τουλάχιστον υπό εξέταση. Γενικά, η αναφορά στην εξέλιξη του υπολείμματος περιλαμβάνει κυρίως τον χρόνο κατάρρευσης και τη μάζα κατωφλίου. Επιπλέον, η πιθανότητα μετάβασης φάσης στο εσωτερικό του υπολείμματος μπορεί να επηρεάσει το σήμα των εκπεμπόμενων βαρυτικών κυμάτων. Ακόμη, θέματα που εξετάζονται είναι επίσης οι ιδιότητες εκτόξευσης δίσκου και εκπομπής νετρίνων, οι οποίες είναι ευαίσθητες στη χρησιμοποιούμενη ΚΕ (για εκτεταμένη συζήτηση και εφαρμογές, βλέπε Perego et al. (Perego et al., 2019)). Ορισμένες προηγούμενες εργασίες περιλαμβάνονται επίσης στους Bauswein et al. (Bauswein et al., 2010), Kaplan et al. (Kaplan et al., 2014), Tsokaros et al. (Tsokaros et al., 2020), Yasin et al. (Yasin et al., 2020), Radice et al. (Radice et al., 2020), Sarin και Sen (Sen, 2020).

Αξίζει να αναφέρουμε ότι η θεωρία της κβαντικής χρωμοδυναμικής (QCD) προβλέπει τη συνεχιζόμενη μετάβαση της αδρονικής ύλης σε με περιορισμένη ύλη κουάρκ σε αρκετά υψηλή πυκνότητα (λίγες φορές την πυκνότητα κορεσμού). Καθώς τα αστέρια νετρονίων παρέχουν ένα πλούσιο πεδίο δοκιμών για μικροσκοπικές θεωρίες πυκνής πυρηνικής ύλης, ο συνδυασμός αυτής της μελέτης με τα πειραματικά δεδομένα από υπερσχετικιστικές συγκρούσεις βαρέων ιόντων (ο Σχετικός Επιταχυντής Βαρέων Ιόντων στο Brookhaven και ο Μεγάλος Επιταχυντής Αδρονίων στο CERN) μπορεί να βοηθήσει σημαντικά στη βελτίωση των γνώσεων μας για τη θεωρία QCD (Baym et al. (Baym et al., 2018)). Ωστόσο, το πρόβλημα της ύπαρξης ελεύθερης ύλης κουάρκ στο εσωτερικό των αστέρων νετρονίων παραμένει. Επιπλέον, η εμφάνιση περίεργων αδρονίων (υπερονίων, κλπ.) περίπου στη διπλάσια πυκνότητα κορεσμού οδηγεί σε μια αξιοσημείωτη ομαλότητα της ΚΕ και σε χαμηλές τιμές μάζας αστέρων νετρονίων, μακριά από την παρατήρηση. Αυτό το πρόβλημα επισημαίνεται ως το παζλ υπερονίων. Φυσικά, υπάρχουν και άλλες μελέτες όπου οι συγγραφείς δήλωσαν ότι η θεώρηση του υπερονίου στην ΚΕ δεν έρχεται σε αντίθεση με

τις προβλέψεις μιας πολύ υψηλής μάζας αστέρα νετρονίων (βλέπε Chatterjee & Vidana (Chatterjee and Vidaña, 2016); Li et al. (Li et al., 2020)).

Πρόσφατα, υποστηρίχθηκε ότι η πρόσφατη παρατήρηση βαρυτικών κυμάτων από συγχωνεύσεις αστέρων νετρονίων θα μπορούσε να ρίξει φως στην πιθανότητα των αδρονίων να κινούνται σε μια μετάβαση φάσης κουάρκ (Annala et al. (Annala et al., 2020)). Οι συγγραφείς δήλωσαν ότι εάν το σύμμορφο όριο στην τιμή της ταχύτητας του ήχου, $c_s/c \leq 1/\sqrt{3}$, δεν παραβιαστεί έντονα, τότε οι βαρείς αστέρες νετρονίων μπορεί να έχουν μεγάλους πυρήνες κουάρκ. Σε αυτήν την περίπτωση, πρέπει να ληφθούν υπόψη σημαντικές επιπτώσεις σε συγχωνεύσεις αστέρων νετρονίων με τουλάχιστον έναν τεράστιο συμμετέχοντα (Annala et al. (Annala et al., 2020)). Ωστόσο, στην παρούσα έρευνα, η περίπτωση πρόσθετων βαθμών ελευθερίας (υπερόνια, κουάρκ κλπ.) στο εσωτερικό των αστέρων νετρονίων δεν εξετάζεται.

Ως συνέχεια, πραγματοποιείται η διερεύνηση των μακροσκοπικών ιδιοτήτων της θερμής πυρηνικής ύλης και αστέρων νετρονίων. Συγκεκριμένα, εφαρμόζουμε ένα μοντέλο αποτελεσματικής αλληλεπίδρασης που εξαρτάται από την ορμή (MDI), όπου τα θερμικά αποτελέσματα μπορούν να μελετηθούν ταυτόχρονα στο κινητικό μέρος της ενέργειας και στην αλληλεπίδραση. Το πλεονέκτημα του παρόντος μοντέλου, σε σύγκριση με άλλα, είναι ότι τα θερμικά φαινόμενα εισάγονται με αυτοσυνεπή τρόπο. Ειδικότερα, εφαρμόζουμε αυστηρά τους θερμοδυναμικούς νόμους που περιγράφουν την θερμή πυκνή πυρηνική ύλη. Επιπλέον, αυτό το μοντέλο μπορεί να επεκταθεί προκειμένου να τροποποιηθεί η ακαμψία της προτεινόμενης ΚΕ παραμετροποιώντας σωστά την συμμετρική πυρηνική ενέργεια. Αξίζει να σημειωθεί ότι ένας μεγάλος αριθμός ΚΕ θερμής πυρηνικής ύλης και αστέρων νετρονίων για αστροφυσικές εφαρμογές έχουν εμφανιστεί με την πάροδο των ετών, χρησιμοποιώντας διάφορα θεωρητικά μοντέλα και προσεγγίσεις. Ωστόσο, τα περισσότερα από αυτά είναι αμφισβητήσιμα με την έννοια ότι τα θερμικά φαινόμενα δεν περιλαμβάνονται στην ψυχρή ΚΕ με αυτοσυνεπή τρόπο αλλά μάλλον με τεχνητό. Αυτό το σημείο έχει ήδη σημειωθεί στους Constantinou et al. (Constantinou et al., 2015). Στην πραγματικότητα, το παρόν μοντέλο εισήχθη από τους Gale et al. (Gale et al., 1987) προκειμένου να εξεταστεί η επίδραση του MDI στη ροή ορμής των συγκρούσεων βαρέων ιόντων. Ωστόσο, με την πάροδο των ετών, το μοντέλο έχει εφαρμοστεί εκτενώς για τη μελέτη των ιδιοτήτων της ψυχρής και θερμής πυρηνικής ύλης και αστέρων νετρονίων (για μια ανασκόπηση του μοντέλου, βλέπε Prakash et al. (Prakash et al., 1997); Li & Schr öder (Li and Schröder, 2001); Li et al. (Li et al., 2008)).

Κατόπιν, παράγεται ένα σύνολο θερμοδυναμικά ευσταθών ισοθερμικών και ισεντροπικών ΚΕ, με βάση το παραμετροποιημένη ψυχρή ΚΕ. Ο τελικός μας σκοπός είναι η εφαρμογή των προβλεπόμενων ΚΕ για μια εκτενή μελέτη σχετικά με τις μακροσκοπικές ιδιότητες (συμπεριλαμβανομένης κυρίως της μάζας και της ακτίνας, της ροπής αδράνειας, της παραμέτρου Kerr, κλπ.) τόσο σε μη περιστρεφόμενο όσο και σε περιστρεφόμενο στη συχνότητα Kepler αστέρα νετρονίων, καθώς και σε πρωταστέρες και υπολείμματα συγχώνευσης αστέρων νετρονίων. Δίνουμε ιδιαίτερη προσοχή στις ακολουθίες σταθερής βαρυονικής μάζας και εξετάζουμε τον ιδιότυπο ρόλο της παραμέτρου Kerr. Τέλος, αφιερώνουμε ένα μέρος για τη μελέτη μερικών διαδικασιών μετά τη συγχώνευση, όπως το θερμό, ταχέως περιστρεφόμενο υπόλειμμα και η μάζα κατωφλίου, και τα συνδέουμε με τις προκύπτουσες ΚΕ.

Τέλος, η έρευνα επικεντρώνεται στην ευστάθεια των σχετικιστικών αστέρων που έχει μελετηθεί εκτενώς στο παρελθόν (Chandrasekhar, 1964a,b; Friedman and Stergioulas, 2013; Glendenning, 2000; Haensel et al., 2007; Harrison et al., 1965; Shapiro and Teukolsky, 1983; Weinberg, 1972; Zeldovich and Novikov, 1978), όπου έχουν χρησιμοποιηθεί διάφορες προσεγγίσεις για την αντιμετώπιση αυτού του προβλήματος (Bardeen et al., 1966). Συγκεκριμένα, μπορούν πρώτα να λυθούν οι εξισώσεις TOV (Oppenheimer and Volkoff, 1939; Tolman, 1939) (οι οποίες παρέχουν τη διαμόρφωση ευστάθειας) είτε για αριθμητικές ΚΕ είτε για την προσπάθεια εύρεσης αναλυτικών λύσεων. Σε κάθε περίπτωση, και οι δύο λύσεις οδηγούν σε άπειρο αριθμό καταστάσεων. Δεύτερον, μια πιθανότητα είναι η χρήση του κριτηρίου του Chandrasekhar (Chandrasekhar, 1964a,b) προκειμένου να προσδιοριστεί, σε κάθε περίπτωση, η ευσταθής κατάσταση καθώς και

η διεπαφή μεταξύ ευσταθούς και ασταθούς κατάστασης.

Αξίζει να σημειωθεί ότι για να εξαγάγουμε μια λύση με φυσικό ενδιαφέρον, πρέπει να λύσουμε τις εξισώσεις πεδίου του Αϊνστάιν χρησιμοποιώντας μια ρεαλιστική ΚΕ του εσωτερικού ρευστού. Ωστόσο, υπάρχουν μερικές αναλυτικές λύσεις με φυσικό ενδιαφέρον που μπορεί να βοηθήσουν στην εισαγωγή και την καθιέρωση κάποιων καθολικών προσεγγίσεων.

Επιπλέον, σε μια δεδομένη πυκνότητα, υπάρχει μια σημαντική παράμετρος που ονομάζεται αδιαβατικός δείκτης και συγκεκριμένα, χαρακτηρίζει την ακαμψία ΚΕ (Bludman, 1973a,b; Gaertig and Kokkotas, 2009; Glass and Harpaz, 1983; Haensel et al., 2007; Harrison et al., 1965; Hiscock and Lindblom, 1983; Ipser, 1970; Lindblom and Detweiler, 1983; Misner et al., 1973). Το κριτήριο αστάθειας του Chandrasekhar (Chandrasekhar, 1964a,b), εξαρτάται σε μεγάλο βαθμό από αυτήν την παράμετρο (αδιαβατικός δείκτης). Ένα από τα κύρια κίνητρα της παρούσας εργασίας είναι να εξετάσει τη δυνατότητα επιβολής περιορισμών στις ρεαλιστικές ΚΕ των αστέρων νετρονίων μέσω της συνθήκης αστάθειας του Chandrasekhar.

Συγκεκριμένα, χρησιμοποιείται μια εκτεταμένη ομάδα ρεαλιστικών ΚΕ που βασίζονται σε διάφορα θεωρητικά πυρηνικά μοντέλα. Τα συντομευμένα ονόματα αυτών των εξισώσεων κατάστασης είναι: MDI (Moustakidis and Panos, 2009; Prakash et al., 1997), NLD (Gaitanos and Kaskulov, 2013, 2015), HHJ (Heiselberg and Hjorth-Jensen, 2000), Ska, SkI4 Chabanat et al. (1997); Farine et al. (1997), HLPS (Hebeler et al., 2013), SCVBB (Sharma et al., 2015), BS (Balberg and Shapiro, 2000), BGP (Bowers et al., 1975), W (Walecka, 1974), DH (Douchin and Haensel, 2001), BL (Bombaci and Logoteta, 2018), WFF1, WFF2 (Wiringa et al., 1988), APR (Akmal et al., 1998) και PS (Pandharipande and Smith, 1975). Όλα αυτά ικανοποιούν, τουλάχιστον οριακά, το παρατηρούμενο όριο των $M = 1.97 \pm 0.04\ M_{\odot}$ (PRS J1614-2230 (Demorest et al., 2010)) και $M = 2.01 \pm 0.04\ M_{\odot}$ (PSRJ0348+0432 (Antoniadis et al., 2013)). Στην πραγματικότητα, αυτή τη στιγμή, οι πιο ισχυροί περιορισμοί στις ΚΕ των αστέρων νετρονίων βασίζονται στις μετρήσεις του κατώτερου ορίου της μέγιστης μάζας τους. Αυστηρά μιλώντας, οι προτεινόμενες ΚΕ που δεν αναπαράγουν την υψηλότερη μέτρηση της μάζας των αστέρων νετρονίων, πρέπει να αποκλειστούν.

Η παρούσα έρευνα επικεντρώνεται στην εξάρτηση του αποτελεσματικού κρίσιμου αδιαβατικού δείκτη από τους συμπαγής αστέρες νετρονίων, για κάθε ΚΕ. Εστιάζουμε κυρίως στη διεπαφή μεταξύ ευσταθούς και ασταθούς καταστασης που αντιστοιχεί στην κατάσταση μέγιστης μάζας. Αυτή η περιοχή είναι πολύ σημαντική αφού σχετίζεται άμεσα με το τμήμα υψηλής πυκνότητας της ΚΕ του αστέρα νετρονίων. Αυτό το ζήτημα παραμένει ένα ανοιχτό πρόβλημα. Επιπλέον, προτείνουμε μια πρόσθετη μέθοδο για τον περιορισμό των ΚΕ με τη βοήθεια ακριβών μετρήσεων της μέγιστης μάζας ή/και συμπαγότητας αστέρων νετρονίων. Τέλος, κάνουμε μια προσπάθεια να συσχετίσουμε τη μέγιστη συχνότητα περιστροφής $f_{\rm max}$ με τον κρίσιμο αδιαβατικό δείκτη και τις μακροσκοπικές ιδιότητες που αντιστοιχούν στη κατάσταση μέγιστης μάζας ενός μη περιστρεφόμενου (στατικού) αστέρα νετρονίων (συμπεριλαμβανομένης της μέγιστης μάζας $M^{\rm stat}_{\rm max}$, της αντίστοιχης ακτίνας $R^{\rm stat}_{\rm max}$ και της παραμέτρου συμπαγότητας $\beta^{\rm stat}_{\rm max}$) έτσι ώστε να υποδείξουμε πώς οι παρατηρήσιμες μετρήσεις αστέρων νετρονίων με υψηλή περιστροφή μπορεί να επιβάλλουν περιορισμούς στην ΚΕ.

Contents

CHAPTER 1

Introduction

The ashes of luminous stars are the endpoint of stellar evolution and comprise white dwarfs, neutron stars, as well as black holes. Whichever of these objects is formed at the end of the life of a luminous star, the compact object will live unchanged from the state that was formed. Compact stars are different from ordinary stars, considering that they do not burn nuclear fuels, so they are not supported by thermal pressure against the pull of gravity. In particular, white dwarfs are supported by the degeneracy pressure of electrons, neutron stars by the repulsive interactions between nucleons, and black holes are collapsed objects where no matter is needed for their solution. Additionally, while white dwarfs can take different forms only in the dominant nuclear species, neutron stars can support several forms, including hyperon, hybrid, strange, and quark matter. In the last case, that of a black hole, which is probably the fate of the most massive stars, an inaccessible region in spacetime is formed (Glendenning, 2000; Weber, 1996, 1999).

In the particular case of neutron stars, all four fundamental forces (strong, weak, electromagnetic, gravity) involve and represent a way for the universe to manifest its densest objects with an internal structure. Neutron stars find their position among the most amazing astrophysical objects as they combine nuclear physics with general relativity (for a shematic presentation of neutron star formations see Figure 1.1). The former introduces the equation of state (EoS), which is mandatory for describing the fluid interior. At the same time, the final provides the Tolman-Oppenheimer-Volfkoff (TOV) equations where the EoS is applied. Their combination leads to the ultimate neutron star structure. However, it must be stressed that the EoS is still unknown, both from a theoretical and an experimental point of view. The unknown EoS has a significant effect on the bulk neutron star properties. To eliminate the uncertainty of the EoS, we rely on the observational data of isolated neutron stars and binary neutron star mergers, neutron star-black hole systems, supernova explosions, etc.

The existence of neutron stars is inferred by the occurrence of supernova explosions and X-ray binaries where the emitted radiation, as a consequence of a matter accreted from a companion star, provides an indicator. The first observation of a neutron star was in the form of a pulsar, which is a rapidly rotating and highly magnetized neutron star. These objects are powered by beamed magnetic dipole radiation stemming from the amount of lost rotational energy. In particular, the brief history of the discovery to observation is (Lattimer, 2015)

- **1920**: Rutherford predicts the existence of the neutron.
- **1931**: Landau anticipates single-nucleus stars.
- **1932**: Chadwick discovers the neutron.
- **1934**: W. Baade and F. Zwicky (Baade and Zwicky, 1934) suggest that neutron stars are the end product of supernovae.

- **1939**: Oppenheimer and Volkoff (Oppenheimer and Volkoff, 1939) find that general relativity predicts a maximum mass for neutron stars.
- **1964**: Hoyle, Narlikar and Wheeler (Hoyle et al., 1964) predict that neutron stars rotate rapidly.
- **1965**: Hewish and Okoye (Hewish and Okoye, 1965) discover an intense radio source in the Crab nebulae, later shown to be a neutron star.
- **1966**: Colgate and White (Colgate and White, 1966) perform simulations of core-collapse supernovae resulting in formation of neutron stars.
- **1967**: C. Schisler discovers a dozen pulsing radio sources, including the Crab, using classified military radar. He revealed his discoveries in 2007. Later in 1967 Hewish, Bell, Pilkington, Scott and Collins (Hewish et al., 1968) discover PSR 1919+21 (Hewish receives 1974 Nobel Prize).
- **1968**: Crab pulsar discovered (Piddington, 1969) and pulse period found to be increasing, characteristic of spinning stars but not binaries or vibrating stars. This also clinched the connection with supernovae. The term "pulsar" first appears in print in the Daily Telgraph.
- **1969**: "Glitches" observed (Radhakrishnan and Manchester, 1969; Reichley and Downs, 1969), providing evidence for superfluidity in the neutron star crust (Baym et al., 1969).
- **1971**: Accretion powered X-ray pulsars discovered by the Uhuru satellite (Giacconi et al., 1971).
- **1974**: The first binary pulsar, PSR 1913+16, discovered by Hulse and Taylor (Hulse and Taylor, 1975) (Nobel Prize 1993). It's orbital decay is the first observation (Taylor et al., 1979) proving existence of gravitational radiation. Lattimer and Schramm (Lattimer and Schramm, 1974) suggest decompressing neutron star matter from merging compact binaries leads to synthesis of r-process elements.

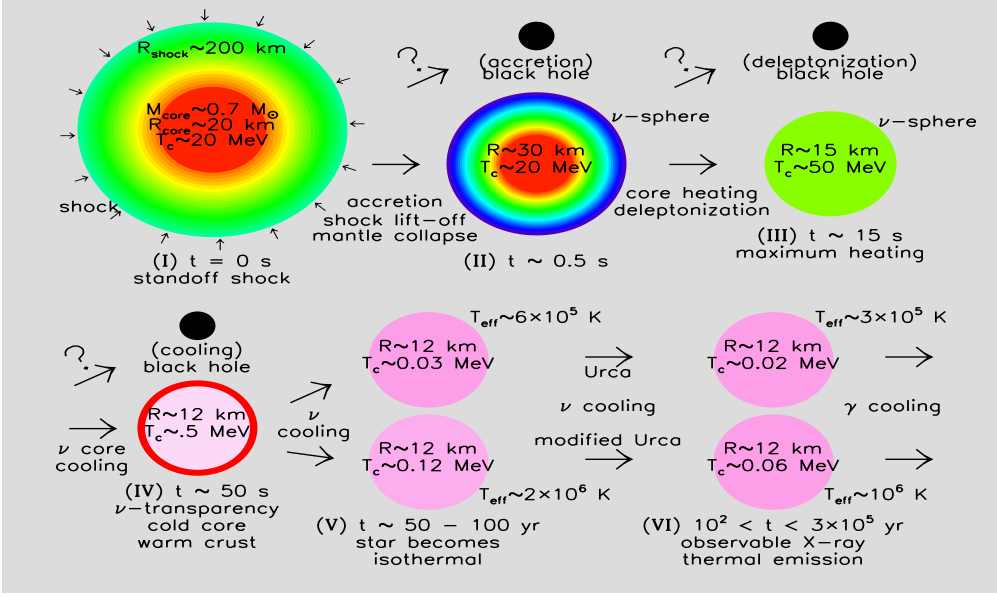

Figure 1.1: The main stages of evolution of a neutron star (Lattimer and Prakash, 2004).

- **1982**: The first millisecond pulsar, PSR B1937+21, discovered by Backer et al. (Backer et al., 1982)
- **1996**: Discovery of the closest neutron star RX J1856-3754 by Walter et al. (Walter et al., 1996).
- **1998**: Kouveliotou et. al. discovers the first magnetar (Kouveliotou et al., 1998).

Neutron stars can be considered giant nuclei with N about 10^{57}. Delving into the neutron star structure, we come across five major regions, that are: (a) the inner core, (b) the outer core, (c) the crust, (d) the envelope, and (e) the atmosphere (Lattimer, 2010, 2014). Starting the description from the outer layers, the atmosphere of a neutron star has a thickness of $\sim$ 1 cm, controls the observed spectral energy distribution, and shapes the emergent photon spectrum. Moving inside, we meet the envelope, whose role is thermal insulation. It influences the transport and release of thermal energy from the star's surface at a crucial level. Actually, the star's temperature is defined through the particular composition of its elements, i.e., stars with a hydrogenic atmosphere appear cooler than those with heavy-element envelopes. The regions mentioned above contain matter in the form of plasma. Afterward, when we pass through the envelope, the crust appears. The crust extends for $\sim 1-2$ km and is primarily formed by nuclei. To be accurate, the dominant species of nuclei depend on the density. Specifically, it ranges from ^{56}Fe for matter with densities less than about 10^6 g cm^{-3} to nuclei with mass number about 200. The proton fraction at the crust-core interface at n $\approx$ n$_0/3$, where n$_0 = 0.16$ fm^{-3} denotes the saturation density, spreads between the values $(0.1 - 0.2)$. We note here that such extremely "rich" nuclei cannot be observed in the laboratory, but rare-isotope accelerators could create some of them. As we move through the crust, at the time the density meets the "neutron-drip" density, n$_{\rm nd} = 4 \times 10^{11}$ g cm^{-3} (where the neutron chemical potential is zero), neutrons leak out of nuclei. Considering the latter, at higher densities, most matter resides in the neutron fluid. Reaching the crust-core interface, nuclei are so closely packed that, in a way, they "virtually" touching. However, it could be at lower densities that the nuclear lattice turns "inside-out" and forms a lattice of voids, which eventually squeezed out at densities near n$_0$. At high enough densities, starting at 0.1 n$_0$, the so-called "pasta phases" appear, where deformations become extreme and spherical nuclei transform into rods or plates. Furthermore, at this boundary, where the density is roughly $\rho_{\rm s}/3$, with $\rho_{\rm s}$ approximately equal to 3×10^{14} g cm^{-3} being the nuclear saturation density, the inhomogeneous phase with nuclei transforms to a homogeneous phase of nucleons in the outer core. In addition, the matter is charge-neutral, leading to an equal number of protons and electrons. In addition to protons and electrons, muons appear for higher densities than ρ_s. Finally, considering the inner core's composition, the existing knowledge contains high uncertainties. Thus, it could range from an extension of the outer core and be primarily nucleonic, or it could be a mixture of nucleons and strange matter in the form of hyperons or deconfined quarks. Nevertheless, in extreme cases, some theories suggest that nucleons may entirely give their place to deconfined quarks at the star's center, creating a vastly different star. The schematic presentation of the internal neutron star structure is displayed in Figure 1.2.

The extreme characteristics that rule neutron stars place them in a different physical principles ground, which are required for their understanding than the rest of stars. In particular, most of the stars can be fully described in Newtonian Gravity, considering the low-energy and atomic nuclear physics. The conditions, in this case, are essentially known in the laboratory. Neutron stars push matter to such extremes of density that nuclear and particle physics are necessary for their accurate description. Newtonian hydrostatic equilibrium, which is adequate for most stars, breaks down for neutron stars. Probably the biggest defect is the inability to predict the existence of the maximum mass. In addition, Laplace demonstrated that the escape velocity, $\sqrt{GM/R}$, could eventually exceed the speed of light. The former led to the utmost importance of compactness limits described by Laplace. However, the introduction of general relativity

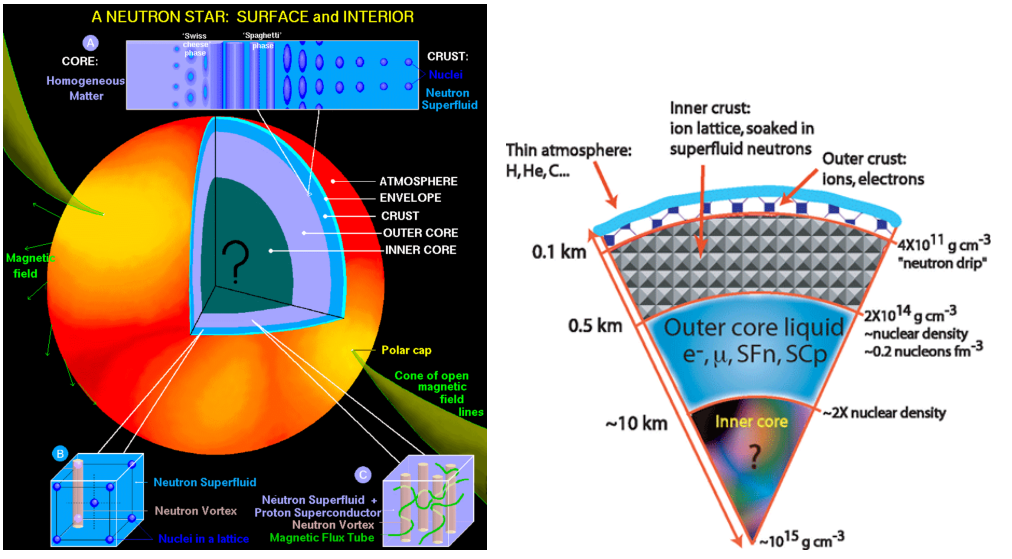

Figure 1.2: Internal structure of neutron stars, where the major regions are shown, in two representatives schematic presentations (Arzoumanian et al., 2009; Lattimer, 2010, 2014; Lattimer and Prakash, 2004).

imposed a limit on the mass along with a limit for the maximum density inside any neutron star. Thus, it leads to a limit for the ultimate energy density of cold, baryonic matter in our universe. Concluding, the intense concentration of matter in neutron stars can be described only in General Relativity, Einstein's theory of gravity which alone describes the way the weakest force in nature arranges the distribution of the mass and the constituents of the densest objects in the universe.

The overall structure of neutron stars is controlled through the TOV equation, as already mentioned. Their composition does not affect the aforementioned equations. Specifically, the TOV stellar structure equations provided through general relativity are expressed as

$$\frac{dP(r)}{dr} = -\frac{G\mathcal{E}(r)M(r)}{c^2r^2}\left(1+\frac{P(r)}{\mathcal{E}(r)}\right)\left(1+\frac{4\pi P(r)r^3}{M(r)c^2}\right)\left(1-\frac{2GM(r)}{c^2r}\right)^{-1}, \tag{1.1}$$

$$\frac{dM(r)}{dr} = \frac{4\pi r^2}{c^2}\mathcal{E}(r), \tag{1.2}$$

where P is the pressure, $\mathcal{E}$, which is equal to ρc^2, is the energy density, and M is the gravitational mass interior to the radius r. The TOV equations cannot always provide physical solutions. Thus, in order to have physical solutions, these equations have boundary conditions. More precisely,

- For $r = 0$, all gradients and M are zero,
- $P = 0$ at the surface where $r = R_{\text{max}}$ and $M = M_{\text{max}}$.

An EoS in the form $P(\mathcal{E})$, which arrives from nuclear physics, describing all the layers of a neutron star, dictates a unique mass-radius curve, as shown in the Figure 1.3.

Figure 1.3 displays the one-to-one correspondence of the EoS (a relation between pressure and energy) with the mass-radius curve. In fact, Figure 1.3 shows the connection of nuclear physics with astrophysics. Two general features can be extracted: (a) it is a consequence of general relativity that maximum mass exists for any causal[1] EoS. It is widely known that the

[1]Causality is the condition that the speed of sound, $\sqrt{dP/dr}$, never exceeds the speed of light.

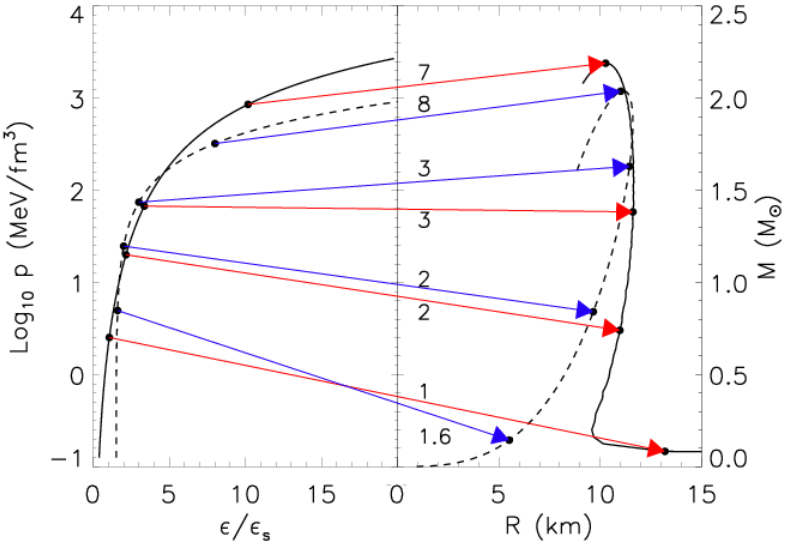

Figure 1.3: The pressure dependence on the energy density and the corresponding mass dependence on the radius for a specific EoS. The arrows show the one-to-one correspondence of the pressure/energy to the mass/radius (Lattimer, 2012).

term *maximum mass* does not exist in Newtonian gravity, and (b) the nature of the EoS dictates the slope of the mass-radius curve. This can be seen from the dimensional analysis of the structure equations, ignoring of course the general relativistic terms.

Determining the maximum neutron star mass is a long-standing issue in astrophysics since it is directly related to identifying black holes and the unknown behavior of nuclear matter at high densities. Until now, the observation of non/slow-rotating neutron stars has provided severe constraints on the dense nuclear matter through their maximum possible mass. The most massive neutron stars measurements include: (a) the PSR J1614-2230 ($M = 1.97 \pm 0.04\ M_{\odot}$) (Demorest et al., 2010) (or from the recent elaboration of the observation $M = 1.928 \pm 0.017\ M_{\odot}$ (Fonseca et al., 2016) and also $M = 1.908 \pm 0.016 M_{\odot}$ (Arzoumanian et al., 2018)), (b) the PSR J0348+0432 ($M = 2.01 \pm 0.04\ M_{\odot}$) (Antoniadis et al., 2013), (c) the PSR J0740+6620 ($M = 2.14^{+0.10}_{-0.09}\ M_{\odot}$) (Cromartie et al., 2019), and (d) the PSR J2215+5135 ($M = 2.27^{+0.17}_{-0.15}\ M_{\odot}$) (Linares et al., 2018). In addition, there is a detailed study concerning the spin frequency of rotating neutron stars (for a review, see Refs. (Patruno et al., 2017)). The fastest rotating pulsar found is the J1748-244ad with a spin frequency of 716 Hz (Hessels et al., 2006). Nonetheless, the issue is still open: *why we have not observed pulsars with higher values of frequency which predicted from the majority of theoretical models?* And even more, *what limits the spin frequencies of millisecond pulsars and why?* (Prakash, 2015). Future measurements of the moment of inertia (Bejger et al., 2005) and Keplerian frequency may answer these questions by considerably improving our knowledge of the properties of maximally-rotating neutron stars.

The effects of the EoS on the properties of rotating neutron stars (see Refs. (Paschalidis and Stergioulas, 2017; Stergioulas, 1998) for introduction and relevant bibliography) began to gain ground almost 30yr ago from Shapiro, Teukolsky, and their colleagues (Cook et al., 1992, 1994a,b,c; Shapiro et al., 1989). A significant contribution to these issues had also been

made by Friedman and his colleagues (Friedman and Ipser, 1987; Friedman et al., 1986, 1988, 1989; Koranda et al., 1997), Haensel and co-workers (Haensel and Zdunik, 1989; Haensel et al., 1995, 1999; Lasota et al., 1996; Salgado et al., 1994a,b), as well as Glendenning and his colleagues (Glendenning, 1992; Glendenning and Weber, 1994; Weber and Glendenning, 1991; Weber and Glendenning, 1992). Rapid rotation and its effects on the EoS have also been studied in Refs. (Abramowicz and Wagoner, 1978; Hashimoto et al., 1994; Iida and Sato, 1997; Lattimer et al., 1990; Lindblom, 1986; Shibata et al., 2000) and most recently in Refs. (Agrawal et al., 2008; Bejger et al., 2017; Benhar et al., 2005; Breu and Rezzolla, 2016; Chakrabarti et al., 2014a; Cipolletta et al., 2015, 2017; Dhiman et al., 2007; Haensel et al., 2008, 2009, 2016; Haskell et al., 2018; Krastev et al., 2008; Lo and Lin, 2011; Riahi et al., 2019; Zhang et al., 2013). Moreover, in nuclear astrophysics hot neutron stars in correlation with rapid rotation had been studied in Refs. (Batra et al., 2018; Marques et al., 2017). In addition, maximally-rotating neutron stars in modified gravity theories have been studied in detail by Kokkotas and his colleagues (Doneva et al., 2013; Yazadjiev et al., 2015).

In the present dissertation, the previous fundamental work of Cook, Shapiro, and Teukolsky (Cook et al., 1994b), as well as the most recent work of Cipolletta et al. (Cipolletta et al., 2015), are extended. In particular, a large number of modern EoSs (combined with a few previous ones) which all of them, at least marginally (few of them), predict the upper bound of the maximum neutron star mass of $M = 1.908 \pm 0.016\ M_{\odot}$ (Arzoumanian et al., 2018), while also reproducing the bulk properties of symmetric nuclear matter accurately (for more details see Ref. (Koliogiannis and Moustakidis, 2019)), are employed. The models of these EoSs are phenomenological, field theoretical, and microscopic. In the category of phenomenological models, there are the: MDI (Moustakidis and Panos, 2009; Prakash et al., 1997), HHJ (Heiselberg and Hjorth-Jensen, 2000), Ska, SkI4 (Chabanat et al., 1997; Farine et al., 1997) and DH (Douchin and Haensel, 2001), in field theoretical one, there are the: NLD (Gaitanos and Kaskulov, 2013, 2015) and W (Walecka, 1974) and in microscopic one, there are the: HLPS (based on nuclear interactions derived from chiral effective field theory) (Hebeler et al., 2013), SCVBB (using the Argonne v18 potential plus three-body forces computed with the Urbana model) (Sharma et al., 2015), BS (Balberg and Shapiro, 2000), BGP (Relativistic pion exchange) (Bowers et al., 1975), BL (Bombaci and Logoteta, 2018), WFF1, WFF2 (Wiringa et al., 1988) and PS (Pandharipande and Smith, 1975). It must be stressed that the majority of the mentioned EoSs have been constructed to reproduce the bulk properties of uniform symmetric nuclear matter and extend to pure neutron matter. The extension to neutron star matter is performed with respect to beta equilibrium. Regarding the leptonic degree of freedom, in most of them, it is considered that the main contribution of leptons is due to electrons. All of the used EoSs adequately describe the fluid core of a neutron star. It should also be noted that few have been applied first to study finite nuclei. Among the number of equations that are being employed, we have constructed two EoSs, the APR-1 and APR-2 (Microscopic model) (Akmal et al., 1998), predicted by the Momentum-Dependent Interaction model (MDI). This model reproduces the results of microscopic calculations of symmetric nuclear matter and neutron star matter at zero temperature with the advantage of its extension to finite temperature. For the solid crust region of all the EoSs, the EoS of Feynman, Metropolis, and Teller (Feynman et al., 1949) and also of Baym, Bethe, and Sutherland (Baym et al., 1971), are employed.

An effort was made to systematically study most of the bulk properties of uniformly rotating neutron stars at the Keplerian sequence (the sequence in which the maximum mass configuration corresponds to the Keplerian frequency), including the mass, polar and equatorial radius, angular velocity, moment of inertia, Kerr parameter, eccentricity, braking index, etc. Additionally, for reasons of completeness and comparison, because the employed EoSs are hadronic ones, an EoS with the appearance of hyperons at high densities (FSU2H) (Tolos et al., 2017a) and one suitable to describe quark stars based on MIT bag model (QS57.6) (Glendenning, 2000; Haensel et al., 2007), are also introduced.

Furthermore, the possibility of updating the previous empirical universal relations, which connect the Keplerian frequency with the mass and radius at the maximum mass configuration, is explored. We systematically study the Kerr parameter dependence on the EoS and provide the evolution of the angular momentum of a neutron star to examine the case where neutron stars are considered progenitors of black holes. In particular, we examine (according to the terminology of Ref. (Cook et al., 1994b)) two equilibrium sequences of rotating neutron stars, *normal* and *supramassive*. While *normal* evolutionary sequences have a spherical, non-rotating (stable) endpoint, *supramassive* ones, which by definition have masses higher than the maximum mass of the non-rotating neutron star, do not have a stable endpoint and as a consequence, the collapse to a black hole is inevitable. However, the construction of *normal* and mainly *supramassive* sequences is a complicated procedure in the framework of General Relativity (Cook et al., 1994b).

In addition, a systematic study of the moment of inertia, a quantity that plays an essential role in the properties of rotating neutron stars, and eccentricity, which can inform us of their deformation, is performed. Following the previous work of Lattimer and Prakash (Lattimer and Prakash, 2005), we also provide an absolute upper limit of the higher density of cold baryonic matter in the Universe, based on the upper limit imposed by the maximum mass of a neutron star. In fact, an effort to improve the bound that was introduced in Ref. (Lattimer and Prakash, 2005), by using updated EoSs and including the case of maximally-rotating neutron stars, is taking place. Closing the section, the effects of the EoS on the braking index of pulsars are under consideration. We mainly focus on values near the Keplerian frequency (70% and more) where the braking index begins to be affected by the rest mass (definition has been given in a proper section).

However, the recent observation of gravitational waves from a merging neutron star binary system (GW170817; Abbott et al. (Abbott et al., 2017)) opened a new, significant source to probe and improve our knowledge of the EoS in multiple ways. Specifically, the EoS of cold and hot nuclear matter considerably affects the dynamic process of binary neutron star's prior and postmerger phases, leading to a hot remnant. This process also includes the tidal polarizability during the inspiral of a binary system. In addition, after the merger, the maximum stable mass, the spin period, and the lifetime of the remnant strongly depend on the dense matter properties at high temperatures and entropy. In particular, the evolution and possible final stage of the remnant are sensitive to the EoS, including (a) the time scale for the gravitational collapse to a black hole; (b) the possibility of a phase transition to other degrees of freedom (hyperons, quarks, etc.), which may lead to collapse to a black hole (due to softening of the EoS); and (c) the creation of a disk around the remnant, ejecta, and neutrino emission.

In earlier years, pioneering work was done for the study of a hot EoS for astrophysical applications, including the studies of Bethe et al. (Bethe et al., 1979), Brown et al. (Brown et al., 1982), Lamb et al. (Lamb et al., 1978), Lattimer & Ravenhall (Lattimer and Ravenhall, 1978) and Lattimer (Lattimer, 1981). Over the years, the most used EoSs of hot neutron star matter have been (a) the liquid drop-type model constructed by Lattimer & Swesty (Lattimer and Swesty, 1991) and (b) the one by Shen et al. (Shen et al., 1998), where the relativistic mean field model is employed. Later on, Shen et al. (Shen et al., 1998) extended their study to generate EoSs of nuclear matter for a wide range of temperatures, densities, and proton fractions for applications in supernovae, neutron star mergers and black hole formation simulations by also employing a full relativistic mean field (Shen et al. 2011).

Wellenhofer et al. (Wellenhofer et al., 2015) investigated the density and temperature dependence of the nuclear symmetry free energy using microscopic two- and three-body nuclear potentials constructed from Chiral effective field theory. Constantinou et al. (Constantinou et al., 2014, 2015) derived a hot EoS suitable to describe supernova and hot neutron star properties. Temperature effects on the neutron star matter EoS were investigated in the Chiral effective field theory framework by Sammarruca et al. (Sammarruca et al., 2020). The properties of hot $\beta-$stable nuclear matter, using EoSs derived within the Brueckner-Hartree-Fock approach at

finite temperature, have been provided in several papers (Nicotra et al. (Nicotra et al., 2006); Burgio & Schulze (Burgio and Schulze, 2010); Baldo & Burgio (Baldo and Burgio, 2016); Fortin et al. (Fortin et al., 2018); Lu et al. (Lu et al., 2019), (Li et al., 2021); Figura et al. (Figura et al., 2020); Shang et al. (Shang et al., 2020); Wei et al. (Wei et al., 2020)). Raithel et al. (Raithel et al., 2019) derived a model that extends any cold nucleonic EoS, including piecewise polytropes, to arbitrary temperature and proton fractions for use in calculations and numerical simulations of astrophysical phenomena.

Moreover, a detailed study of the evolution of protoneutron stars was predicted by Pons et al. (Pons et al., 1999) and Prakash et al. (Prakash et al., 2001). The authors focused on the thermal and chemical evolution of the birth of neutron stars by employing neutrino opacities consistently calculated with the underlying nuclear EoS (Pons et al. (Pons et al., 1999)). For a recent review of the hot EoS of dense matter and neutron stars, see Lattimer & Prakash (Lattimer and Prakash, 2016).

In the last 40 yr, a lot of theoretical work has been dedicated to studying the processes of the merger and postmerger phases of a binary neutron star system, and important progress has been achieved. However, many relevant issues remain unsolved or at least under consideration. In general, the reference to the remnant evolution mainly includes the collapse time and threshold mass. Moreover, the possibility of a phase transition in the remnant's interior may affect the signal of the emitted gravitational waves. In addition, matters under consideration are also the disk ejecta and neutrino emission properties, which are sensitive to the employed EoS (for an extended discussion and applications, see Perego et al. (Perego et al., 2019)). Some previous work is included in Bauswein et al. (Bauswein et al., 2010), Kaplan et al. (Kaplan et al., 2014), Tsokaros et al. (Tsokaros et al., 2020), Yasin et al. (Yasin et al., 2020), Radice et al. (Radice et al., 2020), Sarin et al. (Sarin et al., 2020), Soma & Bandyopadhyay (Soma and Bandyopadhyay, 2020), and Sen (Sen, 2020).

It is worth mentioning that the theory of quantum chromodynamics (QCD) predicts the ongoing transition of hadron matter to unconfined quark matter at a sufficiently high density (a few times the saturation density). As neutron stars provide a rich testing ground for microscopic theories of dense nuclear matter, combining this study with the experimental data from ultrarelativistic heavy-ion collisions (the Relativistic Heavy Ion Collider at Brookhaven and the Large Hadron Collider at CERN) may help to improve our knowledge of QCD theory significantly (Baym et al. 2018). However, the problem of the existence of free quark matter in the interior of neutron stars remains. Moreover, the emergence of strange hadrons (hyperons, etc.) around twice the nuclear saturation density leads to an appreciable softness of the EoS and low values of neutron star mass, far from observation. This problem is highlighted as the hyperon puzzle. Of course, there are other studies where the authors stated that hyperon consideration on the EoS is not in contradiction with the predictions of a very high neutron star mass (see Chatterjee & Vidana 2016; Li et al. 2020).

It has been claimed that the recent observation of gravitational waves from neutron star mergers could shed light on the possibility of hadrons moving to a quark phase transition (Annala et al. 2020). The authors stated that if the conformal limit on the value of the speed of sound, $c_s/c \leq 1/\sqrt{3}$, is not strongly violated, then heavy neutron stars may have sizable quark matter cores. In this case, important implications must be considered in neutron star mergers with at least one massive participant (Annala et al. 2020). However, in the present research, the case of additional degrees of freedom (hyperons, quarks, etc.) in the interior of neutron stars is not under active consideration. This issue will be under consideration in a future study.

As a continuation, the bulk properties of hot nuclear and neutron star matter are investigated. In particular, we apply a momentum-dependent effective interaction (MDI) model, where thermal effects can be studied simultaneously on the kinetic part of the energy and the interaction. Compared to others, the advantage of the present model is that thermal effects are introduced in a self-consistent way. Specifically, we rigorously enforce the thermodynamic laws describing

the hot dense nuclear matter. In addition, this model can be extended in order to modify the stiffness of the proposed EoS by properly parameterizing the nuclear symmetry energy. It is worth pointing out that a large number of EoSs of hot nuclear and neutron star matter for astrophysical applications have appeared over the years, employing various theoretical models and approximations. However, most of them are questionable in the sense that thermal effects are not included in the cold EoS in a self-consistent way but rather in an artificial one. This point has already been noted in Constantinou et al. (Constantinou et al., 2015). Actually, the present model was introduced by Gale et al. (Gale et al., 1987) in order to examine MDI's influence on the momentum flow of heavy-ion collisions. Nonetheless, over the years, the model has been extensively applied to study the properties of cold and hot nuclear and neutron star matter (for a review of the model, see Prakash et al. 1997; Li & Schröder 2001; Li et al. 2008).

Afterward, a set of thermodynamically consistent isothermal and isentropic EoSs are produced based on the parameterized cold one. Our eventual purpose is the application of the predicted EoSs for an extensive study on the bulk properties (including mainly the mass and radius, moment of inertia, Kerr parameter, etc.) both at non-rotating and rotating with the Kepler frequency neutron stars, as well as protoneutron stars, and neutron star merger remnants. We pay special attention to the sequences of constant baryon mass (baryon mass is equal to rest mass) and examine the peculiar role of the Kerr parameter. Finally, we dedicate a part to studying a few postmerger processes, such as the hot, rapidly rotating remnant and the threshold mass, and we connect them with the derived EoSs.

Lastly, the research is focused on the stability of relativistic stars, which has been studied extensively in the past (Chandrasekhar, 1964a,b; Friedman and Stergioulas, 2013; Glendenning, 2000; Haensel et al., 2007; Harrison et al., 1965; Shapiro and Teukolsky, 1983; Weinberg, 1972; Zeldovich and Novikov, 1978), where various approaches have been used in order to treat this problem (Bardeen et al., 1966). In particular, firstly, one can solve the TOV (Oppenheimer and Volkoff, 1939; Tolman, 1939) equations (which provide the equilibrium configuration) for either numerically derived EoS or trying to find analytical solutions. In any case, both solutions lead to an infinite number of configurations. Secondly, one possibility is the use of the criterion of Chandrasekhar (Chandrasekhar, 1964a,b) in order to identify, in each case, the stable configuration as well as the interface between stable and unstable configuration.

It is worth pointing out that in order to extract a solution with physical interest, one has to solve Einstein's field equations using a realistic EoS of the fluid interior. However, there are a few analytical solutions with physical interest that may help to introduce and to establish some universal approximations.

Moreover, at a given density, there is an important parameter that is called adiabatic index and, in particular, characterizes the stiffness of the EoS (Bludman, 1973a,b; Gaertig and Kokkotas, 2009; Glass and Harpaz, 1983; Haensel et al., 2007; Harrison et al., 1965; Hiscock and Lindblom, 1983; Ipser, 1970; Lindblom and Detweiler, 1983; Misner et al., 1973). The instability criterion of Chandrasekhar (Chandrasekhar, 1964a,b), strongly depends on this parameter (adiabatic index). One of the main motivations of the present work is to examine the possibility of imposing constraints on the realistic neutron star EoSs via the instability condition of Chandrasekhar.

In particular, an extended group of realistic EoSs based on various theoretical nuclear models is employed. The abbreviated names of these EoSs are: MDI (Moustakidis and Panos, 2009; Prakash et al., 1997), NLD (Gaitanos and Kaskulov, 2013, 2015), HHJ (Heiselberg and Hjorth-Jensen, 2000), Ska, SkI4 (Chabanat et al., 1997; Farine et al., 1997), HLPS (Hebeler et al., 2013), SCVBB (Sharma et al., 2015), BS (Balberg and Shapiro, 2000), BGP (Bowers et al., 1975), W (Walecka, 1974), DH (Douchin and Haensel, 2001), BL (Bombaci and Logoteta, 2018), WFF1,WFF2 (Wiringa et al., 1988), APR (Akmal et al., 1998) and PS (Pandharipande and Smith, 1975). All of them satisfy, at least marginally, the observed limit of $M = 1.97 \pm 0.04\ M_{\odot}$ (PRS J1614-2230 (Demorest et al., 2010)) and $M = 2.01 \pm 0.04\ M_{\odot}$ (PSRJ0348+0432 (Antoniadis et al., 2013)). Actually, at the moment, the most robust constraints on the neutron star EoSs

are based on the measurements of the lower bound of the maximum neutron star mass. Strictly speaking, the suggested EoSs, which do not reproduce the higher measurement of neutron star mass, must be excluded.

It is also well known that the rapidly rotating neutron stars can be used in order to determine the EoS (see Ref. (Haensel et al., 2007) and reference therein). In particular, the maximum rotating frequency $f_{\max}$ (Keplerian frequency) depends both on the gravitational mass $M_{\max}$ and the EoS. Until this moment, the fastest known pulsar, PSR J1748-244ad, is rotating with frequency 716 Hz (Hessels et al., 2006). While the theoretically predicted values for $f_{\max}$ are much higher than 716 Hz, there is a lack of neutron stars rotating faster than this value. It is an open problem, and additional theoretical assumptions must be needed to solve it.

The present research concentrates on the dependence of the effective critical adiabatic index on the compactness of neutron star for each EoS. We mainly focus on the interface between stable and unstable configurations, corresponding to the maximum mass configuration. This region is critical since it is directly related to the high density part of the neutron star EoS. This issue remains an open problem. Moreover, we propose an additional method to constrain the EoSs with the help of accurate measurements of the maximum neutron star mass and/or compactness. Finally, we make an effort to relate the maximum rotating frequency $f_{\max}$ with the critical adiabatic index and the bulk properties corresponding to the maximum mass configuration of a non-rotating (static) neutron star (including the maximum mass $M^{\rm stat}_{\max}$, the corresponding radius $R^{\rm stat}_{\max}$ and the compactness parameter $\beta^{\rm stat}_{\max}$) so as to indicate how observational measurements of high rotating neutron stars may impose constraints on the EoS.

For the numerical integration of the equilibrium equations, two set of codes have been used

- RNS: Numerical code for rotating neutron stars from (Stergioulas and Friedman, 1995)
- NROTSTAR: Numerical code from the C++ Lorene/Nrotstar library (LORENE, 1998)

The dissertation is structured as follows. In Section 2, neutron stars' stellar composition and structure, considering both the hot and cold matter, is presented, paying particular attention to the microscopic quantities and their analysis. In Section 3, the stability criteria for cold as well as hot neutron stars are provided, while in Section 4, the construction of the EoSs, considering the cold and hot neutron star matter, is illustrated. Section 5 is devoted to describing the bulk cold neutron star properties and their connection with rapid rotation, while Section 6 is focused on the stability of cold neutron stars through the adiabatic index. Neutron stars with hot, lepton-rich matter and rapid rotation are extensively analyzed in Section 7, and Section 8 is dedicated to the concluding remarks of the research. Appendix provides the numerical recipes for some research processes.

CHAPTER 2

Stellar composition and structure

2.1 Momentum-dependent interaction model

The schematic potential of the MDI model is specifically designed to reproduce the results of the more microscopic calculations of nuclear matter, as well as of neutron-rich matter at zero temperature (Moustakidis, 2007, 2008, 2009; Moustakidis and Panos, 2009; Prakash et al., 1997; Psonis et al., 2007). This model combines both density and momentum dependent interaction among the nucleons. It is well known that nuclear interaction has strong exchange effects that give rise to a momentum dependence in the single particle potential, and as a consequence, it has an effect on the energy density functional. The present model was introduced by Gale et al. (Bertsch and Gupta, 1988; Gale et al., 1987, 1990; Prakash et al., 1988) to examine the influence of momentum dependent interactions on the momentum flow of heavy-ion collisions. Over the years, the model has been modified, elaborated and, extensively applied in the study not only of heavy-ion collisions but also the properties of nuclear matter (Chen et al., 2005; Csernai et al., 1992; Das et al., 2007, 2003; Li et al., 2004a,b; Modarres, 1997; Sumiyoshi and Toki, 1994; Xu et al., 2007a). A major advantage of this model is the extension to finite temperature through the momentum dependent interactions among the nucleons. In the following, we are going to calculate and present the different aspects (zero and finite temperature) of the MDI model with analytical description.

The energy density of the asymmetric nuclear matter (ANM) is given by the equation

$$\mathcal{E}\left(n_n, n_p, T\right) = \mathcal{E}^n_{kin}\left(n_n, T\right) + \mathcal{E}^p_{kin}\left(n_p, T\right) + V_{int}\left(n_n, n_p, T\right), \tag{2.1}$$

where n_n, n_p, and n are the neutron, proton, and total density $(n = n_n + n_p)$, respectively. The first two terms in Equation (2.1) are referring to the contribution of the kinetic energy from both neutrons and protons, and can be written as

$$\mathcal{E}^\tau_{kin}\left(n_\tau, T\right) = 2\int \frac{\mathrm{d}^3k}{(2\pi)^3}\frac{\hbar^2k^2}{2m} f_\tau\left(n_\tau, k, T\right), \tag{2.2}$$

where τ denotes the neutrons and protons, m denotes the nucleon mass, and f_τ is the Fermi-Dirac distribution function with respect to τ given by the following form

$$f_\tau\left(n_\tau, k, T\right) = \left[1 + exp\left(\frac{e_\tau\left(n_\tau, k, T\right) - \mu_\tau\left(n_\tau, T\right)}{T}\right)\right]^{-1}. \tag{2.3}$$

The nucleon density n_τ, that appears in Equation (2.3), in accordance to f_τ, can be evaluated

from the integral

$$\begin{aligned} n_\tau &= 2\int \frac{\mathrm{d}^3k}{(2\pi)^3} f_\tau\left(n_\tau, k, T\right) \\ &= 2\int \frac{\mathrm{d}^3k}{(2\pi)^3}\left[1 + exp\left(\frac{e_\tau\left(n_\tau, k, T\right) - \mu_\tau\left(n_\tau, T\right)}{T}\right)\right]^{-1}. \end{aligned} \tag{2.4}$$

The terms that appear in Equation (2.4) can be explained as follows

- $e_\tau\left(n_\tau, k, T\right) \rightarrow$ single-particle energy (SPE),
- $\mu_\tau\left(n_\tau, T\right) \rightarrow$ chemical potential.

The single-particle energy has the following form

$$e_\tau\left(n_\tau, k, T\right) = \frac{\hbar^2 k^2}{2m} + U_\tau\left(n_\tau, k, T\right), \tag{2.5}$$

where the single-particle potential $U_\tau\left(n_\tau, k, T\right)$, which depends on the momentum, is obtained by the functional derivative of the interaction of the energy density with respect to the distribution function f_τ. Including the effect of finite-range forces among nucleons, in order to avoid acausal behavior at high densities, the potential contribution is parametrized as

$$\begin{aligned} V_{\text{int}}(n_n, n_p, T) = &\frac{1}{3}An_s\left[\frac{3}{2} - X_0 I^2\right]u^2 \\ &+ \frac{\frac{2}{3}Bn_s\left[\frac{3}{2} - X_3 I^2\right]u^{\sigma+1}}{1 + \frac{2}{3}B'\left[\frac{3}{2} - X_3 I^2\right]u^{\sigma-1}} \\ &+ u\sum_{i=1,2}\left[C_i\left(\mathcal{J}_n^i + \mathcal{J}_p^i\right) + I\frac{(C_i - 8Z_i)}{5}\left(\mathcal{J}_n^i - \mathcal{J}_p^i\right)\right], \end{aligned} \tag{2.6}$$

where n_s denotes the saturation density, $u = n/n_s$, $I = 1 - 2Y_p$ is the asymmetry parameter, Y_p is the proton fraction, $X_i = \frac{1}{2} + x_i$, with $i = 0, 3$, $[A, B, B', \sigma, C_i]$ are the parameters for symmetric nuclear matter (SNM), $[x_0, x_3, Z_i]$ are the parameters for asymmetric nuclear matter, and

$$\mathcal{J}_\tau^i = 2\int \frac{d^3k}{(2\pi)^3} g(k, \Lambda_i) f_\tau(n_\tau, k, T), \tag{2.7}$$

with $g(k, \Lambda_i)$ being a suitable function to simulate finite range effects defined as

$$g(k, \Lambda_i) = \left[1 + \left(\frac{k}{\Lambda_i}\right)^2\right]^{-1}. \tag{2.8}$$

The finite-range terms, that correspond to a long range attraction and a short range repulsion, take the values $\Lambda_i = [1.5\ k_F^0, 3\ k_F^0]$, where k_F^0 is the Fermi momentum at the saturation density.

It has to be noted here that there is another case for the $g(k, \Lambda_i)$ function. In that case,

$$g(k, \Lambda_i) = \left[1 - \left(\frac{k}{\Lambda_i}\right)^2\right], \tag{2.9}$$

the finite-range interactions are approximated by effective local interactions by retaining only the quadratic momentum dependence. In fact, Equations (2.8) and (2.9) coincide for low values of momenta, but diverge for higher values.

The entropy density has the same functional form with that of a non-interacting gas system given by

$$s_\tau(n,T,I) = -g\int \frac{\mathrm{d}^3k}{(2\pi)^3}\left[f_\tau \ln f_\tau + (1-f_\tau)\ln(1-f_\tau)\right], \tag{2.10}$$

where g stands for the spin degeneracy, and it is equal to 2 for protons, neutrons, electrons, and muons, and equal to 1 for neutrinos.

2.1.1 Symmetric nuclear matter

In symmetric nuclear matter, the energy density can be calculated through Equations (2.1) and (2.6) by setting the asymmetry parameter equal to zero, as (Moustakidis, 2007)

$$\begin{aligned}\mathcal{E}_{\text{snm}}(n,T) = {} & 2\int \frac{\mathrm{d}^3k}{(2\pi)^3}\frac{\hbar^2k^2}{2m}f_n + 2\int \frac{\mathrm{d}^3k}{(2\pi)^3}\frac{\hbar^2k^2}{2m}f_p + \frac{1}{2}An_su^2 + \frac{Bn_su^{\sigma+1}}{1+B'u^{\sigma-1}} \\ & + 2u\left[\sum_{i=1,2}C_i\int\frac{\mathrm{d}^3k}{(2\pi)^3}g(k,\Lambda_i)f_n + \sum_{i=1,2}C_i\int\frac{\mathrm{d}^3k}{(2\pi)^3}g(k,\Lambda_i)f_p\right].\end{aligned} \tag{2.11}$$

In this case, the single particle potential is calculated through the relation

$$U^\tau_{\text{snm}}(n,k;T) = \tilde{U}^\tau_{\text{snm}}(n;T) + u\sum_{i=1,2}C_ig(k,\Lambda_i), \tag{2.12}$$

where the momentum dependence appears in the last term. The momentum independent term $\tilde{U}^\tau_{\text{snm}}(n;T)$ is available through the form

$$\begin{aligned}\tilde{U}^\tau_{\text{snm}}(n;T) = {} & Au + \frac{Bu^\sigma(\sigma+1+2B'u^{\sigma-1})}{(1+B'u^{\sigma-1})^2} \\ & + \frac{4}{n_s}\sum_{i=1,2}C_i\int\frac{\mathrm{d}^3k}{(2\pi)^3}g(k,\Lambda_i)f_\tau.\end{aligned} \tag{2.13}$$

2.1.2 Pure neutron matter

In pure neutron matter, the energy density can be calculated through Equations (2.1) and (2.6) by setting the asymmetry parameter equal to one, as (Moustakidis, 2007)

$$\begin{aligned}\mathcal{E}_{\text{pnm}}(n,T) = {} & 2\int\frac{\mathrm{d}^3k}{(2\pi)^3}\frac{\hbar^2k^2}{2m}f_n + \frac{1}{3}An_s(1-x_0)u^2 + \frac{\frac{2}{3}Bn_s(1-x_3)u^{\sigma+1}}{1+\frac{2}{3}B'(1-x_3)u^{\sigma-1}} \\ & + \frac{4u}{5}\sum_{i=1,2}(3C_i-4Z_i)\int\frac{\mathrm{d}^3k}{(2\pi)^3}g(k,\Lambda_i)f_n.\end{aligned} \tag{2.14}$$

In this case, the single particle potential is calculated through the relation

$$U_{\text{pnm}}(n,k;T) = \tilde{U}(n;T) + \frac{2}{5}u\sum_{i=1,2}(3C_i-4Z_i)g(k,\Lambda_i), \tag{2.15}$$

where the momentum dependence appears in the last term. The momentum independent term $\tilde{U}_{\text{pnm}}(n;T)$ is available through the form

$$\begin{aligned}\tilde{U}_{\text{pnm}}(n;T) = {} & \frac{2}{3}A(1-x_0)u + \frac{\frac{2}{3}B(1-x_3)u^\sigma}{\left[1+\frac{2}{3}B'(1-x_3)u^{\sigma-1}\right]^2}\left[(\sigma+1)+\frac{4}{3}B'(1-x_3)u^{\sigma-1}\right] \\ & + \frac{4}{5n_s}\sum_{i=1,2}(3C_i-4Z_i)\int\frac{\mathrm{d}^3k}{(2\pi)^3}g(k,\Lambda_i)f_n.\end{aligned} \tag{2.16}$$

In both cases of subsections 2.1.1 and 2.1.2, for a fixed baryon density and temperature, Equation (2.4) can be solved iteratively for

$$\eta(n,T) = \frac{\mu(n,T) - \tilde{U}(n,T)}{T}. \tag{2.17}$$

The knowledge of $\eta(n,T)$ allows the evaluation of the last term in Equations (2.13) and (2.16), which then inferred the chemical potential from

$$\mu(n,T) = T\eta(n,T) + \tilde{U}(n,T). \tag{2.18}$$

Equation (2.18) is a requirement for the calculation of the single particle spectrum, and as a consequence, the evaluation of the bulk quantities of asymmetric nuclear matter.

2.1.3 Single-particle potentials

In the single particle energy, calculated through Equation (2.5), the interaction term, in general, depends on the density, the momentum, the isospin asymmetry, and the temperature, $U_\tau = (n, I, k, T)$. The single-particle potential has the general form (Moustakidis, 2008; Moustakidis and Panos, 2009)

$$U_\tau(n,I,k,T) = U_\tau^{\mathrm{A}}(n,I) + U_\tau^{\mathrm{B}}(n,I) + U_\tau^{\mathrm{MD}}(n,I,k,T), \tag{2.19}$$

where the first two terms correspond to the momentum independent ones, and the last one describes the momentum dependence of the single-particle potential. Specifically, the terms can be expressed as:

$$U_\tau^{\mathrm{A}}(n,I) = Au \mp \frac{2}{3}AX_0uI, \tag{2.20}$$

$$U_\tau^{\mathrm{B}}(n,I) = \frac{U_\tau^{\mathrm{B_1}}(n,I)U_\tau^{\mathrm{B_2}}(n,I) - U_\tau^{\mathrm{B_3}}(n,I)U_\tau^{\mathrm{B_4}}(n,I)}{\left[U_\tau^{\mathrm{B_2}}(n,I)\right]^2}, \tag{2.21}$$

where

$$U_\tau^{\mathrm{B_1}}(n,I) = B\left(\sigma+1\right)u^\sigma \mp \frac{4}{3}BX_3u^\sigma I + \frac{2}{3}B\left(1-\sigma\right)X_3u^\sigma I^2, \tag{2.22}$$

$$U_\tau^{\mathrm{B_2}}(n,I) = 1 + \frac{2}{3}B'\left(\frac{3}{2} - X_3I^2\right)u^{\sigma-1}, \tag{2.23}$$

$$U_\tau^{\mathrm{B_3}}(n,I) = \frac{B'}{n_s}\left(\sigma-1\right)u^{\sigma-2} \mp \frac{4B'}{3n_s}X_3u^{\sigma-2}I + \frac{2B'}{3n_s}\left(3-\sigma\right)X_3u^{\sigma-2}I^2, \tag{2.24}$$

$$U_\tau^{\mathrm{B_4}}(n,I) = \frac{2}{3}Bn_s\left(\frac{3}{2} - X_3I^2\right)u^{\sigma+1}, \tag{2.25}$$

$$U_\tau^{\mathrm{MD}}(n,I,k,T) = \frac{4}{5n_s}\sum_{i=1,2}\left[\frac{1}{2}\left(3C_i - 4Z_i\right)\mathcal{J}_\tau^i + \left(C_i + 2Z_i\right)\mathcal{J}_{\tau'}^i\right] + u\sum_{i=1,2}\left[\left(C_i \pm \frac{C_i - 8Z_i}{5}I\right)g(k,\Lambda_i)\right]. \tag{2.26}$$

In Equation (2.26) the τ, τ' are referring to neutrons and protons, in accordance to the signs, whereas the upper signs denote the neutrons, and lower ones denote the protons. In particular,

while the first two terms are functions of the baryon density and the isospin parameter, the last one has an additional dependence on the temperature and the momentum. The latter is implied in the function $g(k, \Lambda_i)$ and is expected to be important both for the single-particle properties and the bulk properties of nuclear matter.

In addition, the calculation of the single-particle potential in symmetric nuclear matter have been performed in a microscopic way for several Hamiltonians in Wiringa (Wiringa, 1988). The Hamiltonians include nucleon-nucleon potentials fit to scattering data and three-nucleon potentials properties of nuclear matter. Following the formula

$$U(n,k) = \alpha(n) + \beta(n)\left[1 + \left(\frac{k}{\Lambda(n)}\right)^2\right]^{-1}, \tag{2.27}$$

where the parameters α, β, and Λ depend only the density and their calculation for three types of Hamiltonian is listed in Table I of Ref. (Wiringa, 1988). Furthermore, Li and Machleidt (Li and Machleidt, 1993), based on th Bonn meson-exchange model for the nucleon-nucleon interaction and the Dirac-Brueckner approach for the nuclear matter, has parameterized the single-particle potential as

$$U(n,k) = \alpha n + \beta n^{\gamma} + \delta \ln^2\left[\varepsilon\left(\hbar c k\right)^2 + 1\right] n^{\sigma}, \tag{2.28}$$

where the parameters α, β, γ, δ, ε, and σ are listed in Table I of Ref. (Li and Machleidt, 1993).

2.1.4 Nuclear symmetry potential

The nuclear symmetry potential is a quantity that corresponds to the isovector part of the nucleon mean-field in isospin asymmetric nuclear matter. In the case of hot nuclear matter, this property also depends on the temperature. The nuclear symmetry potential presents the behavior between the neutron and proton single particle potentials in neutron-rich matter, as (Moustakidis, 2008)

$$U_{\text{sym}}(n,I,k,T) = \frac{1}{2I}\left[U_n(n,I,k,T) - U_p(n,I,k,T)\right]. \tag{2.29}$$

Most of the theoretical models that have been applied to study the properties of the symmetry potential present the reduction of the nucleon symmetry potential with increasing nucleon momentum. However, there are studies that suggest the opposite behavior.

Based on the systematic analysis of a large number of nucleon-nucleon scattering experiments and (p,n) charge exchange reactions at beam energies up to 100 MeV, the data can be described as

$$U_{\text{sym}}(E_{\text{kin}}) = \alpha - bE_{\text{kin}}, \tag{2.30}$$

where $\alpha \in [22, 34]$ MeV and $b \in [0.1, 0.2]$. It is worth noticing that the uncertainties on these values are large (for more information see Refs. (Dalen et al., 2005; Kozack and Madland, 1990, 1989; Lane, 1962; van Dalen et al., 2004; van Dalen et al., 2005)).

2.1.5 Effective mass

One of the most important single-particle properties is the nucleon effective mass. It is a characterized quantity for the momentum dependence of the single-particle potential of a nucleon and consequently, for the quasi-particle properties of a nucleon inside a strongly interacting medium, i.e. the nuclear matter. In addition, the nucleon effective mass describes to a leading order the effects related to the non-locality of the underlying nuclear effective interaction and the Pauli exchange effects in many-fermion systems (Moustakidis, 2008).

In particular, the effective mass is defined via the momentum dependent single nucleon potential as

$$\frac{m_\tau^*(n,I,k)}{m_\tau} = \left[1 + \frac{m_\tau}{\hbar^2 k}\frac{dU_\tau(n,I,k,T)}{dk}\right]^{-1}. \tag{2.31}$$

Considering the evaluation of the Equation (2.31) at the Fermi momentum, then the Landau effective mass is provided. By employing Equation (2.21), Equation (2.31) can be presented in the analytical form

$$\frac{m_\tau^*(n,I,k)}{m_\tau} = \left\{1 + u\frac{m_\tau}{\hbar^2 k_\mathrm{F}}\sum_{i=1,2}\left[\left(C_i \pm \frac{C_i - 8Z_i}{5}I\right)\frac{dg(k,\Lambda_i)}{dk}\bigg|_{k=k_\mathrm{F}}\right]\right\}^{-1}. \tag{2.32}$$

By considering the cases Equation (2.8) and (2.9), Equation (2.32) can be evaluated as

$$\frac{m_\tau^*(n,I,k)}{m_\tau} = \left\{1 - \frac{2um_\tau}{\hbar^2}\sum_{i=1,2}\frac{1}{\Lambda_i^2}\frac{C_i \pm \frac{C_i - 8Z_i}{5}I}{\left[1 + \left(\frac{k_\mathrm{F}^0}{\Lambda_i}\right)^2\left[(1 \pm I)\,u\right]^{2/3}\right]^2}\right\}^{-1}, \tag{2.33}$$

$$\frac{m_\tau^*(n,I,k)}{m_\tau} = \left\{1 - \frac{2um_\tau}{\hbar^2}\sum_{i=1,2}\frac{1}{\Lambda_i^2}\left(C_i \pm \frac{C_i - 8Z_i}{5}I\right)\right\}^{-1}. \tag{2.34}$$

Equations (2.33) and (2.34) show the dependence of the properties of nuclear matter on the Landau effective mass. In particular, the Landau effective mass depends of the parameters C_i and Z_i, which are connected with the saturation properties and the density dependence of the nuclear symmetry energy, respectively. Additionally, there is a direct dependence on the baryon density and the isospin asymmetry, as well as on the values of Λ_i. The latter corresponds to the specific choice of the regulating function $g(k,\Lambda_i)$.

2.1.6 Properties of nuclear matter

The total energy per particle can be expanded as follows (Constantinou et al., 2014, 2015)

$$E(n,I) = E(n,0) + \sum_{k=2,4,\cdots} E_{\mathrm{sym},k}(n) I^k, \tag{2.35}$$

where

$$E_{\mathrm{sym},k}(n) = \frac{1}{k!}\frac{\partial^k E(n,I)}{\partial I^k}\bigg|_{I=0}. \tag{2.36}$$

In the case of the parabolic approximation (pa) it is considered that the symmetry energy is given through

$$E_{\mathrm{sym,pa}}(n) = E(n,I=1) - E(n,I=0), \tag{2.37}$$

while in the full approximation (f) it is given through

$$E_{\mathrm{sym,f}}(n) = E_{\mathrm{sym},2}(n) = S_2(n). \tag{2.38}$$

The properties of nuclear matter at the saturation density are defined as (Constantinou et al., 2014, 2015)

$$L = 3n_s\frac{dS_2(n)}{dn}\bigg|_{n_s}, \quad K = 9n_s^2\frac{d^2S_2(n)}{dn^2}\bigg|_{n_s}, \tag{2.39}$$

$$Q = 27n_s^3 \left.\frac{d^3S_2(n)}{dn^3}\right|_{n_s}, \quad K_0 = 9n_s^2 \left.\frac{d^2E(n,0)}{dn^2}\right|_{n_s}, \tag{2.40}$$

$$Q_0 = 27n_s^3 \left.\frac{d^3E(n,0)}{dn^3}\right|_{n_s}, \tag{2.41}$$

where L, K, Q are related to the first, second and third derivative of the symmetry energy $S_2(n)$, respectively. K_0 is the compression modulus and Q_0 is related to the third derivative of $E(n,0)$. The n_s is the saturation density of symmetric nuclear matter and its equal to 0.16 fm^{-3}.

2.2 Thermodynamics of hot neutron stars

The Helmholtz free energy F is a mandatory quantity for studying the properties of the nuclear matter at finite temperature. In particular, the differential of the total free energy F_{tot} and the total internal energy E_{tot} (total free/internal energy of baryons contained in volume V) are given as (Fetter and Walecka, 2003; Goodstein, 1985)

$$dF_{\text{tot}} = -S_{\text{tot}}dT - PdV + \sum_i \mu_i dN_i, \tag{2.42}$$

$$dE_{\text{tot}} = TdS_{\text{tot}} - PdV + \sum_i \mu_i dN_i, \tag{2.43}$$

where S_{tot} is the total entropy of baryons, and μ_i, N_i are the chemical potential and the number of particles of each species, respectively. The free energy per particle F can be written as

$$F(n,T,I) = E(n,T,I) - TS(n,T,I), \tag{2.44}$$

with $E = \mathcal{E}/n$ and $S = s/n$ being the internal energy and entropy per particle respectively. It has to be noted here that for $T = 0$ MeV, Equation (2.44) leads to the equality between free and internal energy. The latter means that for the cold, catalyzed matter, the internal energy and Helmholtz free energy coincide.

As the total internal energy is useful for studying isentropic processes, for the described thermodynamic system, pressure and chemical potentials are defined as follows

$$P = -\left.\frac{\partial E_{\text{tot}}}{\partial V}\right|_{S,N_i} = n^2 \left.\frac{\partial\left(\mathcal{E}/n\right)}{\partial n}\right|_{S,N_i}, \tag{2.45}$$

$$\mu_i = \left.\frac{\partial E_{\text{tot}}}{\partial N_i}\right|_{S,V,N_{j\neq i}} = \left.\frac{\partial \mathcal{E}}{\partial n_i}\right|_{S,V,n_{j\neq i}}. \tag{2.46}$$

2.2.1 Bulk thermodynamic quantities

It what follows, the research will focus on the presentation of bulk thermodynamic quantities and approximations related to the present study. As the key quantity is the free energy, the pressure and chemical potentials are connected with the derivative of the total free energy F_{tot} and defined as

$$P = -\left.\frac{\partial F_{\text{tot}}}{\partial V}\right|_{T,N_i} = n^2 \left.\frac{\partial\left(f/n\right)}{\partial n}\right|_{T,N_i}, \tag{2.47}$$

$$\mu_i = \left.\frac{\partial F_{\text{tot}}}{\partial N_i}\right|_{T,V,N_{j\neq i}} = \left.\frac{\partial f}{\partial n_i}\right|_{T,V,n_{j\neq i}}, \tag{2.48}$$

where f denotes the free energy density. Even more, the pressure P can be calculated also from (Fetter and Walecka, 2003; Goodstein, 1985)

$$P = Ts - \mathcal{E} + \sum_i \mu_i n_i. \tag{2.49}$$

The calculation of the entropy per particle $S(n,T)$ is being by differentiating the free energy density f with respect to the temperature

$$S(n,T) = -\frac{\partial\,(f/n)}{\partial T}\bigg|_{V,N_i} = -\frac{\partial F}{\partial T}\bigg|_{n}. \tag{2.50}$$

The comparison between Equations (2.10) and (2.50) for the entropy, provides a testing criterion of the approximation used in the present study.

By applying Equation (2.48), the chemical potentials for protons and neutrons take the form (for a proof see Ref. (Prakash, 1994) as well as Refs. (Burgio et al., 2007; Nicotra et al., 2006))

$$\mu_n = F + u\frac{\partial F}{\partial u}\bigg|_{Y_p,T} - Y_p\frac{\partial F}{\partial Y_p}\bigg|_{n,T}, \tag{2.51a}$$

$$\mu_p = \mu_n + \frac{\partial F}{\partial Y_p}\bigg|_{n,T}, \tag{2.51b}$$

$$\hat{\mu} = \mu_n - \mu_p = -\frac{\partial F}{\partial Y_p}\bigg|_{n,T}. \tag{2.51c}$$

The free energy $F(n,T,I)$ and the internal energy $E(n,T,I)$ can be expressed by the following parabolic approximations (PA) (Burgio et al., 2007; Moustakidis, 2008; Moustakidis and Panos, 2009; Nicotra et al., 2006; Xu et al., 2007b)

$$F(n,T,I) = F(n,T,I=0) + I^2 F_{\text{sym}}(n,T), \tag{2.52a}$$

$$E(n,T,I) = E(n,T,I=0) + I^2 E_{\text{sym}}(n,T), \tag{2.52b}$$

where

$$F_{\text{sym}}(n,T) = F(n,T,I=1) - F(n,T,I=0), \tag{2.53a}$$

$$E_{\text{sym}}(n,T) = E(n,T,I=1) - E(n,T,I=0). \tag{2.53b}$$

In order to apply the above approximation, the validity checking of the parabolic law is mandatory. The validity of the PA, at least in the present model, has been tested previously. It has been proved that the PA is well satisfied not only on the internal energy, but also on the free energy (Moustakidis, 2008; Moustakidis and Panos, 2009). A similar statement about the validity of the PA has also been found in Refs. (Burgio et al., 2007; Nicotra et al., 2006; Xu et al., 2007b). However, in other similar studies (Tan et al., 2016), it was found that the validity of the PA suffers from uncertainties. We conjecture that the validity of the PA strongly depends on the specific character of each nuclear model.

The key quantity of Equation (2.51c) can be obtained by using Equation (2.52a) as

$$\hat{\mu} = \mu_n - \mu_p = 4(1-2Y_p)F_{\text{sym}}(n,T). \tag{2.54}$$

This equation is similar to that obtained for cold catalyzed nuclear matter by replacing $E_{\text{sym}}(n)$ with $F_{\text{sym}}(n,T)$.

It is intuitive to assume, based mainly on Equations (2.52a) and (2.52b), that the entropy must also exhibit a quadratic dependence on asymmetry parameter I, that is according to the parabolic law (Moustakidis, 2009)

$$S(n,T,I) = S(n,T,I=0) + I^2 S_{\text{sym}}(n,T), \tag{2.55}$$

where

$$\begin{aligned} S_{\text{sym}}(n,T) &= S(n,T,I=1) - S(n,T,I=0) \\ &= \frac{1}{T}(E_{\text{sym}}(n,T) - F_{\text{sym}}(n,T)). \end{aligned} \tag{2.56}$$

2.2.1.1 Leptons contribution to equation of state

In principle the hot nuclear matter is composed, except by the two baryons (protons and neutrons), by photons and leptons (electrons, muons, and neutrinos), and also from their corresponding anti-particles (positrons, anti-muons, and anti-neutrinos).

Nuclear matter at high densities in order to be stable must be in chemical equilibrium for all reactions (including the weak interactions). β decay and electron capture would take place simultaneously as

$$n \longrightarrow p + e^- + \bar{\nu}_e, \quad \text{and} \quad p + e^- \longrightarrow n + \nu_e. \tag{2.57}$$

Both of them affect directly the EoS as they change the electron per nucleon fraction Y_e. By assuming that the generated neutrinos have already left the system, the absence of neutrino-trapping has a dramatic effect on the EoS as a significant change on the values of the proton fraction Y_p is in order (Takatsuka, 1996; Takatsuka et al., 1994). The absence of neutrinos implies that

$$\hat{\mu} = \mu_n - \mu_p = \mu_e. \tag{2.58}$$

In general, it is considered that nuclear matter contains neutrons, protons, electrons, and muons. Muons decay to electrons as (Suh and Mathews, 2001)

$$\mu^- \longrightarrow e^- + \nu_\mu + \bar{\nu}_e, \tag{2.59}$$

but when the Fermi energy of the electrons approaches the muon rest mass $m_\mu \simeq 105.7$ MeV (due to their rest mass, it is expected to merely appear at the saturation nuclear density), it becomes energetically favorable for electrons at the top level of Fermi sea to decay into muons with neutrinos and anti-neutrinos escaping from the star. Hence, above some density, muons and electrons are in equilibrium state

$$\mu^- \leftrightarrow e^-, \tag{2.60}$$

assuming that the neutrinos left the star. These particles are considered to be in a β-equilibrium state, where the following relations hold

$$\mu_n = \mu_p + \mu_e, \quad \text{and} \quad \mu_e = \mu_\mu. \tag{2.61}$$

The neutrality charge condition is also satisfied through the relation

$$n_p = n_e + n_\mu. \tag{2.62}$$

The density of leptons (electrons and muons) is expressed through the relation

$$n_l = \frac{2}{(2\pi)^3} \int \frac{d^3k}{1 + \exp\left[\frac{\sqrt{\hbar^2 k^2 c^2 + m_l^2 c^4} - \mu_l}{T}\right]}. \tag{2.63}$$

Equations (2.54), and (2.61) - (2.63) are solved in a self-consistent way for the calculation of the proton fraction Y_p, the lepton fractions Y_e, and Y_μ, as well as the lepton chemical potentials μ_e, and μ_μ as functions of the baryon density n, for various values of the temperature T.

Afterward, the energy density and pressure of leptons is calculated through the following formulae

$$\mathcal{E}_l(n_l,T) = \frac{2}{(2\pi)^3}\int \frac{d^3k\ \sqrt{\hbar^2k^2c^2+m_l^2c^4}}{1+\exp\left[\frac{\sqrt{\hbar^2k^2c^2+m_l^2c^4}-\mu_l}{T}\right]}, \tag{2.64}$$

$$P_l(n_l,T) = \frac{1}{3}\frac{2(\hbar c)^2}{(2\pi)^3}\int \frac{1}{\sqrt{\hbar^2k^2c^2+m_l^2c^4}} \times \frac{d^3k\ k^2}{1+\exp\left[\frac{\sqrt{\hbar^2k^2c^2+m_l^2c^4}-\mu_l}{T}\right]}. \tag{2.65}$$

The chemical potentials of electrons and muons, which are equal, according to Equations (2.54) and (2.61) are

$$\mu_e = \mu_\mu = \mu_n - \mu_p = 4I(n,T)F_{\text{sym}}(n,T). \tag{2.66}$$

Equation (2.66) is crucial for the calculation of the proton fraction as a function of the baryon density and for various temperatures. The EoS of hot nuclear matter in β-equilibrium state is provided through the calculation of the total energy density $\mathcal{E}_\text{t}$ as well as the total pressure P_t. The total energy density is given by

$$\mathcal{E}_\text{t}(n,T,I) = \mathcal{E}_b(n,T,I) + \sum_l \mathcal{E}_l(n,T,I) + \sum_{\bar{l}} \mathcal{E}_{\bar{l}}(n,T,I) + \mathcal{E}_\gamma(n,T), \tag{2.67}$$

where $\mathcal{E}_b(n,T,I)$, $\mathcal{E}_l(n,T,I)$, $\mathcal{E}_{\bar{l}}(n,T,I)$, and $\mathcal{E}_\gamma(n,T)$ are the contributions of baryons, particle and anti-particles of leptons, and photons, respectively. The total pressure is

$$P_\text{t}(n,T,I) = P_b(n,T,I) + \sum_l P_l(n,T,I) + \sum_{\bar{l}} P_{\bar{l}}(n,T,I) + P_\gamma(T), \tag{2.68}$$

where $P_b(n,T,I)$ is the contribution of baryons (see Equation (2.49))

$$P_b(n,T,I) = T\sum_{\tau=p,n} s_\tau(n,T,I) + \sum_{\tau=n,p} n_\tau\mu_\tau(n,T,I) - \mathcal{E}_b(n,T,I), \tag{2.69}$$

while $P_l(n,T,I)$, $P_{\bar{l}}(n,T,I)$, and $P_\gamma(T)$ are the contributions of particles and anti-particles of leptons, and photons, respectively.

It is worth mentioning that, in principle, it is necessary to include photons and anti-particles, which are in thermal equilibrium with the other constituents of the hot nuclear matter. However, in the present study, the relative particles will be excluded since their contribution is negligible (Takatsuka et al., 1994).

2.2.2 Isothermal temperature profile

In the present study, it is considered that nuclear matter consists only of neutrons, protons, and electrons. Therefore, electrons are the only leptons that contribute to the energy density and pressure. Assuming that for each value of temperature the proton fraction is a well known function of the baryon density, $Y_p = Y_p(n)$, the total energy density reads as

$$\mathcal{E}_\text{t}(n,T,Y_p) = \mathcal{E}_b(n,T,Y_p) + \mathcal{E}_e(n,T,Y_p), \tag{2.70}$$

where

$$\mathcal{E}_b(n,T,Y_p) = nF_{\rm PA} + nTS_{\rm PA}, \tag{2.71}$$

$\mathcal{E}_e(n,T,Y_p)$ is given by Equation (2.64) replacing the leptons with electrons and μ_e from Equation (2.66), and in the frame of the parabolic approximation $F_{\rm PA}$ and $S_{\rm PA}$ are given by the Equations (2.52a) and (2.55), respectively. In addition, the total pressure reads as

$$P_{\rm t}(n,T,Y_p) = P_b(n,T,Y_p) + P_e(n,T,Y_p), \tag{2.72}$$

where

$$P_b(n,T,Y_p) = n^2 \frac{\partial F_{\rm PA}(n,T,Y_p)}{\partial n}\bigg|_{T,n_i}, \tag{2.73}$$

and $P_e(n,T,Y_p)$ is given by Equation (2.65) replacing the leptons with electrons and μ_e from Equation (2.66).

Henceforth, in the present study, Equation (2.70) for the energy density and Equation (2.72) for the pressure, are the ingredients for the construction of isothermal EoSs of hot nuclear matter in a β-equilibrium state.

2.2.2.1 Thermal index

Except proto-neutron stars and supernovae, hot EoSs find their place in neutron stars mergers where the increase of temperature is rather significant. A usual treatment, in order to study the effects of temperature on neutron stars and to include thermal effects in neutron stars mergers simulations, is the effective thermal index defined as (Constantinou et al., 2014, 2015)

$$\Gamma_{\rm th}(n) = 1 + \frac{P_{\rm th}(n)}{\mathcal{E}_{\rm th}(n)}, \tag{2.74}$$

where $P_{\rm th}(n)$ and $\mathcal{E}_{\rm th}(n)$ are the pressure and energy density contribution to the cold EoS due to temperature. More precisely, for a specific value of temperature, the right-hand side terms of Equation (2.74) are defined as

$$P_{\rm th}(n) = P(T,n) - P(T=0,n), \tag{2.75a}$$
$$\mathcal{E}_{\rm th}(n) = \mathcal{E}(T,n) - \mathcal{E}(T=0,n). \tag{2.75b}$$

It has to be noted that although Equation (2.74) is artificially and not self-consistently constructed, it has been widely used in order to introduce the effects of temperature in isothermal EoSs (Bauswein et al., 2010).

In most cases, the values of the thermal index are taken to be constant, an approximation which seems to be unrealistic since a high density dependence is suggested by the interactions of cold catalyzed matter.

2.2.3 Isentropic temperature profile and neutrino trapping

In the case of the isentropic profile, it is considered that the entropy per baryon and lepton fraction are fixed in the interior of proto-neutron star. In particular, according to Equation (2.57), it is considered that neutrinos are trapped in the interior of the star, a process which leads to a dramatic increase of the proton fraction. Now, the chemical equilibrium can be expressed in terms of the chemical potentials for the four species

$$\mu_n + \mu_{\nu_e} = \mu_p + \mu_e. \tag{2.76}$$

Obviously, the charge neutrality demands $Y_p = Y_e$, while the total fraction of leptons reads as $Y_l = Y_e + Y_{\nu_e}$. Moreover, the chemical equilibrium leads to the expression

$$\mu_e - \mu_{\nu_e} = \mu_n - \mu_p = 4(1 - 2Y_p)F_{\text{sym}}(n, T). \tag{2.77}$$

Similar to isothermal profile, one can solve self-consistently the relevant equations in order to calculate the density and temperature dependence of proton and neutrino fractions, as well as the corresponding chemical potentials for a fixed value of the total entropy per baryon. However, in order to avoid computational complications (arising mainly from the system of the coupled integral equations), the approximation introduced by Takatsuka et al. (Takatsuka et al., 1994) is followed. In particular, it was find that the proton fraction is well approximated (within 3% accuracy) by the empirical formula $Y_p \simeq 2/3Y_l + 0.05$. The ingredients for the construction of isentropic EoSs are given by Equations (2.67) and (2.68).

Two important quantities related to the measure of stiffness of the EoS and, consequently, the stability of proto-neutron stars are the adiabatic index, defined as

$$\Gamma = \frac{n}{P}\frac{\partial P}{\partial n}\bigg|_S, \tag{2.78}$$

and the speed of sound given by (Landau and Lifshitz, 1969)

$$\frac{c_s}{c} = \sqrt{\frac{\partial P}{\partial \mathcal{E}}}\bigg|_S. \tag{2.79}$$

CHAPTER 3

Stability of neutron stars

3.1 Cold neutron stars

Einstein's equations for a non-rotating neutron star are the most suitable tool to describe its macroscopic properties. In this case, the metric for curved spacetime is (Glendenning, 2000; Weber, 1996)

$$ds^2 = e^{2\nu}dt^2 - e^{2\lambda}dr^2 - r^2\left(d\theta^2 + \sin^2\theta d\phi^2\right), \tag{3.1}$$

where ν and λ are metric functions that depend on the coordinates r. These equations are solved numerically, coupled to the hydrostatic equilibrium condition, and with source terms given by that of a perfect fluid. The latter is possible by neglecting sources of nonisotropic stresses, as well as viscous ones, and heat transport. The energy-momentum tensor that describes the perfect fluid is

$$T^{\mu\nu} = (\mathcal{E} + P)\, u^\mu u^\nu + P g^{\mu\nu}, \tag{3.2}$$

where u^μ and u^ν are the fluid's four-velocity. The thermodynamical quantities, energy density and pressure, are denoted as $\mathcal{E}$ and P, respectively, and $g^{\mu\nu}$ denotes the spacetime metric function.

The stability of cold non-rotating neutron stars is acquired by using the general properties of the central density as well as those of the mass–radius relation (Weinberg, 1972). In this case, the configuration is stable when the inequality $dM/dE_c > 0$ holds. However, it needs to be noted that this condition is just necessary but not sufficient.

3.2 Cold rotating neutron stars

Einstein's equations for a rigidly rotating neutron star are also the most suitable tool to describe its macroscopic properties. In this case, the metric for curved spacetime is (Glendenning, 2000; Weber, 1996)

$$ds^2 = -e^{2\nu}dt^2 + e^{2\phi}\left(d\varphi - N^\varphi dt\right)^2 + e^{2\omega}\left(dr^2 + r^2 d\theta^2\right), \tag{3.3}$$

where ν, ϕ, N^φ, and ω are metric functions that depend on the coordinates r and θ. As in the former case, these equations are solved numerically, coupled to the hydrostatic equilibrium condition, and with source terms given by that of a perfect fluid. The latter is possible by neglecting sources of nonisotropic stresses, as well as viscous ones, and heat transport. The energy-momentum tensor that describes the perfect fluid is

$$T^{\mu\nu} = (\mathcal{E} + P)\, u^\mu u^\nu + P g^{\mu\nu}, \tag{3.4}$$

where u^μ and u^ν are the fluid's four-velocity. The thermodynamical quantities, energy density and pressure, are denoted as $\mathcal{E}$ and P, respectively, and $g^{\mu\nu}$ denotes the spacetime metric function.

The stability of cold rotating neutron stars is acquired via the turning-point criterion, which is only a sufficient and not a necessary one. In fact, the neutral stability line is positioned to the left of the turning-point line in (M, ρ_c) space. The latter indicates that the star will collapse before reaching the turning-point line (Takami et al., 2011; Weih et al., 2017).

3.3 Hot neutron stars

The stability of hot neutron stars is acquired via a specific version of the secular instability criterion of Friedman et al. (Friedman et al., 1988), which follows Theorem I of Sorkin (Sorkin, 1982). We choose a continuous sequence of equilibria to be at a fixed baryon number $N_{\rm bar}$ and total entropy of the neutron star $S_{\rm t}^{\rm ns}$, and the extremal point of the stability loss is (Goussard et al., 1997)

$$\left.\frac{\partial J}{\partial n_b^c}\right|_{N_{\rm bar}, S_{\rm t}^{\rm ns}} = 0, \tag{3.5}$$

where J and n_b^c are the angular momentum and central baryon density of the star, respectively.

In addition, a turning point in the sequence occurs where three out of four derivatives, $\partial M_{\rm gr}/\partial n_b^c$, $\partial M_{\rm b}/\partial n_b^c$, $\partial J/\partial n_b^c$, and $\partial S_{\rm t}^{\rm ns}/\partial n_b^c$, where $M_{\rm gr}$ and $M_{\rm b}$ denote the gravitational and baryon mass, vanish (Kaplan et al., 2014; Marques et al., 2017). At this point, the turning-point theorem shows that the fourth derivative also vanishes, and the sequence has transitioned from stable to unstable.

The criterion for distinguishing secularly stable from unstable configurations is meaningful only for constant entropy per baryon or temperature (Marques et al., 2017). In our calculations, as the entropy per baryon and temperature are constant throughout the star, the other three criteria simultaneously vanish at the maximum mass configuration, which is the last stable point. It has to be mentioned that the rotating configuration with maximum mass and the one with maximum angular velocity do not generally coincide (Friedman and Stergioulas, 2013). However, the difference is very small, and it could not be detected within the precision of our calculations (Goussard et al., 1997).

CHAPTER 4

Construction of the equation of state

4.1 MDI-APR1 and MDI-APR2

The construction of the EoS is being performed with the MDI model and data originated from Akmal et al. (Akmal et al., 1998) for the A18+UIX (hereafter APR1) and A18+δv+UIX* (hereafter APR2). To be more specific, the data concerning the energy per particle of SNM and PNM for the two models, in the baryon density range $[0.04, 0.96]$ fm^{-3}, are employed. In order to achieve the best fitting into Akmal's data, the region of study is divided into three sections

- low density region $n \in [0.04, 0.2]$ fm^{-3},
- medium density region $n \in [0.2, 0.56]$ fm^{-3},
- high density region $n \in [0.56, 0.96]$ fm^{-3}.

In particular, in order to ensure the continuity in the EoSs, the continuity among the transition points for different regions is demanded. This method is used to calculate the coupling constants and the parameters for the ANM. The main properties of nuclear matter at the saturation density for the MDI-APR1 and MDI-APR2 EoSs, including also isovector quantities, are presented in Table 4.1. In addition, the schematic presentation of the MDI-APR1 and MDI-APR2 EoSs is presented in Figure 4.1.

Table 4.1: Properties of nuclear matter (NM) for APR-1 and APR-2 EoSs.

Properties of NM	APR-1	APR-2	Units
$L_{\rm pa}$	63.18	57.43	MeV
$Q_{\rm pa}$	482.34	568.91	MeV
$K_{\rm pa}$	-103.70	-118.78	MeV
$E_{\rm sym_{pa}}$	33.61	33.59	MeV
$L_{\rm f}$	63.31	57.40	MeV
$Q_{\rm f}$	450.50	538.44	MeV
$K_{\rm f}$	-88.26	-99.81	MeV
$E_{\rm sym_f}$	32.74	32.53	MeV
Q_0	-581.27	-581.27	MeV
K_0	256.40	256.40	MeV
m^*_τ/m_τ	0.79	0.79	

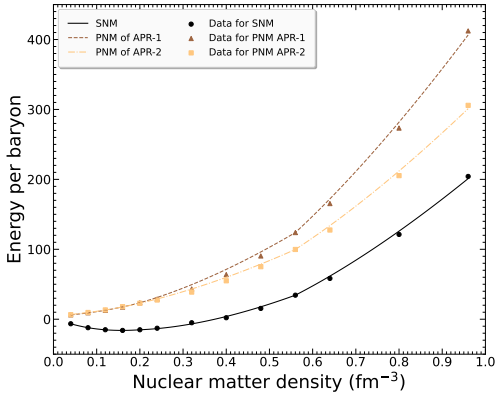

Figure 4.1: Symmetric nuclear matter and pure neutron matter fits for APR EoSs using Akmal's (Akmal et al., 1998) data and the MDI model. The SNM is presented with the circles and the solid line, the APR-1 PNM is presented with the triangles and the dashed line, and the APR-2 PNM is presented with the squares and the dashed-dotted line.

4.2 MDI+APR1

The construction of the EoSs for the description of neutron stars is based on the MDI model and the data provided by Akmal et al. (Akmal et al., 1998) for the APR-1 EoS (hereafter MDI+APR1). Its schematic presentation is shown in Figure 4.2. This model, as a microscopic one, is available via ab initio calculations. The explicit use of the MDI model is due not only to its numerous advantages but also to its ability to express the energy per particle as a function of the density and momentum. This property is the one that allows the extension of its parameterization to a finite temperature that is suitable for studying processes sensitive to thermal effects, including core-collapse supernovae, protoneutron stars, neutron star mergers, etc.

Using this parameterization one cold EoS, 10 hot EoSs based on various temperatures in the range $[1, 60]$ MeV, and nine hot EoSs based on various lepton fractions and entropies per baryon in the ranges $[0.2, 0.4]$ and $[1, 3]$ k_B, respectively, have been constructed. The advantages of the MDI+APR1 EoS are (a) it reproduces with high accuracy the properties of SNM at the saturation density (including isovector quantities K_0 and Q_0) which are shown in Table 4.2; (b) it correctly reproduces the microscopic calculations of the Chiral model (Hebeler and Schwenk, 2010) for pure neutron matter (PNM;for low densities) and the results of *state-of-the-art* calculations of Akmal et al. (Akmal et al., 1998) (for high densities); and (c) it predicts a maximum neutron star mass at least higher than the observed ones (Antoniadis et al., 2013; Arzoumanian et al., 2018; Cromartie et al., 2019; Demorest et al., 2010; Fonseca et al., 2016; Linares et al., 2018). In addition, the predictions of PNM have been compared with those originating from the very recent state-of-the-art calculations (shaded region in Figure 4.2; Piarulli et al. (Piarulli et al., 2020)). From Figure 4.2, it is obvious that at very low densities, the agreement is quite satisfactory, while for higher densities, a deviation is exhibited. The latter is pointed out and discussed in Piarulli et al. (Piarulli et al., 2020).

For the solid crust region, two models have been adopted. For the cold case, the EoS of Feynman et al. (Feynman et al., 1949) and also Baym et al. (Baym et al., 1971) are employed, while for the finite temperature cases and the low-density region ($n_b \leq 0.08$ fm^{-3}), as well as the finite entropies per baryon and lepton fractions, the EoSs of Lattimer & Swesty (Lattimer and Swesty, 1991) (hereafter LS220) and the specific model corresponding to the incomprehensibility modulus at the saturation density of SNM $K_0 = 220$ MeV are used (https://www.stellarcollapse.org).

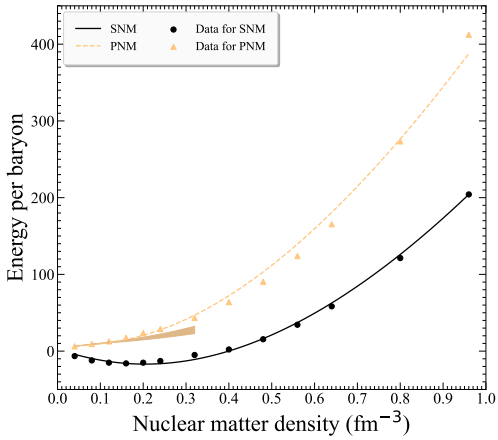

Figure 4.2: The SNM and PNM fits for the MDI+APR1 cold EoS. The SNM is presented by the circles and solid line, while the PNM is presented by the triangles and dashed line. The shaded region corresponds to benchmark calculations of the energy per particle of PNM extracted from Piarulli et al. (Piarulli et al., 2020).

Table 4.2: Properties of nuclear matter (NM) at the saturation density for the MDI+APR1 EoS.

Properties of NM	MDI+APR1	Units
L_{sym}	77.696	MeV
Q_{sym}	223.061	MeV
K_{sym}	0.016	MeV
E_{sym}	31.071	MeV
Q_0	-25.687	MeV
K_0	220.671	MeV
m^*_τ/m_τ	0.822	

CHAPTER 5

Neutron stars with cold, catalyzed matter

5.1 The selected equations of state

The EoSs that are used (Akmal et al., 1998; Balberg and Shapiro, 2000; Bombaci and Logoteta, 2018; Bowers et al., 1975; Chabanat et al., 1997; Douchin and Haensel, 2001; Farine et al., 1997; Gaitanos and Kaskulov, 2013, 2015; Hebeler et al., 2013; Heiselberg and Hjorth-Jensen, 2000; Koliogiannis and Moustakidis, 2019; Moustakidis and Panos, 2009; Pandharipande and Smith, 1975; Prakash et al., 1997; Sharma et al., 2015; Walecka, 1974; Wiringa et al., 1988) are consistent with the current observed limits of neutron star mass (Antoniadis et al., 2013; Arzoumanian et al., 2018; Cromartie et al., 2019; Demorest et al., 2010; Fonseca et al., 2016; Linares et al., 2018) and also with the one for frequency (Hessels et al., 2006). Figure 5.1 displays the gravitational mass versus the corresponding equatorial radius (hereafter radius) for the 23 EoSs at the non-rotating configuration, where the current observed limits are also presented. Moreover, the EoS with appearance of hyperons at high densities (FSU2H) (Tolos et al., 2017b) and the one suitable to describe quark stars (QS57.6) (Glendenning, 2000; Haensel et al., 2007), are also indicated.

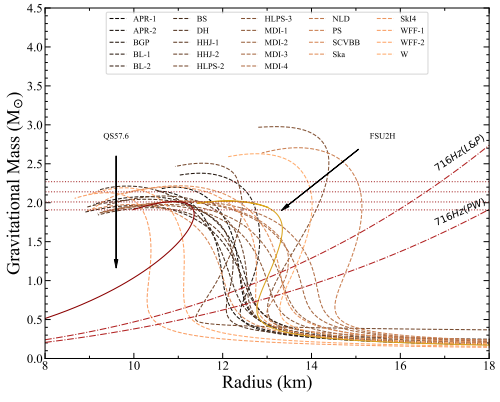

Figure 5.1: Mass - Radius diagram for the 23 EoSs at the non-rotating configuration. The observed limits of neutron star mass are presented with the horizontal dotted lines ($1.908M_{\odot}$, $2.01M_{\odot}$, $2.14M_{\odot}$ and $2.27M_{\odot}$). The observed limit of 716 Hz, from Lattimer and Prakash (L&P) (Lattimer and Prakash, 2004) and from the present work (PW) (for more details see Appendix 9.1), is presented with the curved dashed-dotted lines. The two indicated solid lines correspond to the EoS with appearance of hyperons at high densities (FSU2H) and the one suitable to describe quark stars (QS57.6).

5.2 Keplerian frequency

The derivation of the Keplerian frequency, in which a rotating star would shed matter at its equator, is a complicated problem. In Newtonian theory has its origin on the balance between gravitational and centrifugal forces and takes a very simple form. However, in General Relativity (GR) exhibits a more complicated dependence on the structure of the star through the interior metric as it is expressed as a self-consistency condition that must be satisfied by the solution to Einstein's equations.

It has been shown by Friedman et al. (Friedman et al., 1988) that the turning-point method, which is leading to the points of secular instability, can also be used in the case of uniformly rotating neutron stars. With this consideration, in a constant angular momentum sequence, the turning-point of a sequence of configurations with increasing central density, separates the secular stable from unstable configuration and consequently, the condition

$$\left.\frac{\partial M(\varepsilon_c, J)}{\partial \varepsilon_c}\right|_{J=\text{constant}} = 0, \tag{5.1}$$

where ε_c is the energy density in the center of the neutron star and J is the angular momentum, defines the possible maximum gravitational mass. In general, gravitational (gr) and rest mass (rm) are defined as (Haensel et al., 2007)

$$M_{\text{gr}} = \int_0^{\text{R}} 4\pi r^2 \epsilon(r) \mathrm{d}r, \tag{5.2}$$

$$M_{\text{rm}} = m_A \int_0^{\text{R}} 4\pi r^2 \frac{n(r)}{\left(1-\frac{2GM(r)}{c^2 r}\right)^{1/2}} \mathrm{d}r, \tag{5.3}$$

where m_A is the baryonic mass and $n(r)$ is the baryon number density.

The absence of analytical solutions for rotating neutron stars leads to numerical estimations for the Keplerian frequency. A significant number of empirical formulas for the Keplerian frequency had been produced along the years. The formula is given by (Haensel et al., 2009; Haskell et al., 2018)

$$f_k = \mathcal{C}_\alpha \left(\frac{M^\alpha_{\text{max}}}{M_\odot}\right)^{1/2} \left(\frac{10\,\text{km}}{R^\alpha_{\text{max}}}\right)^{3/2} = \mathcal{C}_\alpha x^\alpha_{\text{max}}\ (\text{Hz}), \tag{5.4}$$

where

$$x^\alpha_{\text{max}} = \left(\frac{M^\alpha_{\text{max}}}{M_\odot}\right)^{1/2} \left(\frac{10\,\text{km}}{R^\alpha_{\text{max}}}\right)^{3/2}, \tag{5.5}$$

and α (st : static, rot : rotating, rm; rot : rest mass at rotating configuration) takes the form of the corresponding configuration. Although this relation is well established, the unknown parameter ($\mathcal{C}_\alpha$) depends highly on the various approximations and of course the selected EoSs.

It is worth pointing out that while the maximum rotation rate is an increasing function of the EoS's softness, the maximum mass is a decreasing one (considering a fixed mass). Therefore, for a fixed gravitational mass M the softer EoS predicts the lower value of the radius R and consequently, leads to higher values for f_k. The latter it had been already noticed by Lattimer et al. (Lattimer et al., 1990). These two constraints restrict the EoS in a narrow region. The above statement is one of the main subjects of the present study.

5.2.1 The Keplerian frequency, the maximum gravitational mass, and the corresponding radius of non-rotating neutron stars

We studied the Keplerian frequency in correlation with the bulk properties of a non-rotating neutron star and specifically on its gravitational mass and the corresponding radius at the maximum mass configuration, using Equation (5.4) and $\alpha = \text{st}$.

In Figure 5.2, the relation (5.4) with the corresponding parametrization, which can be found in Table 5.1, is presented, updating the work of Haensel et al. (Haensel et al., 2009). The value of the parameter $\mathcal{C}_{st}$ is in very good agreement with the current EoSs to a linear term.

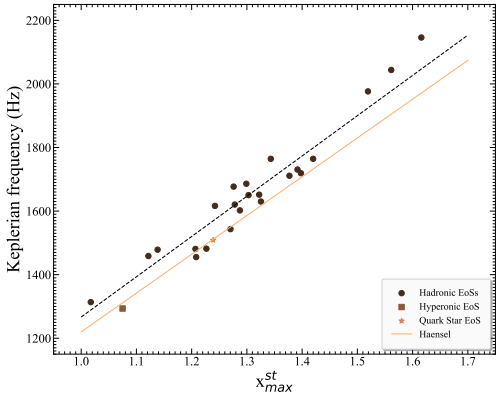

Figure 5.2: Keplerian frequency dependence on the quantity $x^{\text{st}}_{\text{max}}$ for the 23 EoSs (for more details see Equation (5.5)). Dashed line corresponds to the best linear trend that fits the data. The data from 23 hadronic EoSs are also presented with circles. The hyperonic EoS is indicated with the square and the quark star EoS with the star. The solid line marks the work of Haensel et al. (Haensel et al., 2009).

Table 5.1: Parametrization of Equation (5.4) for the different configurations. The relative error (r.e.) between the data and fits is also presented.

α	$\mathcal{C}_\alpha$	r.e.%	$\mathcal{C}_{\text{Haensel}}$
st	1266.68	5.6	1220
rot	1781.90	≤ 1	–
rm;rot	1644.75	2.2	–

5.2.2 The Keplerian frequency, the maximum gravitational mass, and the corresponding radius of maximally rotating neutron stars

An interesting relation is also the one between the Keplerian frequency and the macroscopic properties of maximally-rotating neutron stars (maximum gravitational mass and the corresponding radius). Using Equation (5.4) and $\alpha = \text{rot}$, it is remarkable that in this scenario, as Figure 5.3(a) shows, the linear fit between these quantities (f_k, $x^{\text{rot}}_{\text{max}}$) leads to nearly perfect results. The parametrization can be found in Table 5.1.

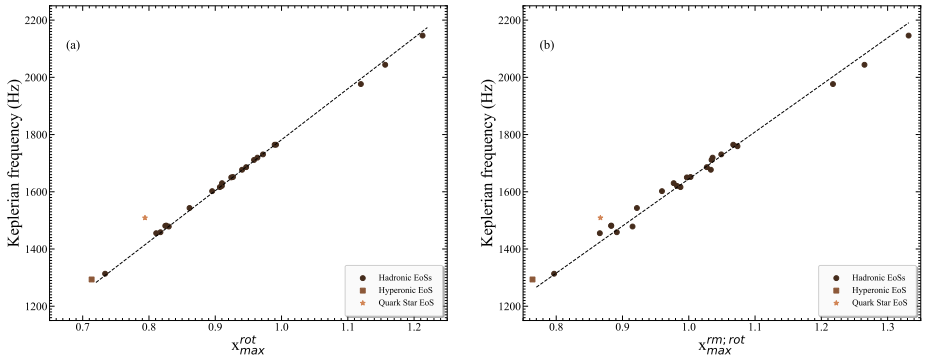

Figure 5.3: Keplerian frequency dependence on the quantity (a) $x_{\rm max}^{\rm rot}$ and (b) $x_{\rm max}^{\rm rm;rot}$ for the 23 EoSs (for more details see Equation (5.5)). Dashed lines correspond to the best linear trend that fits the data. The data from 23 hadronic EoSs are also presented with circles. The hyperonic EoS is indicated with the square and the quark star EoS with the star.

5.2.3 The Keplerian frequency, the maximum rest mass, and the corresponding radius of non-rotating neutron stars

In the macroscopic properties of a neutron star, rest mass plays an important role. In order to understand the effects of the rest mass on the Keplerian sequence, the Keplerian frequency dependence on the rest mass and the corresponding radius using Equation (5.4) and $\alpha = {\rm rm; rot}$ has been studied.

In Figure 5.3(b) is displayed the almost linear relation that holds on between these two quantities (f_k, $x_{\rm max}^{\rm rm;rot}$), enhancing with this way the existence of a relation between rest mass and gravitational mass in neutron stars at the Keplerian frequency. The parametrization can be found in Table 5.1.

5.2.4 Rest mass and gravitational mass at the maximum mass configuration of maximally rotating neutron stars

As a follow-up to Section 5.2.3, the rest mass dependence on the gravitational mass at the maximum mass configuration for the Keplerian frequency has been studied. Figure 5.4 displays the almost linear relation between these two quantities, as expected from Section 5.2.3.

The relation which describes our data is given via the form

$$\left(\frac{M_{\rm max}^{\rm rm;rot}}{M_\odot}\right) = 1.17 \left(\frac{M_{\rm max}^{\rm gm;rot}}{M_\odot}\right), \tag{5.6}$$

(the maximum possible error is less than 3.3%) concluding that the percentage difference between these quantities is around 17%.

5.3 Moment of inertia and eccentricity

Rotating neutron stars can provide us with more quantities than non-rotating ones that we could study. Among them, there is the moment of inertia and eccentricity. Both these quantities can give us information about the deformation of the mass while its spinning.

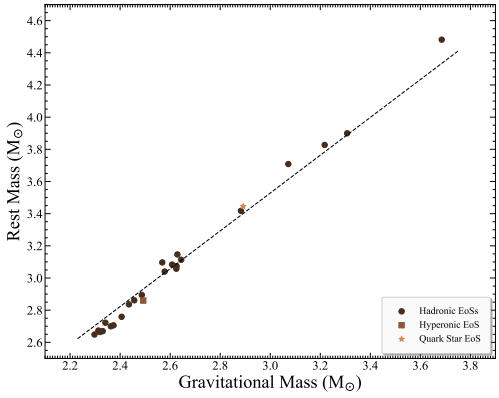

Figure 5.4: Rest mass dependence on the gravitational mass of a maximally-rotating neutron star at the maximum mass configuration. Dashed line corresponds to the best linear trend that fits the data. The data from 23 hadronic EoSs are also presented with circles. The hyperonic EoS is indicated with the square and the quark star EoS with the star.

The moment of inertia (Cipolletta et al., 2015; Stergioulas, 2003), which have a prominent role in pulsar analysis, is defined as

$$I = \frac{J}{\Omega}, \tag{5.7}$$

where J is the angular momentum and Ω is the angular velocity. This property of neutron stars quantifies how fast an object can spin with a given angular momentum.

In particular, the moment of inertia dependence on the gravitational mass for the Keplerian sequence has been studied. Figure 5.5(a) displays that all EoS present similar behavior. For this reason, inside Figure 5.5(a), the moment of inertia values corresponding to maximum mass configuration versus the corresponding gravitational mass are plotted. A relation, given by the formula

$$I^{\rm rot}_{\rm max} = -1.568 + 0.883 \exp\left[0.7\left(\frac{M^{\rm gm;rot}_{\rm max}}{M_\odot}\right)\right]\left(10^{45}\ {\rm gr\ cm^2}\right), \tag{5.8}$$

describes with high accuracy our data, concluding that moment of inertia, at the maximum mass configuration for the Keplerian frequency, can provide a universal relation between moment of inertia and the corresponding gravitational mass.

The dimensionless moment of inertia dependence on the corresponding compactness parameter (Lattimer and Schutz, 2005), has also been studied, which, in general, it is defined as

$$\beta = \frac{GM}{Rc^2}, \tag{5.9}$$

where R corresponds to the equatorial radius of neutron star.

Figure 5.5(b) presents a window where moment of inertia and compactness parameter can lie (shadowed region), constraining both these quantities. There is an empirical relation, derived from the data, that can describe this window. The form of this empirical relation is

$$I/MR^2 = \alpha_1 + \alpha_2\beta + \alpha_3\beta^2 + \alpha_4\beta^3 + \alpha_5\beta^4, \tag{5.10}$$

where the coefficients for the two edges are shown in Table 5.2. It is clear from Figure 5.5(b) and Equation (5.10) that if we have a measurement of moment of inertia, or compactness parameter, we could extract the interval where the other parameter can lie.

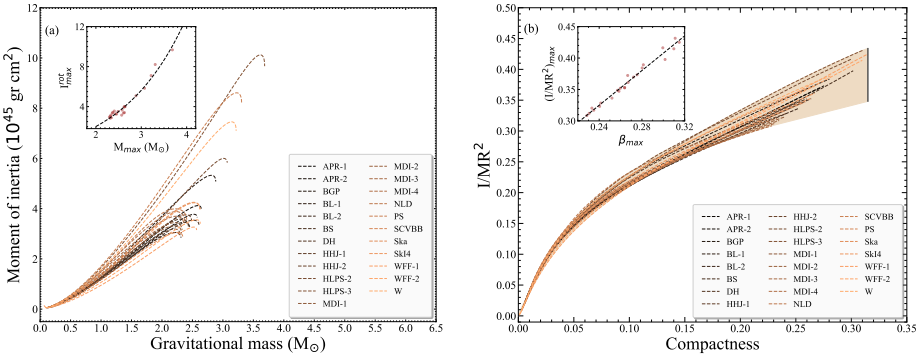

Figure 5.5: Moment of inertia dependence (a) on the gravitational mass and (b) on the compactness parameter of a maximally-rotating neutron star for the 23 EoSs. Dashed lines in the inside figures correspond to the best fit in each case. The data at the maximum mass configuration are also presented with circles in the inside figures.

Table 5.2: Coefficients of the empirical relation (5.10) for the two edges of the window presented in Figure 5.5(b).

Edges	α_1	α_2	α_3	α_4	α_5
Upper	0.005	4.01	-24.79	86.66	-110.33
Lower	0.005	3.38	-17.45	49.68	-55.36

As a consequence, by constraining simultaneously these two quantities, constraints could be imposed on the radius of neutron stars, which still remains an open problem.

From Figure 5.5(b), it is displayed that all EoSs present similar behavior. For this reason, inside Figure 5.5(b), the dimensionless moment of inertia values corresponding to maximum mass configuration versus the corresponding compactness parameter are plotted. A relation, given by the formula

$$\left(I/MR^2\right)_{\rm max} = -0.006 + 1.379\beta_{\rm max}, \tag{5.11}$$

describes with high accuracy our data, concluding that dimensionless moment of inertia, at the maximum mass configuration for the Keplerian frequency, can provide a universal relation between dimensionless moment of inertia and the corresponding compactness parameter.

Eccentricity, is the main quantity that is related to the deformation of the star. Rapid rotation deforms the models of equilibrium and in order to see how these models change, the calculation of the eccentricity is performed, which is given by the form (Cipolletta et al., 2015)

$$\epsilon = \sqrt{1 - \left(\frac{r_{\rm pol}}{r_{\rm eq}}\right)^2}, \tag{5.12}$$

where the $r_{\rm pol}$ and $r_{\rm eq}$ are the polar and equatorial radius of the star, respectively.

For a schematic presentation of the energy inside a neutron star, Figure 5.6 presents the contours of constant density of a neutron star model with central density equals to 10^{15} gr cm^{-3}, both in the non-rotating case and in the rotating one with frequency equals to the Keplerian frequency. For the sake of example the APR-1 EoS is being used.

Performing the same analysis as for moment of inertia, the eccentricity dependence on the gravitational mass for the Keplerian sequence and the eccentricity values corresponding to

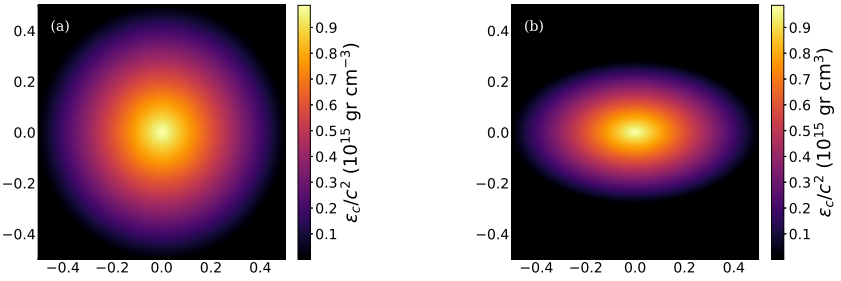

Figure 5.6: Contours of constant density of a neutron star model with central density equals to 10^{15} gr cm^{-3}, both (a) in the non-rotating case and (b) in the rotating one with frequency equals to the Keplerian frequency for the APR-1 EoS. The axis had been scaled in a way that the maximum radius corresponds to 0.5.

maximum mass configuration on the corresponding gravitational mass, have been studied, as Figure 5.7 shows. A relation, given by the formula

$$\epsilon_{\max} = 0.799 + 0.01 \left(\frac{M_{\max}}{M_\odot} \right), \tag{5.13}$$

describes with high accuracy our data, concluding that eccentricity, at the maximum mass configuration for the Keplerian frequency, is an EoS-independent property.

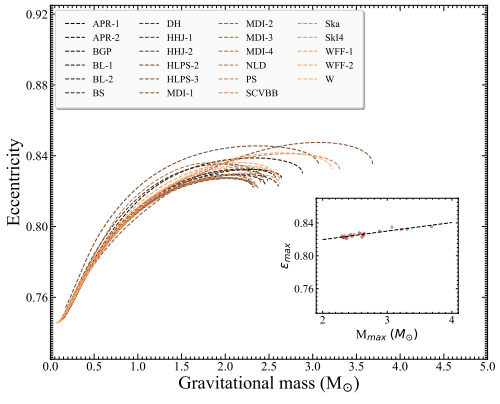

Figure 5.7: Eccentricity dependence on the gravitational mass of a maximally-rotating neutron star for the 23 EoSs. (Inside) The eccentricity values as a function of the corresponding gravitational mass at the maximum mass configuration. Dashed line in the inside figure corresponds to the best fit. The data at the maximum mass configuration are also presented with circles in the inside figure.

5.4 Kerr parameter

The Kerr space-time provided from the Einstein's field equations, give us the so-called Kerr black holes (Cipolletta et al., 2015; Lo and Lin, 2011). These rotating black holes can be fully described from the gravitational mass (M) and the angular momentum (J). In order to have a

meaningful Kerr black hole, the relation $J \geq GM^2/c$ (Kerr bound) must hold, or otherwise, we have a naked singularity. A naked singularity is a black hole without a horizon and can be considered as closed timelike curves, where causality would be violated. While there is no rigorous proof from Einstein's field equations, the cosmic-censorship conjecture implies that a generic gravitational collapse cannot form a naked singularity (Virbhadra, 2009; Virbhadra and Ellis, 2000, 2002; Virbhadra and Keeton, 2008). This is the reason why the astrophysical black holes should satisfy the Kerr bound (Cipolletta et al., 2015; Lo and Lin, 2011).

The gravitational collapse of a massive rotating neutron star, constrained to mass-energy and angular momentum conservation, creates a black hole with almost the same mass and angular momentum as the prior neutron star. In this case, an important quantity to study, directly related to black holes as well as neutron stars, is the dimensionless angular momentum (Chakrabarti et al., 2014b), which is defined as

$$j = \frac{cJ}{GM_\odot^2}, \tag{5.14}$$

and it is known as dimensionless spin parameter. As a consequence of this parameter, we can define a new one, starting from the parameter α, which is the angular momentum in units of mass and it is given by the form (Paschalidis and Stergioulas, 2017)

$$\alpha \equiv \frac{J}{M} = j\frac{GM_\odot^2}{c}\frac{1}{M}. \tag{5.15}$$

As a follow, using Equation (5.15), the well-known *Kerr parameter* takes the form

$$\mathcal{K} = \frac{\alpha}{M}\frac{c}{G} = j\left(\frac{M_\odot}{M}\right)^2. \tag{5.16}$$

The dependence of this parameter on the gravitational mass at the Keplerian sequence can be seen in Figure 5.8.

Although the meaning of this parameter in black-holes physics is so interesting and fundamental (there is a maximum value at 0.998 (Thorne, 1974)), that's also the case for other compact objects such as neutron stars. In order to find a way to constrain the value of the Kerr parameter

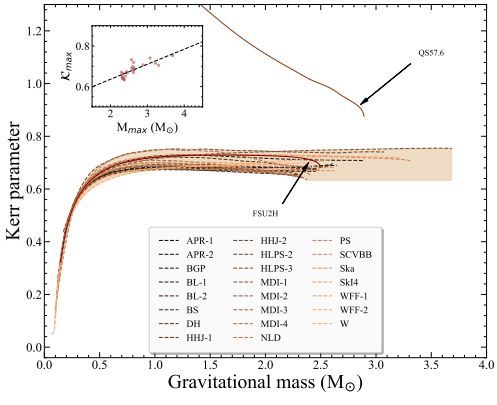

Figure 5.8: Kerr parameter dependence on the gravitational mass of a maximally-rotating neutron star. (Inside) The Kerr parameter values as a function of the corresponding gravitational mass at the maximum mass configuration. The dashed line in the inside figure corresponds to the best linear trend. The data at maximum mass configuration for the 23 hadronic EoSs are presented with circles in the inside figure. FSU2H and QS57.6 EoSs are also indicated with the two solid lines.

in neutron stars, the dependence of this parameter on the total gravitational mass for the Keplerian sequence has been studied. Figure 5.8 presents that the maximum value of the Kerr parameter for neutron stars is around 0.75. While there is a number of EoSs that hold on near this value, the maximum value achieved from HLPS-3. This EoS is the stiffest equation that we have and produces maximum mass greater than all the others. Strictly speaking, if we consider this EoS as the one that produces the maximum possible mass in the maximum mass configuration at the Keplerian sequence, then we could constrain the maximum value of the Kerr parameter in neutron stars.

Figure 5.8 displays also a window (shadowed region) where the Kerr parameter can lie. There is an empirical relation, derived from the data, that can describe this window. The form of this empirical relation is

$$\mathcal{K} = d_1 + d_2 \coth\left[d_3\left(\frac{M_{\rm max}}{M_\odot}\right)\right], \tag{5.17}$$

where the coefficients for the two edges are shown in Table 5.3. It is clear from Figure 5.8 and Equation (5.17) that if we have a measurement of gravitational mass, or spin parameter, we could extract the interval where the other parameter can lie.

Table 5.3: Coefficients of the empirical relation (5.17) for the two edges of the window presented in Figure 5.8.

Edges	d_1	d_2	d_3
Upper	0.86	-0.12	1.54
Lower	0.86	-0.21	2.67

As a consequence, by measuring accurately and simultaneously these two quantities, we could impose constraints on the EoS.

In addition, in Figure 5.8, the maximum values of the Kerr parameter versus the corresponding gravitational mass are plotted. It seems that a linear relation holds between these quantities, given by the equation

$$\mathcal{K}_{\rm max} = 0.488 + 0.074\left(\frac{M_{\rm max}}{M_\odot}\right). \tag{5.18}$$

There are two important reasons for constraining the Kerr parameter at neutron stars: First, the existence of a maximum value at the Kerr parameter, can lead to possible limits for the compactness on neutron stars; strictly speaking, the maximum value of the Kerr parameter for neutron stars implies a maximum value on the possible maximum mass of rotating neutron stars in the universe and second, can be a criteria for determining the final fate of the collapse of a rotating compact star (Lo and Lin, 2011).

Finally, it is clear from Figure 5.8 that the Kerr parameter dependence on the gravitational mass of a quark star is quite different than the one on neutron stars. The Kerr parameter of quark stars can be significantly larger than the maximum value of this parameter on neutron stars. In case of the hypeonic EoS, the dependence between gravitational mass and the Kerr parameter exhibits similar behavior with the hadronic ones.

5.5 Constant rest mass sequences

The rest mass sequences, also called as time evolutionary sequences, based on an EoS, are roughly horizontal lines that extend from the Keplerian sequence to the non-rotating end point or at the axisymmetric instability limit (Cook et al., 1992, 1994a,b). The latter depends only

on the rest mass value of the selected EoS. For a given EoS, the sequences that are below the rest mass value that corresponds to the maximum mass configuration at the non-rotating model, they have a non-rotating member, and as a consequence, are stable and terminate at the non-rotating model sequence. These sequences are called *normal sequences*. Above this value, none of the sequences have a non-rotating member. Instead, they are unstable and terminate at the axisymmetric instability limit and called *supramassive sequences*. The onset that extends from the maximum mass point on the non-rotating limit sequence to the one on the mass-shedding limit sequence is the quasi-radial stability limit. The total region that models are unstable is defined via the rest mass sequence that corresponds to the maximum mass configuration of the non-rotating model, as Figure 5.9 shows (shadowed region). Above this value, the models have masses larger than the maximum mass of the non-rotating model and in that case, are called supramassive models (Friedman and Stergioulas, 2013). It should be noted that models to the axisymmetric area of the shadowed region, which is not shown at the corresponding figures, are also unstable.

To be more specific, if a neutron star spin-up by accretion and becomes supramassive, then it would subsequently spin-down along the constant rest mass sequence until it reaches the axisymmetric instability limit and collapse to a black hole. There is a case where some relativistic stars could be born as supramassive ones, or even more, become one as a result of a binary merger. In this case, the star would be initially differentially rotating and collapse would be triggered by a combination between spin-down effect and viscosity (the force that driving the star to uniform rotation) (Friedman and Stergioulas, 2013).

Although the sequence with rest mass corresponding to the maximum mass configuration of the non-rotating model extends to the right area of the quasi-radial stability limit, the unstable one, it is the last one that has a stable part (half of the sequence terminates at the maximum mass configuration of the non-rotating model). While, below this sequence, all the remaining ones are unconditionally stable against gravitational collapse, above this sequence, all sequences would evolve toward catastrophic collapse to a black hole. Figure 5.9 displays that if we have a neutron star with rest mass in the white region, it would evolve toward stable configuration at the non-rotating sequence, but if we have a star in the shadowed region, it would subsequently

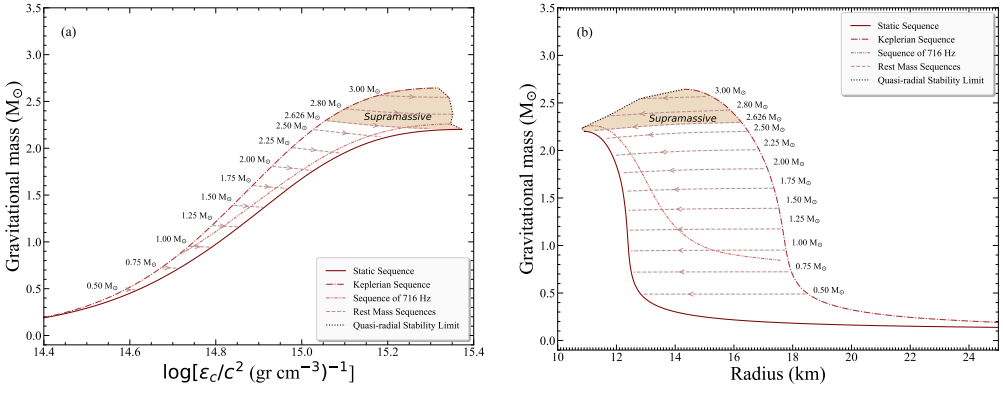

Figure 5.9: Normal and supramassive evolutionary sequences of constant rest mass are presented as the dependence of the (a) gravitational mass on the central energy density and (b) gravitational mass on the corresponding radius for the APR-1 EoS. Non-rotating case is presented with the solid curve while the maximally-rotating one with the dashed-dotted curve. Constant rest mass sequences are presented with the dashed lines, where the rest mass value is also noted. The 716 Hz limit is also presented with the dashed-dotted-dotted curve. The quasi-radial stability limit is presented with the dotted line.

spin-up and evolve toward catastrophic collapse to a black hole (Lasky et al., 2014; Ravi and Lasky, 2014; Shibata, 2003). The direction of evolution for constant rest mass sequences is noted with the existence of an arrow on them.

In all cases, neutron stars which evolve along normal evolutionary sequences, never spin-up as they lose angular momentum. In contradiction to neutron stars on normal evolutionary sequences, neutron stars on supramassive ones, because their unstable portion is always at higher angular velocity than the stable portion, at the same value of angular momentum, must spin-up with angular momentum loss in the neighborhood of the stability limit. If the neutron star is massive enough, then the evolutionary sequence (supramassive) exhibits an extended region where spin-up is allowed. This effect may provide us an observable precursor to gravitational collapse to a black hole (Cipolletta et al., 2015; Lo and Lin, 2011). The latter is shown clearly in Figure 5.10(a).

Following the concept from Figure 5.10(a), the last stable rest mass sequence (LSRMS) for the 23 hadronic EoSs, as shown in Figure 5.10(b), has been constructed. This sequence is the one that divides the stable from unstable region, or in other words, the normal from supramassive evolutionary sequences. In Figure 5.10(b), a window (shadowed region) where the last stable rest mass sequence can lie is presented, and in fact, because the last stable rest mass sequence is the one that corresponds to the maximum mass configuration at the non-rotating model, this is also the region where the EoS can lie, constraining simultaneously the spin parameter and the angular velocity. There is an empirical relation, derived from the data, that can describe this window. The form of this empirical relation is

$$\Omega = \left(b_1\mathcal{K} + b_2\mathcal{K}^2 + b_3\mathcal{K}^3\right) 10^4 \quad (\mathrm{s}^{-1}), \tag{5.19}$$

where the coefficients for the two edges are shown in Table 5.4. It is clear from Figure 5.10(b) and Equation (5.19) that if we have a measurement of angular velocity, or spin parameter, we could extract the interval where the other parameter can lie.

As a consequence, by constraining simultaneously these two quantities, we could significantly narrow the existing area of EoS.

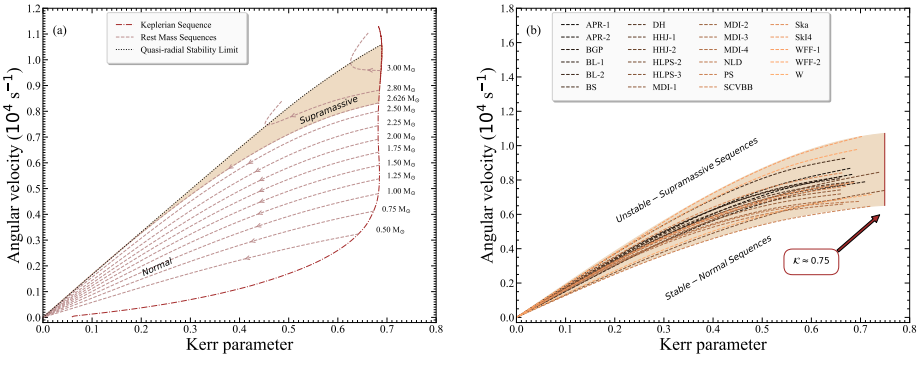

Figure 5.10: (a) Normal and supramassive evolutionary sequences of constant rest mass are presented as the dependence of the angular velocity on the Kerr parameter for the APR-1 EoS. Maximally-rotating case is presented with the dashed-dotted curve while the constant rest mass sequences are presented with the dashed curves, where the rest mass values are also noted. The quasi-radial stability limit is presented with the dotted curve. (b) Last stable rest mass sequences for the 23 EoSs as the dependence of angular velocity on the Kerr parameter. Supramassive and normal areas are shown to guide the eye. The maximum value of the Kerr parameter is also noted.

Table 5.4: Coefficients of the empirical relation (5.19) for the two edges of the window presented in Figure 5.10(b).

Edges	b_1	b_2	b_3
Upper	1.94	0.117	-1.058
Lower	1.35	-0.305	-0.449

5.6 Upper bound for density of cold baryonic matter

Although realistic EoSs are employed in order to solve numerically the equilibrium equations in neutron stars, analytical solutions are far from being insignificant. Useful information can be gained by the comparison between solutions of the Einstein's field equations with numerical solutions for different models of EoSs and the analytical solutions (Lattimer and Prakash, 2005). Two classes derive from analytical solutions: (a) normal neutron stars and (b) self-bound neutron stars. In the first case, the energy density vanishes at the surface where the pressure vanishes and, in the second one, the energy density is finite at the surface.

In this work only the first case scenario will be studied. It is most natural to solve numerically the TOV equations (Glendenning, 2000; Haensel et al., 2007; Shapiro and Teukolsky, 1983) by introducing an EoS describing the relation between pressure and density which is expected to describe the fluid interior. The other possibility is trying find out analytical solutions of TOV equations with the risk of obtaining solutions without physical interest. Actually, there are hundreds of analytical solutions of TOV equations (Delgaty and Lake, 1998; Kramer et al., 1980). However, just few of them are of physical interest. Moreover, there are only three that satisfy the criteria that the pressure and energy density vanish on the surface of the star and also that they both decrease monotonically with increasing radius. These three solutions are the Tolman VII, the Buchdahl and the Nariai IV (Moustakidis, 2017). The main difference between these analytical solutions is related to the maximum value of compactness at which they took effect. For example, the Buchdahl solution is applicable only for neutron stars with compactness up to the value $\beta = 0.17$ and, in general, produces soft EoSs. The Tolman VII solution leads to even stiffer EoSs and, consequently, is suitable to describe compact objects with compactness value up to $\beta = 0.34$ (for more details see Ref. (Moustakidis, 2017)). The Nariai IV solution exhibits similar behavior with the Tolman VII. In particular the Tolman VII is of great interest since it has the specific property that the pressure and density vanish at the surface of the star. It has been extensively employed to neutron star studies and the details of this analytical solution had been given in Appendix 9.2.

It has been shown by Lattimer et al. (Lattimer and Prakash, 2005) that the Tolman VII solution forms an absolute upper limit, which confirmed empirically by using a large number of EoSs, in density inside any compact star (see also Ref. (Lattimer and Prakash, 2011; Zhang and Li, 2019)). This is also the case for rotating stars with rotation rates up to the Keplerian (mass-shedding) rate.

At that time, the maximum masses of the existed EoSs were fully included in the region under the Tolman VII solution; the same holds for the rotating models. In recent years, new EoSs have been introduced and old ones, that could not describe the maximum observed neutron star mass (Antoniadis et al., 2013; Arzoumanian et al., 2018; Cromartie et al., 2019; Demorest et al., 2010; Fonseca et al., 2016; Linares et al., 2018), have been rejected. In this work, using a total of 23 hadronic EoSs that predict the observed maximum neutron star mass (Antoniadis et al., 2013; Arzoumanian et al., 2018; Cromartie et al., 2019; Demorest et al., 2010; Fonseca et al., 2016; Linares et al., 2018), it is confirmed that the Tolman VII curve marks the upper limit to the energy density inside a star but without taking into account the rotation (Tolman VII can describe the majority of them). When considering to add rotation to models, then this curve is not able to

describe anymore the new data as they shift, concerning the plotted area, up and left. For this reason, we propose here, that if there is a curve, like the Tolman VII solution, shifted to the right, that would be a suitable solution to fully describe the maximum energy density inside a star. In other words, the existence of this curve can help to form an absolute upper limit in density inside any compact object.

The proposed expression, described by the form

$$\frac{M}{M_{\odot}} = 4.25\sqrt{\frac{10^{15}\ \mathrm{gr\ cm^{-3}}}{\varepsilon_c/c^2}}, \tag{5.20}$$

can fully describe both the non-rotating and maximally-rotating configuration. The advantages of having this relation are that (a) it can describe the non-rotating configuration having as a guide the corresponding maximally-rotating one (the Tolman VII analytical solution cannot describe all of them, as displayed in Figure 5.11), and (b) it can also describe the maximally-rotating configuration.

Figure 5.11 presents the results of the 23 hadronic EoSs, for the non-rotating and maximally-rotating case, Cook's (Cook et al., 1994a) and Salgado's (Salgado et al., 1994a) data, Tolman VII analytical solution and the proposed solution (5.20). The observed neutron star mass limits are also presented to guide the eye.

The knowledge of the central density at the maximally-rotating case is important for studying the pulsar's time evolution. In particular, following the spin-down trail of a millisecond pulsar, the central density increases and the highly compressible quark matter will replace the existed nuclear matter. This effect is directly connected to the reduction of moment of inertia. Henceforth, the central density can inform us on the appearance of a phase transition in its interior. The latter can leads to the important back-bending phenomenon in pulsars (Glendenning, 1998).

Another interesting effect that presented via the Figure 5.11, is the connection that establishes between gravitational mass at the maximum mass configuration and the corresponding central

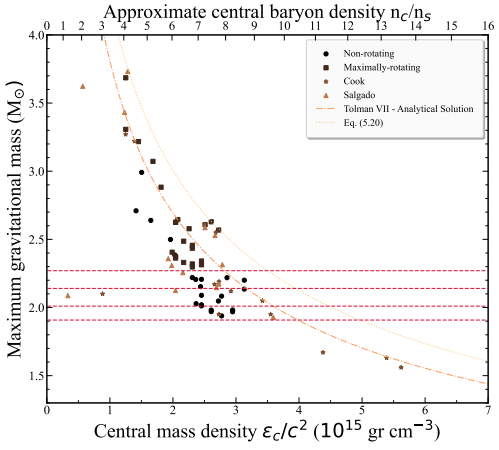

Figure 5.11: Gravitational mass dependence on the central energy density and the central baryon density at the maximum mass configuration for the 23 EoSs at the non-rotating and maximally-rotating case. Circles correspond to the non-rotating case, squares to the maximally-rotating one, stars to Cook's (Cook et al., 1994a) data and triangles to Salgado's (Salgado et al., 1994a) data. The horizontal dashed lines correspond to the observed neutron star mass limits ($1.908M_{\odot}$, $2.01M_{\odot}$, $2.14M_{\odot}$ and $2.27M_{\odot}$). For comparison, the Tolman-VII analytical solution with the dashed-dotted curve and the Equation (5.20) with the dotted one are shown.

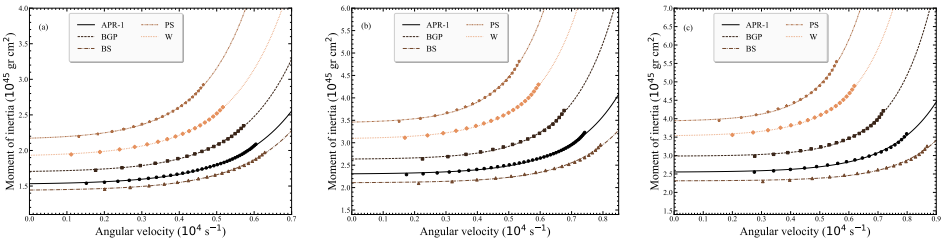

Figure 5.12: Constant rest mass sequences as the dependence of moment of inertia on the angular velocity for five representative EoSs and with rest mass corresponding to (a) $M^{\rm gr}_{\rm max} = 1.45M_\odot$, (b) $M^{\rm gr}_{\rm max} = 2M_\odot$, and (c) $M^{\rm gr}_{\rm max} = 2.2M_\odot$. The data and fits for each EoS are presented with the circles and the solid curve for the APR-1, the squares and the dashed curve for the BGP, the triangles and the dashed-dotted curve for the BS, the stars and the dashed-dotted-dotted curve for the PS and the diamonds and the dotted curve for W.

energy density. Besides the fact that can provide the absolute upper limit in density inside any compact star, it can also directly connect the macroscopic properties of neutron star with the microscopic ones.

5.7 Braking index

It is well-known that the angular velocity Ω of an isolated pulsar decreases very slowly with the time. Various energy loss mechanisms are responsible for this effect, including mainly dipole radiation, charged particles ejections and gravitational waves radiation (edited by W. Becker, 2009; Glendenning, 2000; Hamil et al., 2015; Lorimer and Kramer, 2005; Lorimer, 2008; Lyne et al., 2014; Manchester et al., 2005; Weber, 1999). In this case, and in the most simple model, the evolution of the angular velocity is given by the power law

$$\dot{\Omega} \equiv \frac{d\Omega}{dt} = -\mathcal{J}\Omega^n. \tag{5.21}$$

The braking index, n, of a pulsar, which describes the dependence of the braking torque on the rotation frequency, is a fundamental parameter of pulsar electrodynamics. Simple theoretical arguments, based on the assumption of a constant dipolar magnetic field, predict $n = 3$. It is easy to show that Equation (5.21) leads to the fundamental relation

$$n(\Omega) = \frac{\Omega\ddot{\Omega}}{\dot{\Omega}^2} = 3 - \frac{3\Omega I' + \Omega^2 I''}{2I + \Omega I'}, \tag{5.22}$$

where dot corresponds to the derivative with time, $I' = dI/d\Omega$ and $I'' = d^2I/d\Omega^2$. Now, considering the simple power law dependence $I \sim \Omega^\lambda$, the braking index takes the simple and transparent value

$$n(\Omega) = 3 - \lambda. \tag{5.23}$$

While for $\lambda = 0$ (moment of inertia independent from angular velocity) the well-known result $n = 3$ is recovered, in general it is expected that the inequality $n(\Omega) \leq 3$ must hold. There is a special case where for some reasons when the denominator of Equation (5.22) goes to zero, then the braking index exhibits a singularity which leads to increasing of Ω with time (Bagchi et al., 2015; Glendenning, 2000; Glendenning et al., 1997; Heiselberg and Hjorth-Jensen, 1998; Weber, 1996; Zdunik et al., 2006). This is an interesting effect (which may be caused due to a phase transition in the interior of a pulsar) but it would not be studied further in this work.

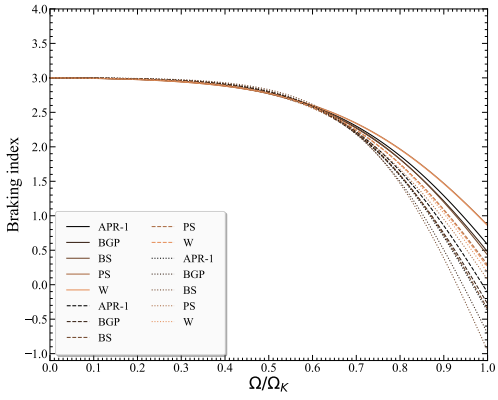

Figure 5.13: Braking index dependence on the angular velocity for the five representative EoSs (APR-1, BGP, BS, PS and W) with constant rest masses. The solid curves correspond to the $M^{\rm gr}_{\rm max} = 1.45 M_\odot$, the dashed curves to the $M^{\rm gr}_{\rm max} = 2 M_\odot$ and the dotted curves to the $M^{\rm gr}_{\rm max} = 2.2 M_\odot$.

Instead, the effects of the EoS on the braking index as well as on the evolution of the angular velocity of a pulsar, especially for very young, at their birth, with their angular velocity being at the mass-shedding limit, have been studied.

In particular, the moment of inertia dependence on the angular velocity for five representative EoSs and for three different values of rest mass, has been studied. In each case, a fit is produced, as shown in Figure 5.12, according to the formula

$$I = \mathrm{g}_1 + \mathrm{g}_2 \exp\left[\mathrm{g}_3 \Omega\right], \tag{5.24}$$

where g_1, g_2 are in units of moment of inertia $(10^{45}\mathrm{gr\ cm}^2)$ and g_3 in units of time (s).

In order to see how the rest mass effects the braking index, Figure 5.13 presents the five representative EoSs for the different rest masses.

From Figure 5.13, it is clear that the rest mass plays an important role on the braking index, i.e. by increasing the rest mass value, the braking index decreases more sharply. This effect will remain valid for all EoSs studied in this research.

CHAPTER 6

Neutron stars stability in terms of adiabatic indices

6.1 The adiabatic indices and the stability criterion

The starting point for determining the mechanical equilibrium of neutron star matter is the well known TOV equations (Glendenning, 2000; Oppenheimer and Volkoff, 1939; Shapiro and Teukolsky, 1983; Tolman, 1939). This set of differential equations describes the structure of a neutron star. For a static spherical symmetric system, the metric reads as follows (Glendenning, 2000; Shapiro and Teukolsky, 1983):

$$ds^2 = -e^{\nu(r)}c^2dt^2 + e^{\lambda(r)}dr^2 + r^2\left(d\theta^2 + \sin^2\theta d\phi^2\right), \tag{6.1}$$

and the corresponding TOV equations take the form

$$\frac{dP(r)}{dr} = -\frac{G\mathcal{E}(r)M(r)}{c^2r^2}\left(1+\frac{P(r)}{\mathcal{E}(r)}\right)\left(1+\frac{4\pi P(r)r^3}{M(r)c^2}\right)\left(1-\frac{2GM(r)}{c^2r}\right)^{-1}, \tag{6.2}$$

$$\frac{dM(r)}{dr} = \frac{4\pi r^2}{c^2}\mathcal{E}(r). \tag{6.3}$$

By introducing a realistic EoS for the neutron star (e.g., a dependence on the form $P = P(\mathcal{E})$), the TOV equations can be solved numerically. This EoS provides the relation between the pressure and density of neutron star matter. Of course, one can try to find analytical solutions for the TOV equations. However, it is worth pointing out that using the analytical solutions, although each one describes equilibrium configurations, is insufficient to tell us if it corresponds to stable ones (Tolman, 1939); this is the case also for any numerical solution. Straightforwardly speaking, any unstable solution is not of physical interest.

Chandrasekhar, in order to solve the instability problem, introduced a criterion for dynamical stability based on the variational method (Chandrasekhar, 1964a). In the present study, this criterion will be presented with the help of the averaged ($\langle\gamma\rangle$) and the critical (γ_{cr}) adiabatic indices. To be more specific, the averaged adiabatic index is defined as follows (Merafina and Ruffini, 1989; Moustakidis, 2017; Negi and Durgapal, 2001):

$$\langle\gamma\rangle = \frac{\displaystyle\int_0^R e^{(\lambda+3\nu)/2}\gamma(r)\frac{P}{r^2}\left(\frac{d}{dr}(r^2e^{-\nu/2}\xi(r))\right)^2 dr}{\displaystyle\int_0^R e^{(\lambda+3\nu)/2}\frac{P}{r^2}\left(\frac{d}{dr}(r^2e^{-\nu/2}\xi(r))\right)^2 dr}, \tag{6.4}$$

and the effective critical adiabatic index as

$$\begin{aligned}\gamma_{cr} &= \left[-4\int_0^R e^{(\lambda+\nu)/2} r\left(\frac{dP}{dr}\right)\xi^2 dr + \int_0^R e^{(\lambda+\nu)/2}\left(\frac{dP}{dr}\right)^2 \frac{r^2\xi^2}{P+\mathcal{E}} dr\right. \\ &- \left.\frac{8\pi G}{c^4}\int_0^R e^{(3\lambda+\nu)/2} P(P+\mathcal{E}) r^2\xi^2 dr\right] \\ &\times \left(\int_0^R e^{(\lambda+3\nu)/2}\frac{P}{r^2}\left(\frac{d}{dr}(r^2 e^{-\nu/2}\xi)\right)^2 dr\right)^{-1}. \end{aligned} \tag{6.5}$$

The Chandrasekhar stability condition leads to the inequality

$$\langle\gamma\rangle \geq \gamma_{cr}, \tag{6.6}$$

while the case $\langle\gamma\rangle = \gamma_{cr}$ corresponds to the onset of the instability (Merafina and Ruffini, 1989; Moustakidis, 2017). According to Equations (6.4) and (6.5), the averaged and the critical adiabatic indices are functions of the function $\xi(r)$ as well as of the compactness parameter β. In particular, the lagrangian displacement away from equilibrium has the form $\zeta(r) = \xi(r)e^{-i\sigma t}$, where σ is the pulsation frequency of the oscillations. It is obvious from the lagrangian displacement that σ^2 can take both positive and negative values. More specifically, a positive value of σ^2 corresponds to stable configuration while a negative to unstable one (Chandrasekhar, 1964a; Kokkotas and Ruoff, 2001; Merafina and Ruffini, 1989). It is worth pointing out that the stability condition (6.6) expresses a minimal and not just an external principle (Chandrasekhar, 1964a).

6.2 Trial functions

Moving on to the trial functions that appear in Equations (6.4) and (6.5), it is widely known that there are infinite numbers of them. However, the most frequently used are the following:

$$\xi(r) = re^{\nu/2}, \quad (\text{TF}-1) \tag{6.7}$$
$$\xi(r) = re^{\nu/4}, \quad (\text{TF}-2) \tag{6.8}$$
$$\xi(r) = r\left(1+a_1r^2+a_2r^4+a_3r^6\right)e^{\nu/2}, \quad (\text{TF}-3) \tag{6.9}$$
$$\xi(r) = r. \quad (\text{TF}-4) \tag{6.10}$$

Considering an adiabatic perturbation, the adiabatic index γ is defined as follows (Chandrasekhar, 1964a; Merafina and Ruffini, 1989):

$$\gamma \equiv \frac{P+\mathcal{E}}{P}\left(\frac{\partial P}{\partial \mathcal{E}}\right)_S = \left(1+\frac{\mathcal{E}}{P}\right)\left(\frac{v_s}{c}\right)_S^2, \tag{6.11}$$

where derivation is performed at constant entropy S. Moreover, $(v_s/c)_S = \sqrt{(\partial P/\partial\mathcal{E})_S}$ is the speed of sound in units of speed of light. The speed of sound is an important quantity directly related to the stiffness of the EoS and plays a significant role in the maximum mass configurations. Since the adiabatic index is a function of the baryon density, it exhibits radial dependence and provides local information for each neutron star configuration. Its values vary from 2 to 4 in most neutron stars EoSs (Haensel et al., 2007). The adiabatic index is a constant in the specific case of a polytropic EoS. The effective adiabatic indices, $\langle\gamma\rangle$ and γ_{cr}, in contrast to γ (Equation (6.11)) have a global character. Both are directly related to the neutron star EoS and the strength of the gravitational field (see also Refs. (Bludman, 1973a,b; Chan et al., 1994; Herrera et al., 1989; Ipser, 1970; Merafina and Ruffini, 1989; Moustakidis, 2017; Negi and Durgapal, 2001, 1999; Sharif and Yousaf, 2015; Yousaf and Bhatti, 2016)).

6.3 Analytical solutions and polytropic equations of state

Chandrasekhar, using the Schwarzschild constant-density interior solution, found that in the Newtonian limit, the stability ensured when (Chandrasekhar, 1964a):

$$\langle\gamma\rangle \geq \gamma_{cr} = \frac{4}{3} + \frac{19}{42}2\beta. \tag{6.12}$$

He employed the approximation that the adiabatic index γ is a constant throughout the star (Chandrasekhar, 1964a). In particular, this approximation directly relates the EoS, which characterizes the fluid, to a possible stable configuration. In addition, Chandrasekhar (Chandrasekhar, 1964a), in the framework of the post-Newtonian approximation, using relativistic polytropes found the relation

$$\gamma_{\rm cr} = \frac{4}{3} + C\left(\frac{P_c}{\mathcal{E}_c}\right), \tag{6.13}$$

where $C = 1.8095, 2.2615, 2.4968, 2.6325$ corresponds to the polytropic index $n = 0, 1, 2, 3$, respectively, and P_c, $\mathcal{E}_c$ are the central values of pressure and energy density. It should be noted that the ratio $P_c/\mathcal{E}_c$ can also be mentioned as a relativistic index and closely related to the compactness β. Similar results have also been found by Tooper in a series of papers (Tooper, 1964, 1965). Moreover, Bludman (Bludman, 1973a,b) studied the stability of general relativistic polytropes and provided the formula

$$\gamma_{\rm cr} \simeq \frac{4}{3} + 1.73\left(\frac{P_c}{\mathcal{E}_c}\right) - 0.31\left(\frac{P_c}{\mathcal{E}_c}\right)^2. \tag{6.14}$$

It is worth extending all these previous studies in order to examine the dependence of $\gamma_{\rm cr}$ on the compactness parameter $\beta_{\rm max}$ (as well as on the ratio $P_c/\mathcal{E}_c$) close to the instability limit, which corresponds to the maximum mass configuration. Although the study concerning the Newtonian or post-Newtonian case is universal, meaning that for low values of β ($\beta \ll 1$), the dependence of $\gamma_{\rm cr}$ is almost insensitive to the details of the EoS, this is not the case for high values of β. In this case, the structure of a neutron star and the corresponding values of $\gamma_{\rm cr}$ are susceptible to the EoS. Since, especially for high values of densities, the uncertainty on pressure-energy dependence is appreciable, an influence on the values of $\gamma_{\rm cr}$ is expected. In view of the above, it is concluded that possible constraints on $\beta_{\rm max}$ may impose constraints on the high-density behavior of the neutron star EoSs.

The stability of the equilibrium configuration by using the general properties of the central density as well as those of the mass-radius relation (Weinberg, 1972) is also possible. In this case, the configuration is stable when the inequality $dM/d\mathcal{E}_c > 0$ holds. Actually, this condition, due to its simplicity, has been used extensively in the literature. However, it needs to be noted that this condition is just necessary but not sufficient, and consequently, it is weak compared to the criterion (6.6).

A brief discussion is presented considering the four analytical solutions of the TOV equations. In the case of the Schwarzschild constant-density interior solution (hereafter Uniform), the density is constant throughout the star (Schutz, 1985; Weinberg, 1972). Although this solution is far from being realistic, it has been applied extensively in the literature due to its simplicity.

The Tolman VII solution has been extensively employed in neutron star studies. Actually, its physical realization has been studied in detail in Ref. (Raghoonundun and Hobill, 2015). This solution ensures the causality for $\beta < 0.2698$. However, useful information and predictions are taken when applied for even higher values of β (see, for example, Refs. (Lattimer and Prakash, 2001, 2005; Moustakidis, 2017; Sotani and Kokkotas, 2018)).

Buchdahl's solution (Buchdahl, 1959a,b) is applicable only for low values of the compactness ($\beta \leq 0.2$) since for higher values, the speed of sound becomes infinite. However, its use helps

to support the rest solutions' findings even for low compactness values e.g., it forms a *bridge* which connects the Newtonian and post-Newtonian limit with the relativistic one (Lattimer and Prakash, 2001; Moustakidis, 2017; Papazoglou and Moustakidis, 2016).

The Nariai IV solution (Nariai, 1950, 1951, 1999), although is very complicated, it provides useful insights because it is one of the physically interesting solutions. In this case, the energy density and pressure are complicated functions of the parametric variable r', which is related to the distance r (for the definitions of the involved functions and constants and more details, see Ref. (Moustakidis, 2017)).

All these solutions have the required property that the derived density and pressure vanish at the star's surface (except for the Schwarzschild constant-density interior solution). Generally, the selected solutions exhibit realistic behavior and can be used as a guide to establishing universal approximations. In particular, while the unrealistic Uniform solution has been used by Chandrasekhar (Chandrasekhar, 1964a) in order to prove his famous expression (6.12), its main drawback is the infinite value of the speed of sound. In Tolman VII solution's case, the causality was ensured for $\beta < 0.2698$. However, useful information and predictions are taken when applied even for higher values of β. Thus, Lattimer and Prakash (Lattimer and Prakash, 2005) have demonstrated, using the Tolman VII solution, that the largest measured mass of a neutron star establishes an upper bound to the energy density of observable cold matter. Moreover, while in the Nariai IV solution, the causality was ensured for $\beta < 0.2277$, its extension for higher values was applied successfully (Lattimer and Prakash, 2005; Moustakidis, 2017; Papazoglou and Moustakidis, 2016).

6.4 Maximum mass and maximum rotation frequency

It is known that rotation increases the maximum mass ($M_{\rm max}^{\rm stat}$) of a corresponding stationary neutron star. In this case, we face two extreme configurations: (a) maximum mass $M_{\rm max}^{\rm rot}$ and (b) maximum rotation frequency $f_{\rm max}$ (known as Kepler frequency) (Haensel et al., 2007). These configurations do not coincide, but we do not differentiate them since they are very close to each other (with high accuracy). Moreover, it was found that the maximum frequency can be expressed, with high precision, in terms of mass and radius of the non-rotating configuration with the maximum mass (see Ref. (Haensel et al., 2007) and references therein). A precise formula that relates $M_{\rm max}^{\rm stat}$ to the maximum mass and the compactness parameter $\beta_{\rm max}^{\rm stat}$ of the static maximum mass configuration, is found by Haensel et al. (Haensel et al., 1999; Haensel et al., 2016; Lasota et al., 1996)

$$f_{\rm max} \simeq 15.125\, \beta_{\rm max}^{3/2}(1 + 1.6164\beta_{\rm max}) \left(\frac{M_\odot}{M_{\rm max}^{\rm stat}}\right) \ ({\rm kHz}). \tag{6.15}$$

It is worth pointing out the strong dependence of $f_{\rm max}$ on $\beta_{\rm max}^{\rm stat}$ and, consequently, via the adiabatic index, on the high-density dependence area of the EoS. The above expression can be used to constrain an absolute lower bound of the maximum frequency of rigid rotation (for example, by measuring the upper bound on the surface red-shift of a non-rotating neutron star) and, consequently, to impose valuable constraints on the EoS and vise-versa.

6.5 The effect of critical and average adiabatic indices

A large number of published realistic EoSs for neutron star matter based on various theoretical nuclear models are employed. A calculation of the effective averaged and the critical adiabatic indices for each configuration is performed, in addition to the adiabatic indices corresponding to the maximum mass configuration. The calculation recipe is the following: Firstly, the TOV equations are solved to determine the M-R dependence and the corresponding energy density and

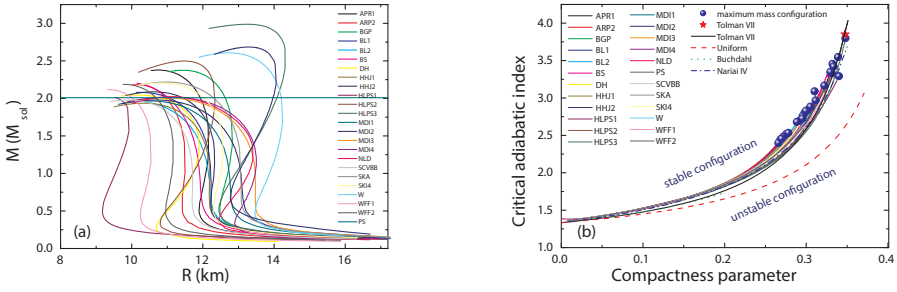

Figure 6.1: (a) Mass–radius trajectories for the selected EoSs. (b) The critical adiabatic index, $\gamma_{\rm cr}$, as a function of the compactness parameter β, for the selected EoSs (using the trial function TF-1 (6.7)). The results of the four analytical solutions, using for consistency the trial function TF-1 (6.7), have also been included for comparison (for more details see text). The blue dots correspond to the onset of instability as a result of the equality $\langle\gamma\rangle = \gamma_{\rm cr}$. The onset of instability for the Tolman VII solution is indicated by a red star (for the TF-1).

pressure configurations. Mainly, the interest is focused on the maximum mass, the corresponding radius, the ratio $P_c/\mathcal{E}_c$, and the corresponding compactness β for each case. Secondly, the determination of $\langle\gamma\rangle$ and $\gamma_{\rm cr}$ is performed for each configuration. The onset of instability is found from the equality $\langle\gamma\rangle = \gamma_{\rm cr}$. The corresponding compactness parameter denotes $\beta_{\rm max}$.

A second criterion also defines the stability limit according to the equality $dM/d\mathcal{E}_c = 0$, providing an additional value of β for the maximum mass configuration. Now, in general, since $\langle\gamma\rangle$ and $\gamma_{\rm cr}$ are functionals of the trial function $\xi(r)$, it is expected that the calculated values of β, for the two methods, will not coincide. In these cases, it will be considered as the most optimum trial function $\xi(r)$, the one that produces values of β, as close as possible to the second method. In particular, it has been found that the trial function (6.7) (indicated as TF-1) is the optimal one, leading to an error, in most cases, less than 1%.

Figure 6.1(a) shows the radius-mass relation using the selected EoSs. One can see that the majority of the EoSs reproduce the recent observation of two-solar mass neutron stars. The various predictions cover a wide range of the maximum neutron star masses and the corresponding radii.

Figure 6.1(b) displays the dependence of $\gamma_{\rm cr}$ as a function of the compactness parameter β for all the employed EoSs by using the optimal trial function (6.7). In particular, for the trial function (6.9) the parametrization $a_1 = 1/10R^2$, $a_2 = 1/5R^4$ and $a_3 = 3/10R^6$ has been used. The results of the four analytical solutions have also been included for comparison. The blue dots correspond to all configurations with neutrally stable equilibrium as result of the equality $\langle\gamma\rangle = \gamma_{\rm cr}$. These configurations correspond to the one with the largest possible central density reachable for stable mass configuration. In the case of the Tolman VII solution, the results using the trial function TF-1 (6.7) have also been included. In this case, the red star indicates the onset of instability and corresponds to $\beta = 0.3475$ and $\gamma_{\rm cr} = 3.85$. Remarkably, using the Tolman VII solution leads to results very close to the predictions using realistic EoSs. The other two analytical solutions (Buchdahl's and Nariai IV) lead to a stable configuration in each case (Moustakidis, 2017). The Uniform solution is always used as a guide for stable configuration, mainly for low values of the compactness β (see expression (6.12)).

The most distinctive feature in Figure 6.1(b) is the remarkable unanimity of all EoSs and consequently the occurrence of a model-independent relation between $\gamma_{\rm cr}$ and $\beta_{\rm max}$, at least for any stable configuration. The above finding is expected for low compactness values β (since all EoSs converge for low-density values). However, this result was not apparent at high densities

Table 6.1: The parametrization of the analytical formulae (6.16), (6.17) and (6.18) is using realistic EoSs as well as four analytical solutions (using the trial function TF-1 (6.7)). The case mentioned as *Realistic EoS*, reproduces the averaged results of the realistic equations of state.

Solution	y_0	A_1	t_1	A_2	t_2	γ_0	C_1	C_2
Realistic EoS	1.23333	0.10425	0.11007					
Tolman VII	1.18654	0.14938	0.15293	0.00011	0.03731	1.32055	2.45877	-0.36691
Buchdahl	1.04258	0.28285	0.27558	0.00792	0.07695	1.33344	2.25592	-1.28137
Nariai IV	1.13470	0.20200	0.16781	0.00015	0.04016	1.33094	2.68839	-0.45055
Uniform	1.18955	0.14587	0.17682	0.00009	0.04140	1.32743	1.94115	-0.08660

of the EoSs, where there is considerable uncertainty. In any case, as a consequence of the convergence, most of the points indicate the onset of the instability, located in the mentioned trajectory for low and high compactness values. In particular, it has been found that the simple expression

$$\gamma_{\rm cr}(\beta) = y_0 + A_1 e^{\beta/t_1}, \tag{6.16}$$

reproduces very well the numerical results due to the use of realistic EoSs. Equation (6.16) is the relativistic expression for the critical value of the adiabatic index and can be considered as the relativistic generalization of the post-Newtonian approximation (6.12). The parametrization is provided in Table 6.1.

The results of the analytical solutions, in each case, can be parameterized according to the expression (see details in Table 6.1)

$$\gamma_{\rm cr}(\beta) = y_0 + A_1 e^{\beta/t_1} + A_2 e^{\beta/t_2}. \tag{6.17}$$

There is a slight deviation between the results of the realistic EoSs and the analytical solutions Tolman VII, Nariai IV, and Buchdahl. It is worth noticing that the Tolman VII solution reproduces the numerical results very well, especially for high compactness values. The analytical solutions generally lead to lower values of the adiabatic index $\gamma_{\rm cr}$, compared to the realistic EoS. In particular, the Uniform solution provides the lower limit for $\gamma_{\rm cr}$, especially for high compactness values and close to the instability limit. However, the general trend is similar and useful insight can be gained concerning the reliability of analytical solutions. The stable configurations, independently of the EoS, correspond to a universal relation between $\gamma_{\rm cr}$ and β. One can safely conclude that $\gamma_{\rm cr}$ is an intrinsic property of neutron stars (likewise the parameter β), which reflects the relativistic effects on their structure. In particular, $\gamma_{\rm cr}$ exhibits a linear dependence with β in the Newtonian and post-Newtonian regimes but a more complicated behavior in the relativistic regime.

The above finding may help impose constraints on the EoS of neutron star matter. For example, the accurate and simultaneous observation of possible maximum neutron star mass and the corresponding radius will constrain the maximum values of the compactness and, consequently, the maximum value of the adiabatic index $\gamma_{\rm cr}$. In any case, useful insights may be gained by the use of the expression (6.16) with the parametrization given in Table 6.1 (Realistic EoS).

In order to clarify further the effects of the trial functions $\xi(r)$ on the results, Figure 6.2(a) is presented. In particular, Figure 6.2(a) displays the dependence of the critical adiabatic index, $\gamma_{\rm cr}$, which corresponds to the onset of instability ($\gamma_{\rm cr}$=$\langle\gamma\rangle$ at this point), as a function of the compactness parameter $\beta_{\rm max}$ using the selected trial functions (6.7), (6.8), (6.9) and (6.10). The most distinctive feature, in this case, is the occurrence of almost linear dependence (in the region under study, e.g., on the maximum mass configuration) between the adiabatic index and the compactness $\beta_{\rm max}$. The use of the trial function $\xi(r)$ affects mainly the values of $\gamma_{\rm cr}$ (for the same $\beta_{\rm max}$) but not the linear dependence.

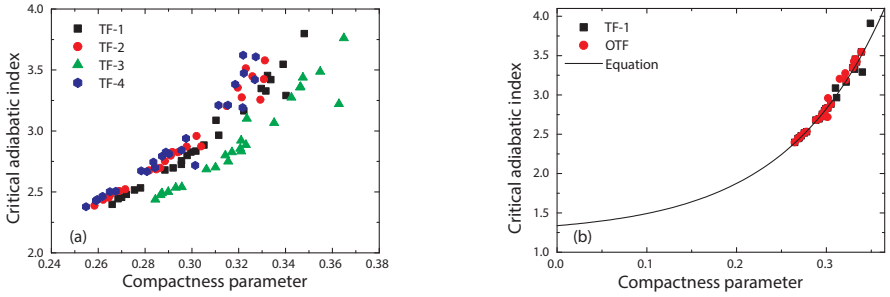

Figure 6.2: (a) The critical adiabatic index $\gamma_{\rm cr}$ as a function of the compactness parameter β for the selected EoSs. The points correspond to the onset of instability for the four selected trial functions $\xi(r)$. (b) The critical adiabatic index, $\gamma_{\rm cr}$, as a function of the compactness parameter β, for the selected EoSs, using the trial function TF-1 (6.7) (squares) and the optimal trial function (OTF) in each EoS (dots). The expression (6.16) (the parametrization is provided in Table 6.1) which reproduces the numerical results corresponding to the trial function (6.7) is also included.

Moreover, in Figure 6.2(b) it is displayed the $\gamma_{\rm cr}$, as a function of the compactness parameter β, for the selected EoSs, using the trial function TF-1 (6.7) and the optimal trial function (OTF) in each EoS, which corresponds to the one with the smallest error. The expression (6.16), which reproduces the numerical results corresponding to the trial function (6.7), is also included. Using the optimal trial function in each EoS the rearrangement of the results becomes more ordered. However, the deviation from using the trial function TF-1 (which is the optimal one in most cases) is negligible.

In Figure 6.3(a) it is displayed the dependence of $\gamma_{\rm cr}$ on the ratio $P_c/\mathcal{E}_c$ (which corresponds to the maximum mass configuration). The symbols correspond to the results originating from the use of realistic EoSs, while the results of the four analytical solutions have also been included for comparison. Generally, in the case of realistic EoS, $\gamma_{\rm cr}$ is an increasing function of the ratio $P_c/\mathcal{E}_c$ without obeying in a specific formula. However, it has been found that the expression

$$\gamma_{\rm cr} = \gamma_0 + C_1 \left(\frac{P_c}{\mathcal{E}_c}\right) + C_2 \left(\frac{P_c}{\mathcal{E}_c}\right)^2, \tag{6.18}$$

reproduces very well the numerical results of the analytical solutions. The parameters γ_0, C_1, C_2 are displayed in Table 6.1. In Figure 6.3(b) displayed the dependence of $\gamma_{\rm cr}$ on $M_{\rm max}$. In Figure 6.3(c) is plotted the $\gamma_{\rm cr}$ as a function of the radius corresponding to the maximum mass configuration, $R_{\rm max}$. In these cases, the dependence is almost random and, consequently, is unlikely to impose constraints from these correlations.

It is known that for low values of β (in the framework of Newtonian and post-Newtonian approximation), there is a straightforward and universal linear correlation between β and the ratio $P_c/\mathcal{E}_c$. In particular, in the case of the analytical solutions of the TOV equations (Uniform, Tolman VII, Buchdahl's, and Nariai IV), we get in each case, by employing a Taylor expansion, the approximated simple relation

$$\frac{P_c}{\mathcal{E}_c} \simeq \frac{\beta}{2}. \tag{6.19}$$

Moreover, in the case of the Newtonian limit, e.g., using the Lane-Emden equation with the polytropic EoS, $P = K(\mathcal{E}/c^2)^{\Gamma} = K(\mathcal{E}/c^2)^{1+\frac{1}{n}}$, that is

$$\frac{1}{\xi^2}\frac{d}{d\xi}\xi^2\frac{d\theta}{d\xi} = -\theta^n, \tag{6.20}$$

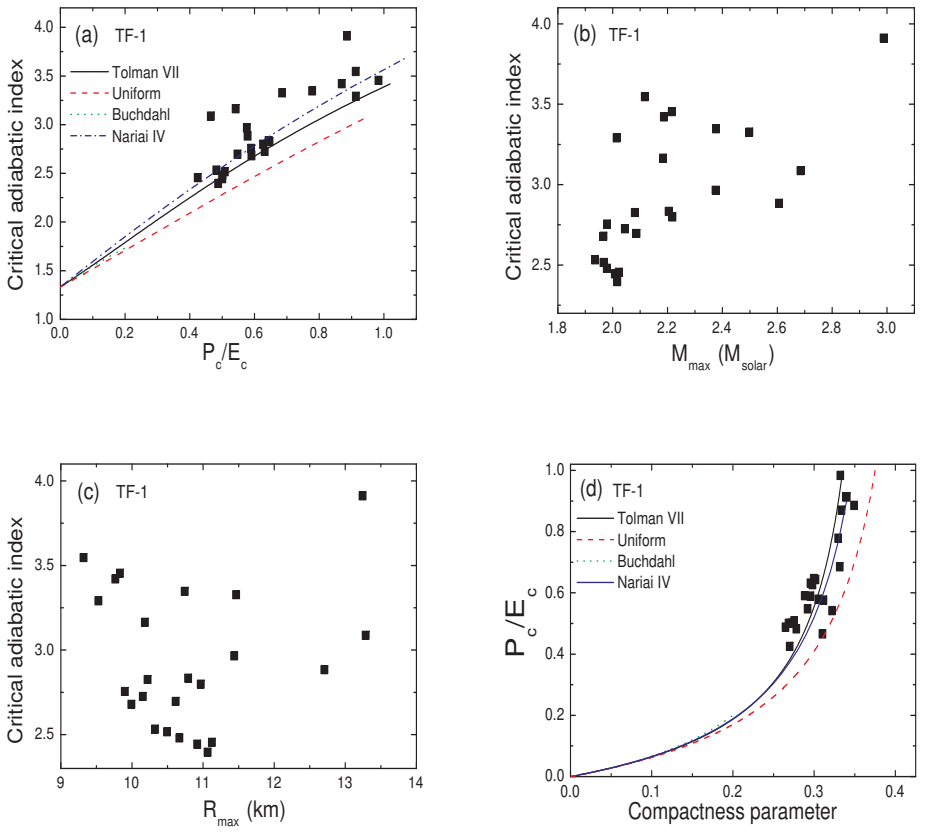

Figure 6.3: (a) The critical adiabatic index, $\gamma_{\rm cr}$, as a function of the ratio $P_c/\mathcal{E}_c$ for the selected EoSs (the dots correspond to the onset of instability in each case) and for the trial function TF-1 (6.7). The results of the four analytical solutions have also been included for comparison. (b) The $\gamma_{\rm cr}$ as a function of the maximum mass, $M_{\rm max}$, for the selected EoSs, (c) the $\gamma_{\rm cr}$ as a function of the radius, $R_{\rm max}$, corresponding to $M_{\rm max}$ for the selected EoSs, and (d) the ratio $P_c/\mathcal{E}_c$ as a function of the compactness parameter, β, for the selected EoSs while the results of the four analytical solutions have also been included for comparison.

with $\theta(\xi_0) = 0$, we get for the total mass and radius (Shapiro and Teukolsky, 1983)

$$M = 4\pi \left[\frac{(n+1)K}{4\pi G}\right]^{3/2} \left(\frac{\mathcal{E}_c}{c}\right)^{(3-n)/2n} \xi_0^2 |\theta'(\xi_0)|, \tag{6.21}$$

and

$$R = \left[\frac{(n+1)K}{4\pi G}\right]^{1/2} \left(\frac{\mathcal{E}_c}{c}\right)^{(1-n)/2n} \xi_0. \tag{6.22}$$

Combining Equations (6.21) and (6.22) it has been found

$$\frac{P_c}{\mathcal{E}_c} = \frac{\beta}{2}\left(\frac{n+1}{2}\xi_0|\theta'(\xi_0)|\right)^{-1}, \tag{6.23}$$

or in general,

$$\frac{P_c}{\mathcal{E}_c} = \frac{\beta}{2}\mathcal{F}(\xi_0, n), \tag{6.24}$$

where $\mathcal{F}(\xi_0, n)$ is a function of ξ_0 and the polytropic index n. More precisely, it has been found that for $n = 0, 0.5, 1, 1.5, 2, 3, 4$ (correspondingly $\Gamma = \infty, 3, 2, 5/3, 3/2, 4/3, 5/4$) the respectively function is $\mathcal{F}(\xi_0, n) = 1$, 0.97, 1, 1.077, 1.204, 1.709, 3.332. Concluding, for $0 < n < 2$, the $\mathcal{F}(\xi_0, n) \simeq 1$.

Since it is worth examining this dependence in the relativistic limit, Figure 6.3(d) displays the dependence of $P_c/\mathcal{E}_c$ on the compactness $\beta_{\max}$. Firstly, the symbols originated from using realistic EoSs obey a general trend. A similar trend is obtained by employing analytical solutions. In particular, the Tolman VII and Nariai IV solutions reproduce the results of realistic calculations very well. Consequently, the Tolman VII solution may be used as a guide for an almost universal dependence between $P_c/\mathcal{E}_c$ and $\beta_{\max}$ that is in the critical point between stable and unstable configuration. Moreover, this correlation may help to constrain the maximum value of the ratio $P_c/\mathcal{E}_c$ and, consequently, the maximum density in the universe with the help of accurate measurements of the maximum value of the compactness.

More specifically, from recent observations of the GW170917 binary system merger, Bauswein et al. (Bauswein et al., 2017) propose a method to constrain some neutron star properties. In particular, they found that the radius $R_{\max}$ of the non-rotating maximum-mass configuration must

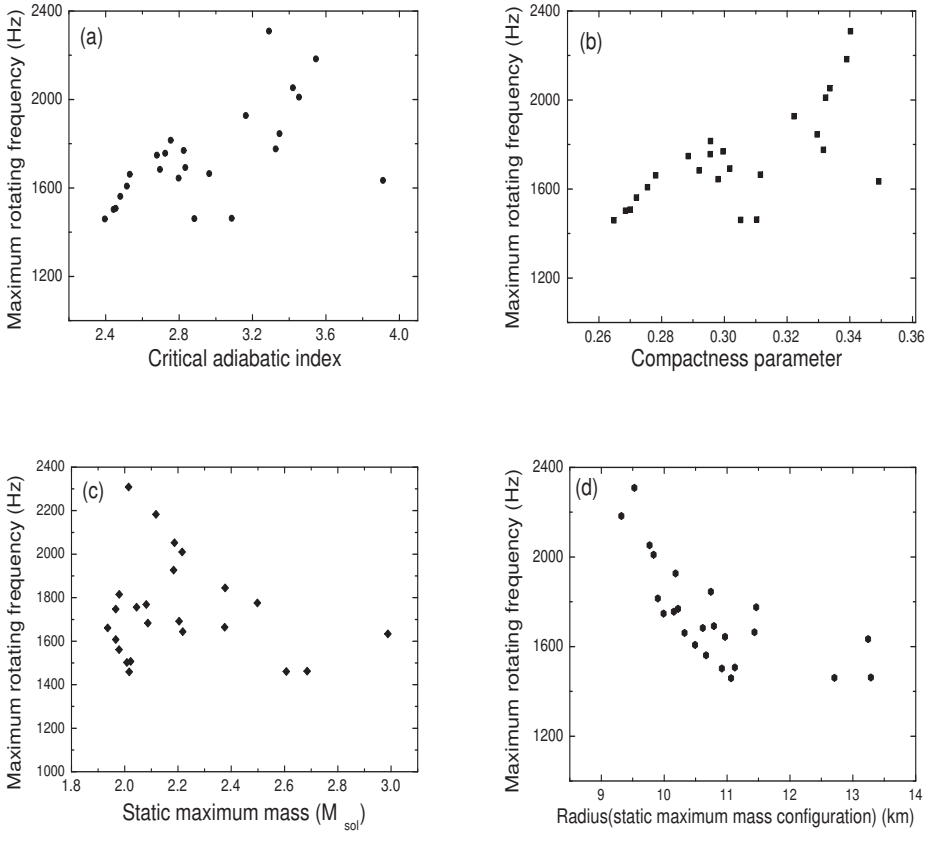

Figure 6.4: The maximum rotating frequency $f_{\max}$ for the selected EoSs, as a function: (a) of the critical adiabatic index, $\gamma_{\rm cr}$, (b) of the compactness parameter $\beta^{\rm stat}_{\max}$ which corresponds to the static maximum mass configuration, (c) of the static maximum mass $M^{\rm stat}_{\max}$ and (d) of the radius $R^{\rm stat}_{\max}$ which corresponds to the static maximum mass configuration.

be larger than $9.6^{+0.15}_{-0.04}$ km. Almost simultaneously, Margalit and Metzger (Margalit and Metzger, 2017) combining electromagnetic and gravitational-wave information on the binary neutron star merger GW170817, constrain the upper limit of $M_{\rm max}$ according to $M_{\rm max} \leq 2.17 M_{\odot}$. The combination of the two suggestions leads to an absolute maximum value of compactness, which is equal to $\beta_{\rm max} = 0.333^{+0.001}_{-0.005}$. The use of this value with the help of the Figure 6.1(b) and Figure 6.3(d) will impose constraints both on the maximum values of the index $\gamma_{\rm cr}$ and the ratio $P_c/\mathcal{E}_c$. According to expression (6.16), constraint on the $\gamma_{\rm cr}$ can be imposed, which is $\gamma_{\rm cr,max} = 3.381^{+0.020}_{-0.095}$, correspondingly to $\beta_{\rm max}$. Even more, a large number of realistic EoSs must be excluded. Some previous and recent efforts to constrain the compactness of neutron stars, have been provided in Refs. (Alsing et al., 2018; Chen and Piekarewicz, 2015; Hambaryan et al., 2017; Miller and Lamb, 1998; Ravenhall and Pethick, 1994; Rosso et al., 2017).

Figure 6.4(a) displays the dependence of the maximum rotating frequency on the critical adiabatic index (it is wort to indicate, in order to avoid any confusion, that in the present study $M^{\rm stat}_{\rm max}$, $R^{\rm stat}_{\rm max}$ and $\beta^{\rm stat}_{\rm max}$ correspond to $M_{\rm max}$, $R_{\rm max}$ and $\beta_{\rm max}$, respectively). While $f_{\rm max}$ is an increasing function of $\gamma_{\rm crit}$, the relative correlation is not so restrictive. However, the most important finding (see also the Figure 6.4(b)) is the derivation of an absolute lower upper bound of the maximum rotation rate close to the value 1460 Hz. The observation of neutron stars rotating with a spin $f > 1460$ Hz, will exclude a number of the selected EoSs. Figure 6.4(b) also presents the dependence of $f_{\rm max}$ on $\beta^{\rm stat}_{\rm max}$ while in Figure 6.4(c) the dependence of $f_{\rm max}$ on the mass which corresponds to the static maximum mass configuration is provided. In this case, the dependence is random. However, the dependence of $f_{\rm max}$ on the radius, shown in Figure 6.4(d), which corresponds to the static maximum mass configuration, exhibits a more restrictive dependence. In particular, $f_{\rm max}$ is a decreasing function of $R^{\rm stat}_{\rm max}$, i.e., the maximum rotation rate is expected to be observed in low-size neutron stars.

In any case, further theoretical and observational studies and refined combinations of them are necessary before accurate, reliable, and robust constraints can be inferred.

CHAPTER 7

Neutron stars with hot and lepton rich matter

7.1 Single particle potentials and effective mass

Among the important tasks of this research, prominent position has the reliability of the implemented nuclear model (MDI). As already mentioned, the MDI model reproduces accurately the bulk properties of SNM at low densities (including saturation density, energy per particle, incompresibility, etc.). This is important in order to ensure the credibility of the EoS at low densities, a region which mainly relates to the radius of the star and the crust-core transition densities. In addition, the predictions of PNM have been compared with those originated from the very recent *state-of-the-art* calculations (shaded region at Figure 4.2) (Piarulli et al., 2020) (see also the relevant discussion at Section 4.2).

In order to further check the EoS, in Figure 7.1 is displayed the single particle potential (SPP) of protons (neutrons) in SNM as a function of the momentum (Moustakidis, 2008). In particular, the SPP is plotted for three values of the baryon density. In each case the results of numerous models are also presented for comparison (Li and Machleidt, 1993; Wiringa, 1988). It is observed that, although at the saturation density the SPP exhibits lower values, for higher densities the results converge. Moreover, a mild dependence on the values of the momentum is also presented, which is expected to be reflected to the dependence of the EoS on temperature.

In addition, the nucleon effective mass has been calculated. This property of nuclear matter characterizes the momentum dependence of the SPP, as it provides useful information concerning

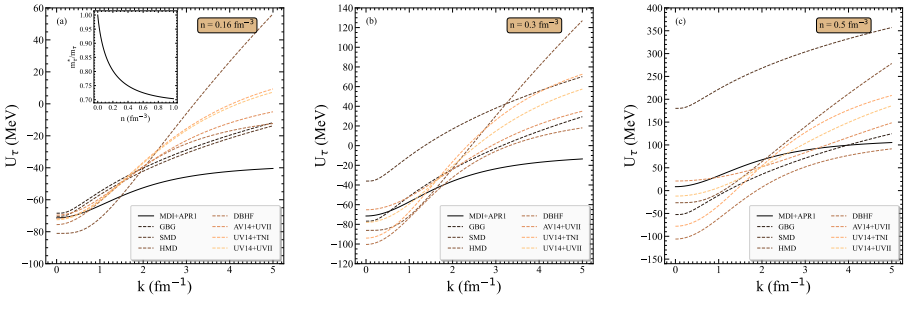

Figure 7.1: Single particle potential of protons (neutrons) as a function of momentum in symmetric nuclear matter for MDI+APR1 EoS (solid line) and baryon density (a) n=0.16 fm^{-3}, (b) n=0.3 fm^{-3}, and (c) n=0.5 fm^{-3}. The dashed lines correspond to various nuclear models for comparison from Refs. (Li and Machleidt, 1993; Wiringa, 1988). The inner figure presents the Landau effective mass as a function of baryon density for the MDI+APR1 EoS.

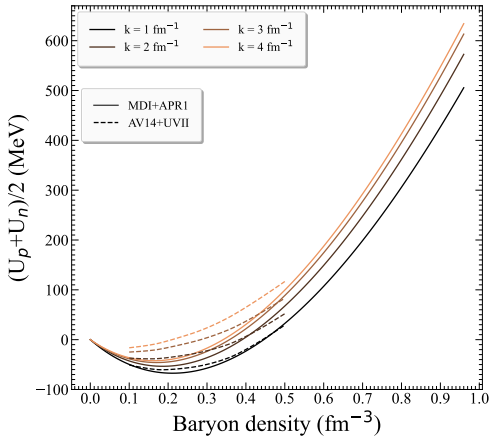

Figure 7.2: Isoscalar potential as a function of baryon density for the MDI+APR1 EoS (solid lines) and momentum in the range $[1-4]$ fm^{-1}. For comparison the data of A14+UVII model are also presented with dashed lines in the range $[0.1-0.5]$ fm^{-3} (Wiringa, 1988).

the strength of the interaction among nucleons (Li et al., 2018). In general, the effective mass m_τ^* depends on the baryon density, the isospin asymmetry, and the momentum of the nucleons and is determined by the momentum dependent single nucleon potential

$$\frac{m_\tau^*}{m_\tau} = \left[1 + \frac{m_\tau}{\hbar^2 k}\frac{dU_\tau(n,I,k)}{dk}\right]^{-1}. \tag{7.1}$$

By employing the definition (7.1) at the Fermi momentum $k = k_F$, analytical expressions for the Landau effective mass are taken (see Section 2.1.5). In an inner window in Figure 7.1(a), the effective mass of the nucleons is plotted as a function of the baryon density, which at the saturation density n_s was found to be $m_\tau^*/m_\tau = 0.822$.

Another microscopic quantity of interest is the isoscalar potential which is defined as $U_{\rm iso} = (U_p + U_n)/2$ (Moustakidis, 2008). The momentum dependence of the isoscalar potential is important for extracting information about the SNM. In order to provide an additional check for the validity of the model parameters, which are customary, the calculation of the isoscalar potential is performed. As a more stingiest test, it has been compared to the ones predicted with the variational many body (VMB) theory (Li, 2004; Wiringa, 1988). Thus, in Figure 7.2 is displayed the isoscalar potential as a function of the baryon density, at four values of the momenta k in comparison to the VMB calculations (AV14 + UVII model). We found that the predictions of the present work are in a very good agreement with the VMB predictions up to $k \sim 2$ fm^{-1}, but also even for higher values of the momentum, where the tread is similar.

The nuclear symmetry potential (NSP), which refers to the isovector part of the nucleon mean-field potential in isospin ANM, can also depend on the temperature. Most studies concerning the NSP have been carried out for zero temperature, whereas the temperature dependence of the NSP so far has received little theoretical attention. The NSP potential describes the difference among the neutron and proton SPP in neutron-rich matter and has the form (Moustakidis, 2008)

$$U_{\rm sym}(n,I,k,T) = \frac{U_n(n,I,k,T) - U_p(n,I,k,T)}{2I}. \tag{7.2}$$

In Figure 7.3 is displayed the $U_{\rm sym}(n,I,k,T)$ as a function of $E_{\rm kin} = \hbar^2k^2/2m_n$ for $n = 0.16$ fm^{-3}, $I = 0.4$, and $T = 0$ MeV. The shaded region corresponds to empirical constraints (related to the systematic analysis of a large number of nucleon-nucleon scattering

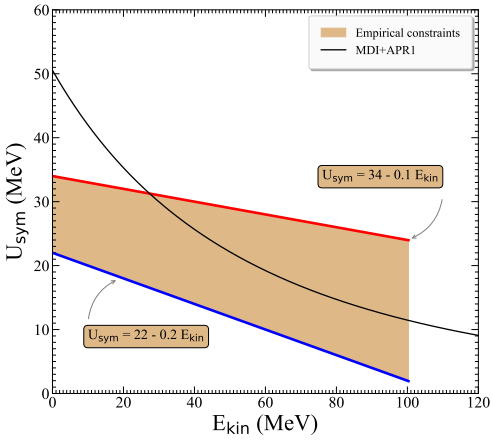

Figure 7.3: Nuclear symmetry potential as a function of kinetic energy for MDI+APR1 EoS. The shaded region represents the empirical constraints implied from nucleon-nucleon scattering experiments and charge-exchange reactions at beam energies up to 100 MeV (Lane, 1962).

experiments and (p,n) charge-exchange reactions at beam energies up to 100 MeV) extracted from the formula (Dalen et al., 2005; Lane, 1962; van Dalen et al., 2004; van Dalen et al., 2005)

$$U_{\text{sym}}(n, I, k, T) \approx a - bE_{\text{kin}}, \tag{7.3}$$

where $a \approx 22 - 34$ MeV and $b \approx 0.1 - 0.2$. The prediction of the present model lies inside the empirical region, except for very low values of E_{kin}. It is worth pointing out that with a proper parametrization of the MDI model, we would be able to mimic the results, concerning all SPP. However, in this study is focused on the predictions of the experimental properties of SNM (saturation density, energy per particle etc.). The latter is the most important part and achieved with high accuracy with the present model.

7.2 Free energy and proton fraction

A key quantity related to the calculation of the proton fraction via β-equilibrium is the free energy per particle. Figure 7.4 displays the free energy per particle as a function of the baryon density for temperatures in the range $[0, 60]$ MeV and the MDI+APR1 EoS for both (a) PNM and (b) SNM (in the following, we refer only to the MDI+APR1 EoS). As is expected due to the quantum character of the hadronic matter, thermal effects are more pronounced at low densities, while at high densities, there is a tendency for convergence. Moreover for practical reasons, it is convenient to have analytical expressions for the dependence of the free energy on both baryon density and temperature. Following the suggestion of Lu et al. (Lu et al., 2019), the following functional form is employed,

$$\frac{F}{A}(n, T) = a_0 + \left(a_1 + a_2 t^2\right) n + a_3 n^{a_4} + a_5 t^2 ln(n) + \left(a_6 t^2 + a_7 t^{a_8}\right)/n, \tag{7.4}$$

where $t = T/100$ MeV, and F/A and n are given in units of MeV and fm^{-3}, respectively. The parameters a_i of the fit, with $i = 0 - 8$, for the SNM and PNM are listed in Table 7.1.

Equation (7.4) is an excellent parameterization of the free energy per particle in the range of density 0.08 fm$^{-3} \leq n \leq 1$ fm^{-3} and temperature 0 MeV $\leq T \leq 60$ MeV. In addition, through Equation (2.50), the very good accuracy between the analytical and numerical calculation of the entropy from Equation (2.10), is confirmed.

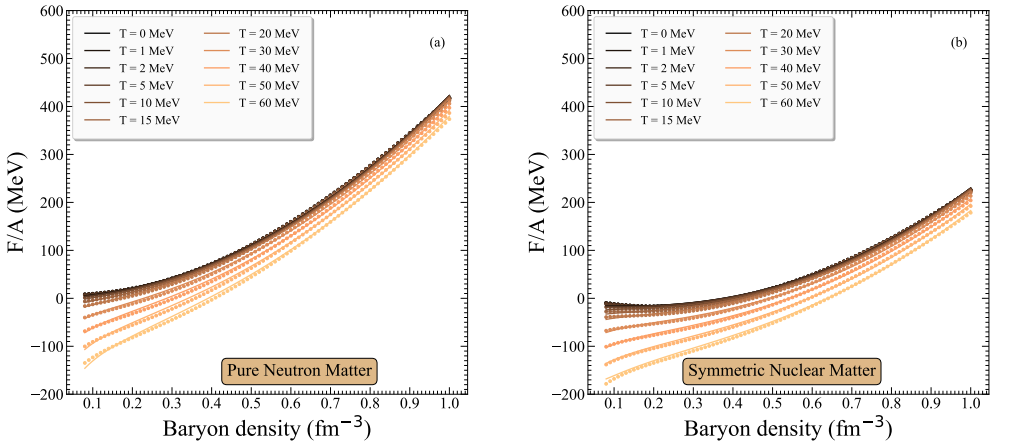

Figure 7.4: Free energy per particle as a function of baryon density for (a) PNM and (b) SNM for temperatures in the range $[0, 60]$ MeV and the MDI+APR1 EoS. Data and fits are presented by circles and solid lines, respectively. (The following figures also refer to the MDI+APR1 EoS.)

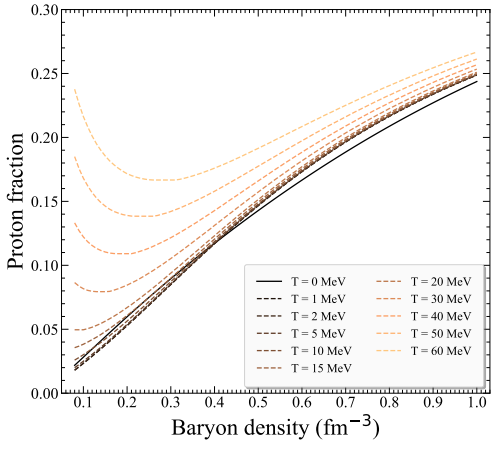

Figure 7.5: Proton fraction as a function of baryon density for temperatures in the range $[0, 60]$ MeV. The cold configuration is presented by the solid line, while hot configurations are presented by the dashed ones.

Table 7.1: Parameters of Equation (7.4) for PNM and SNM of MDI+APR1 EoS.

Parameters	PNM	SNM
a_0	0.000	-12.000
a_1	37.814	-54.000
a_2	-117.379	-140.000
a_3	385.000	296.000
a_4	2.079	2.261
a_5	150.000	211.000
a_6	-90.000	-64.000
a_7	94.000	88.000
a_8	2.140	2.350

The knowledge of the proton fraction is very important, since it is related not only to the specific structure of a neutron star but also to the direct (nucleonic) URCA process (Yakovlev and Pethick, 2004). Figure 7.5 displays the proton fraction as a function of the baryon density for temperatures in the range $[0, 60]$ MeV. Our predictions are very close to those found recently in Lu et al. (Lu et al., 2019), where the authors employed a different nuclear model and approach. In particular, while in the low-density region, the proton fraction is very sensitive to the temperature, in the high-density region, the thermal effects are very mild. This is a direct consequence of the similar sensitivity of the free energy per particle to temperature shown in Figure 7.4. Furthermore, at a high temperature, the free symmetry energy plays an insignificant role, and, consequently, the nuclear system tends to become more symmetric.

7.3 Equation of state and the thermal and adiabatic indices

Figure 7.6 displays the pressure as a function of the baryon density for (a) temperatures in the range $[0, 60]$ MeV and (b) lepton fractions and entropies per baryon in the ranges $[0.2, 0.4]$ and $[1, 3]$ k_B, respectively. In particular, it presents one EoS for the cold catalyzed matter, 10 isothermal EoSs, and 9 isentropic EoSs.

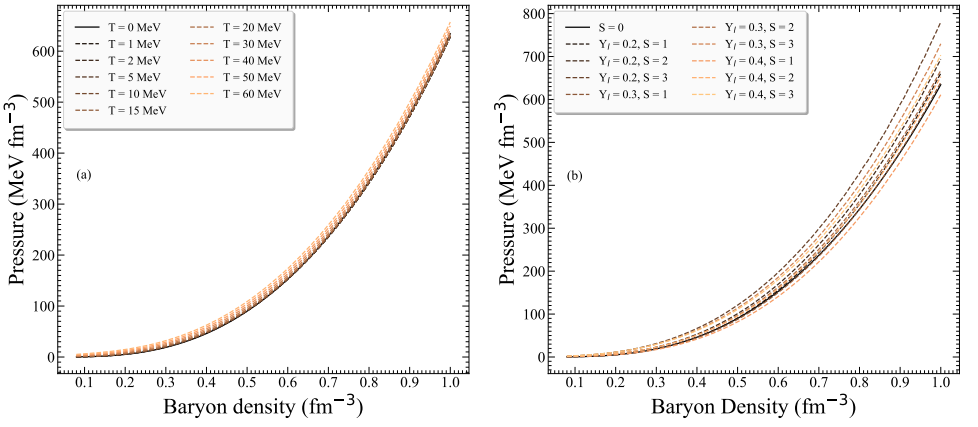

Figure 7.6: Pressure as a function of baryon density for (a) temperatures in the range $[0, 60]$ MeV and (b) lepton fractions and entropies per baryon in the ranges $[0.2, 0.4]$ and $[1, 3]$ k_B, respectively. The cold configuration is presented by the solid line, while hot configurations are presented by the dashed ones.

In order to study in detail the effects of the temperature on the EoS, Figure 7.7 displays the (a) energy density and (b) pressure thermal components as functions of the baryon density. Both the thermal energy density and pressure exhibit a non-monotonic density dependence behavior, with this effect being rather significant in thermal pressure. In this case, while the individual thermal pressures of protons and neutrons at fix partial densities are increasing, the isospin asymmetry is decreasing with temperature, which reduces the total baryon pressure; an effect which is also presented in Figure 7.5.

The next functional step is studying the thermal index, a quantity which fully relies on the energy and pressure thermal components. In Figure 7.8 is displayed the thermal index as a function of the baryon density for temperatures in the range $[1, 60]$ MeV. An important density dependence is clearly presented, especially for temperatures in the range $[1, 30]$ MeV. At higher

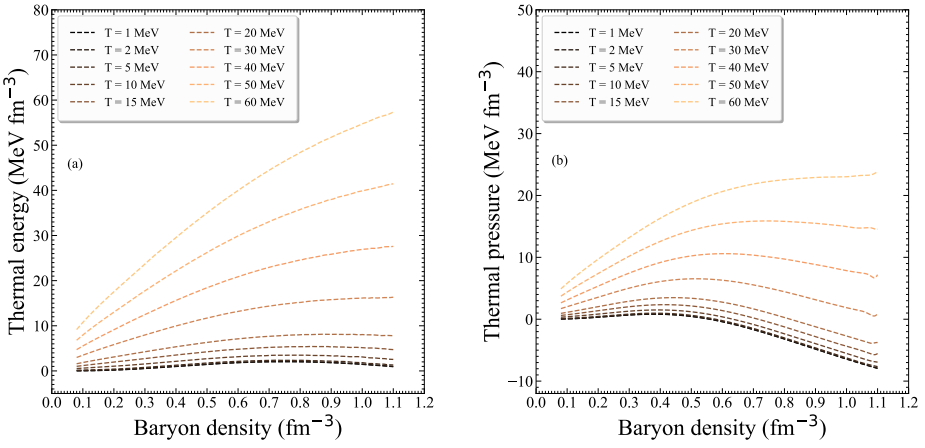

Figure 7.7: Thermal component of (a) energy density and (b) pressure as a function of baryon density for temperatures in the range $[1, 60]$ MeV.

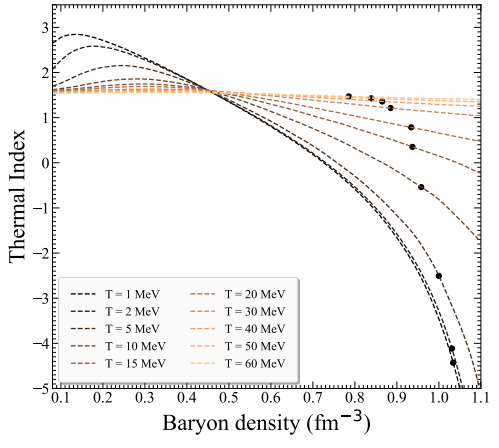

Figure 7.8: Thermal index as a function of baryon density for temperatures in the range $[1, 60]$ MeV. Black circles represent the central baryon density at which the maximum mass configuration appears.

temperatures ($T > 30$ MeV), the thermal index has an almost constant value, as its density dependence is rather insignificant.

We note here that due to the thermal effects that have been analyzed, Equation (2.74) might be strongly violated, in particular for EoSs with low values of temperatures ($T \leq 10$ MeV) and, as a consequence, low values of proton fraction, where the energy density and pressure thermal components might even become negative (Lu et al., 2019).

In the case of isentropic EoSs, both the adiabatic index and the speed of sound have been studied. In Figure 7.9(a) is displayed the adiabatic index as a function of the baryon density for lepton fractions and entropies per baryon in the ranges $[0.2, 0.4]$ and $[1, 3]$ k_B, respectively. For a constant lepton fraction, the decreasing of the entropy per baryon leads to higher values of the central baryon density at which the maximum mass appears.

In addition, Figure 7.9(b) presents the square speed of sound in units of speed of light as a function of the baryon density. In this scenario, no EoSs, including the one with cold catalyzed matter, ever exceed the causality limit (see also (Heiselberg and Hjorth-Jensen, 2000)). It has to

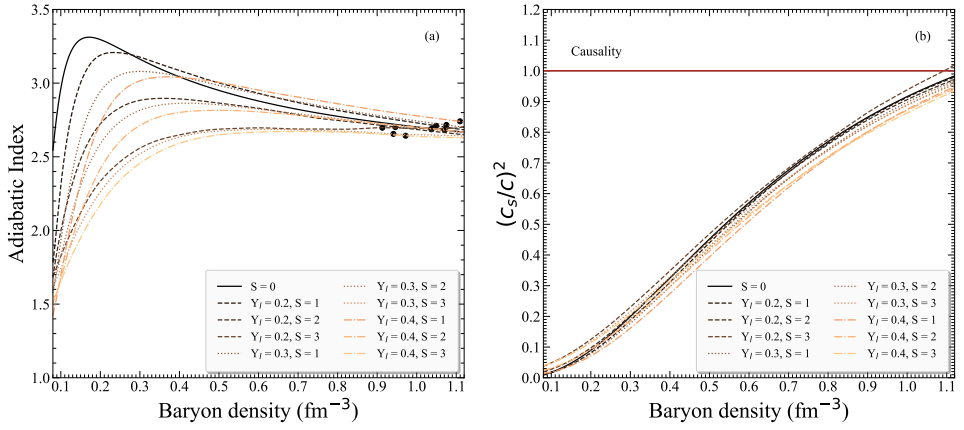

Figure 7.9: (a) Adiabatic index and (b) square speed of sound in units of speed of light as a function of baryon density for lepton fractions and entropies per baryon in the ranges $[0.2, 0.4]$ and $[1, 3]$ k_B, respectively. Black circles represent the central baryon density at which the maximum mass configuration appears. The cold configuration is presented by the solid line.

be emphasized that one of the major advantages of the MDI model is to prevent the EoS from reaching the causality point. The latter is effective even to higher values of neutron star baryon density than the ones that correspond to the maximum mass configuration.

7.4 Thermal effects on non-rotating neutron stars

We now concentrate our study on the bulk properties of non-rotating neutron stars at the maximum mass configuration. In Figure 7.10 is displayed the gravitational mass as a function of the corresponding equatorial radius for temperatures in the range $[0, 60]$ MeV. It is worth clarifying that the nonhomogeneous nuclear matter phase disappears when the temperature is higher than $T \sim 15$ MeV. To be more specific, the critical temperature T_c where this transition (known as liquid-gas phase transition) is achieved is model-dependent. However, a well accepted value is close to $T_c = 15$ MeV (Haensel et al., 2007; Shen et al., 1998).

We found that in the case of the maximum gravitational mass, thermal effects are negligible. In particular, while the introduction of temperature ($T = 1$ MeV) leads to a lower maximum gravitational mass than the cold neutron star, the increase of temperature leads to an increasing behavior of the maximum gravitational mass. The above results confirm similar studies concerning thermal effects on the maximum neutron star mass (Burgio and Schulze, 2010; Burgio et al., 2007; Figura et al., 2020; Lu et al., 2019; Nicotra et al., 2006). However, thermal effects appear to be more important for the radius of neutron stars. For a neutron star with $M_{\rm gr} = 1.4\ M_\odot$ the radius can reach values even twice the radius of the cold one. It is worth noting that after $T = 20$ MeV, there are no configurations for a neutron star with $M_{\rm gr} = 1.4\ M_\odot$. Moreover, the maximum baryon mass decreases with increasing temperature up to $T = 40$ MeV, while for higher temperatures, a relatively low increase is observed. We concluded that hot neutron stars can exist with maximum baryon masses at lower values compared to the cold ones. These bulk properties are summarized in Table 7.2. It has to be noted here that in the case of a very hot neutron star ($T = 60$ MeV), the central density is $\sim 24\%$ lower compared to the cold case. The reason is that while the gravitational masses are comparable, the corresponding radius at $T = 60$ MeV is $\sim 35\%$ higher than the cold case. In particular, at higher temperatures, thermal pressure, which added to the baryonic one, becomes appreciable and pushes the neutron star

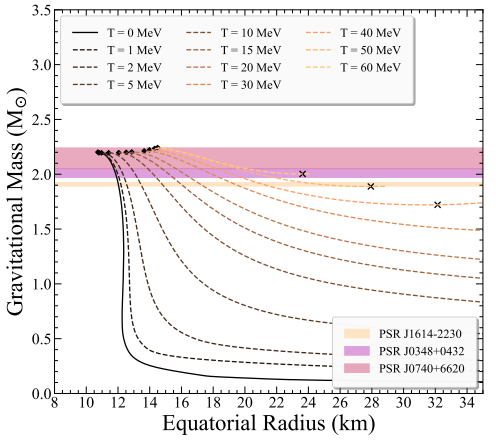

Figure 7.10: Gravitational mass as a function of equatorial radius for temperatures in the range $[0, 60]$ MeV at the non-rotating configuration. The cold configuration is presented by the solid line, while hot configurations are presented by the dashed ones. The shaded regions from bottom to top represent the PSR J1614-2230 (Arzoumanian et al., 2018), PSR J0348+0432 (Antoniadis et al., 2013), and PSR J0740+6620 (Cromartie et al., 2019) pulsar observations for possible maximum mass. Black diamonds correspond to the maximum mass configuration in each case, while black crosses correspond to the minimum mass configuration. (The remaining minimum masses are positioned at higher values of equatorial radius.)

matter against gravity. In this case, while gravitational mass is almost unaffected, as it is mainly determined by the high-density behavior of the EoS, the radius of the star, which is determined by the low- and intermediate-density domain of the EoS, increases appreciably. As a result, the central baryon density of a hot neutron star decreases compared to the cold one.

By considering an isentropic EoS, the mentioned quantities alter in correspondence to lepton fraction and entropy per baryon. For a visual effect, Figure 7.11 displays the gravitational mass as a function of the corresponding equatorial radius for lepton fractions and entropies per baryon in the ranges $[0.2, 0.4]$ and $[1, 3]$ k_B, respectively. In particular, EoSs with constant lepton fractions are compared. The increase of the entropy per baryon in neutron stars leads to lower baryon masses, as well as lower central baryon densities. In contrast to these quantities, the maximum

Table 7.2: Summary of non-rotating isothermal neutron star bulk properties. The properties correspond to the maximum gravitational mass configuration.

T (MeV)	$M_b^{\max}$ $(M_\odot)$	$M_{gr}^{\max}$ $(M_\odot)$	$R_{\max}$ (km)	n_b^c (fm^{-3})	$R_{1.4}$ (km)
0	2.622	2.202	10.734	1.038	12.353
1	2.599	2.195	10.809	1.034	12.633
2	2.567	2.195	10.963	1.031	13.321
5	2.501	2.195	11.407	1.000	15.150
10	2.427	2.197	12.044	0.958	18.315
15	2.380	2.199	12.520	0.937	21.676
20	2.345	2.203	12.869	0.934	25.922
30	2.310	2.212	13.650	0.885	-
40	2.307	2.223	13.981	0.865	-
50	2.313	2.235	14.312	0.839	-
60	2.342	2.244	14.497	0.785	-

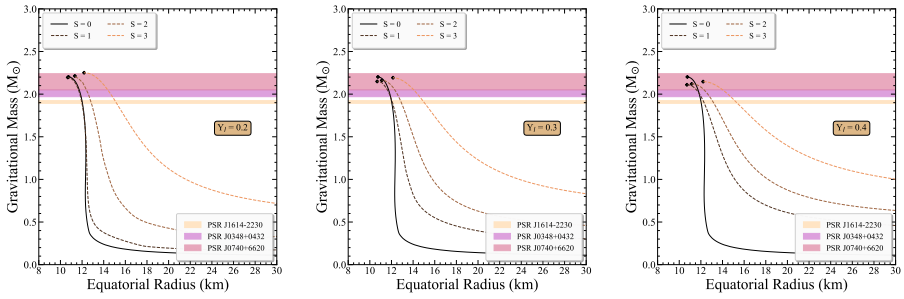

Figure 7.11: Gravitational mass as a function of equatorial radius for lepton fractions and entropies per baryon in the ranges $[0.2, 0.4]$ and $[1, 3]$ k_B, respectively, at the non-rotating configuration. The cold configuration is presented by the solid line, while hot configurations are presented by the dashed ones. The shaded regions from bottom to top represent the PSR J1614-2230 (Arzoumanian et al., 2018), PSR J0348+0432 (Antoniadis et al., 2013), and PSR J0740+6620 (Cromartie et al., 2019) pulsar observations for possible maximum mass. Black diamonds correspond to the maximum mass configuration in each case.

Table 7.3: Summary of non-rotating isentropic neutron star bulk properties. The properties correspond to the maximum gravitational mass configuration.

Y_l	S (k_B)	$M_b^{\max}$ ($M_\odot$)	$M_{gr}^{\max}$ ($M_\odot$)	$R_{\max}$ (km)	n_b^c (fm^{-3})	T_c (MeV)	$R_{1.4}$ (km)
0.2	1	2.612	2.196	10.678	1.049	31.5	12.384
	2	2.589	2.213	11.335	0.946	66.2	13.744
	3	2.530	2.251	12.188	0.913	129.7	17.749
0.3	1	2.515	2.149	10.678	1.075	29.6	12.920
	2	2.485	2.161	11.103	1.037	63.5	14.303
	3	2.440	2.192	12.141	0.941	108.3	18.305
0.4	1	2.430	2.110	10.712	1.110	28.5	13.679
	2	2.398	2.120	11.154	1.071	59.9	15.316
	3	2.354	2.147	12.208	0.972	97.8	19.922

gravitational mass, the corresponding equatorial radius, and the central temperature are increasing as the entropy per baryon increases. As the center of the star becomes hotter with increasing entropy per baryon, the baryon mass that it can withstand is lower. Last but not least, for neutron stars with $M_{\rm gr} = 1.4\ M_\odot$, the radius is increasing, where for $S = 3$, it can be 61% greater than the $R_{1.4}$ of the cold configuration. These bulk properties are summarized in Table 7.3.

Finally, it is worth pointing out that the maximum gravitational/baryon mass as a function of temperature presents a strong dependence on the nuclear EoS (da Silva Schneider et al., 2020; Kaplan et al., 2014; Raduta et al., 2020; Sumiyoshi et al., 1999).

7.5 Thermal effects on rotating neutron stars

In Figure 7.12 is displayed the gravitational mass as a function of the corresponding equatorial radius at the mass-shedding limit for temperatures in the range $[0, 60]$ MeV. In general, as the temperature increases, the bulk properties of neutron stars at the maximum mass configuration[1] are affected. In particular, the dependence of the baryon mass on the temperature exhibits

[1] At the mass-shedding limit, it is considered that maximum mass corresponds to Kepler frequency (Friedman and Stergioulas, 2013).

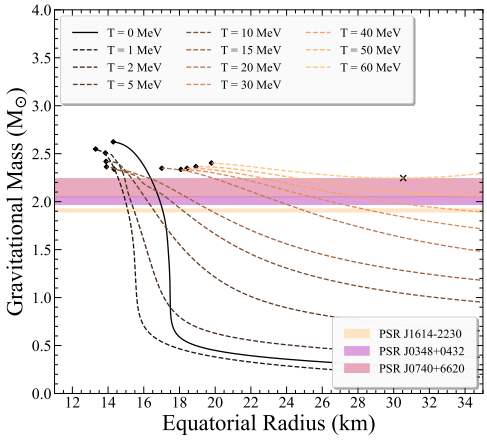

Figure 7.12: Gravitational mass as a function of equatorial radius for temperatures in the range $[0, 60]$ MeV, at the rotating configuration with Kepler frequency. The cold configuration is presented by the solid line, while the hot configurations are presented by the dashed ones. The shaded regions from bottom to top represent the PSR J1614-2230 (Arzoumanian et al., 2018), PSR J0348+0432 (Antoniadis et al., 2013), and PSR J0740+6620 (Cromartie et al., 2019) pulsar observations with possible maximum neutron star mass. Black diamonds correspond to the maximum mass configuration in each case, while the black cross corresponds to the minimum mass configuration (the remaining minimum masses are positioned at higher values of equatorial radius).

similar behavior with the non-rotating case. However, the gravitational mass is decreasing with increasing temperature up to $T = 30$ MeV, while for higher values of temperature, an inverse behavior is observed. Similar to the non-rotating case, while the introduction of temperature $(T = 1$ MeV$)$ leads to a lower value of the corresponding equatorial radius than the cold neutron star, the equatorial radius follows an increasing path with the temperature, where for neutron stars with $M_{\rm gr} = 1.4\ M_{\odot}$, it can reach several times the radius of the cold one with a dramatic increase. These results play a significant role in the time evolution of hot and rapidly rotating neutron stars. The temperature dependence of the maximum gravitational mass and corresponding equatorial radius is well reflected on the corresponding temperature dependence of the rest of the neutron star properties, including the central baryon density, Kepler frequency, Kerr parameter, moment of inertia, and ratio of rotational kinetic to gravitational binding energy, as displayed in Table 7.4.

In the case of isentropic EoSs, where Figure 7.13 presents them, the increase of entropy per baryon affects the neutron star bulk properties in the maximum mass configuration at the mass-shedding limit. To be more specific, considering a constant lepton fraction, the bulk properties under consideration are decreasing as the entropy per baryon; consequently, the temperature at the center of the star increases. Exceptionally, the equatorial radius follows the opposite direction, as it is increasing with the entropy per baryon. This effect is more pronounced at $M_{\rm gr} = 1.4\ M_{\odot}$, where the radius can rise up to 49% of the cold star. These bulk properties are summarized in Table 7.5.

7.6 Minimum mass of neutron stars

Apart from the maximum neutron star mass, the minimum one is also of great interest in astrophysics. For reasons of completeness, the thermal and rotation effects on the minimum mass of neutron stars are studied. The existence of a minimum neutron star configuration is a universal

Table 7.4: Summary of uniformly rotating isothermal neutron star bulk properties at the mass-shedding limit. The properties correspond to the maximum gravitational mass configuration.

T (MeV)	$M_b^{\max}$ ($M_\odot$)	$M_{gr}^{\max}$ ($M_\odot$)	$R_{\max}$ (km)	n_b^c (fm^{-3})	$R_{1.4}$ (km)	$f_{\max}$ (Hz)	$\mathcal{K}_{\max}$	$I_{\max}$ (10^{38} kg m^2)	$T/W\vert_{\max}$ (10^{-1})
0	3.085	2.623	14.292	0.927	17.413	1689	0.692	3.949	1.299
1	2.983	2.549	13.299	0.935	15.504	1613	0.647	3.651	1.137
2	2.899	2.508	13.848	0.877	16.446	1525	0.622	3.597	1.055
5	2.730	2.419	13.887	0.879	18.501	1384	0.545	3.227	0.805
10	2.593	2.364	13.911	0.934	22.520	1285	0.478	2.914	0.612
15	2.514	2.338	14.340	0.934	26.895	1205	0.442	2.813	0.521
20	2.485	2.348	17.011	0.911	37.543	1226	0.456	2.875	0.549
30	2.427	2.336	18.079	0.883	-	1123	0.422	2.873	0.470
40	2.427	2.347	18.425	0.873	-	1090	0.416	2.949	0.460
50	2.439	2.365	18.920	0.848	-	1053	0.414	3.084	0.460
60	2.496	2.403	19.793	0.762	-	1003	0.433	3.490	0.531

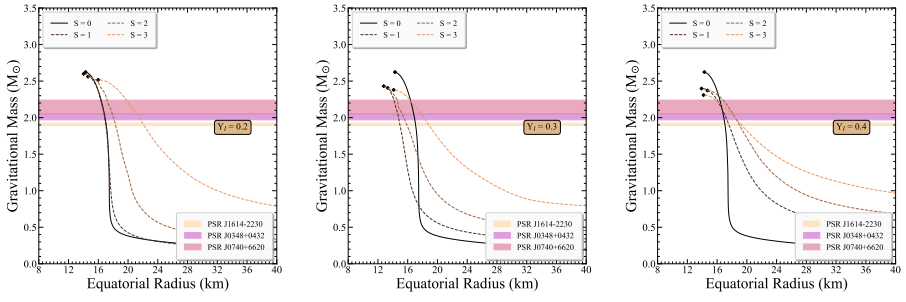

Figure 7.13: Gravitational mass as a function of equatorial radius for lepton fractions and entropies per baryon in the ranges $[0.2, 0.4]$ and $[1, 3]$ k_B, respectively, at the rotating configuration with Kepler frequency. The cold configuration is presented by the solid line, while the hot configurations are presented by the dashed ones. The shaded regions from bottom to top represent the PSR J1614-2230 (Arzoumanian et al., 2018), PSR J0348+0432 (Antoniadis et al., 2013), and PSR J0740+6620 (Cromartie et al., 2019) pulsar observations with possible maximum neutron star mass. Black diamonds correspond to the maximum mass configuration in each case.

Table 7.5: Summary of uniformly rotating isentropic neutron star bulk properties at the mass-shedding limit. The properties correspond to the maximum gravitational mass configuration.

Y_l	S (k_B)	$M_b^{\max}$ ($M_\odot$)	$M_{gr}^{\max}$ ($M_\odot$)	$R_{\max}$ (km)	n_b^c (fm^{-3})	T_c (MeV)	$R_{1.4}$ (km)	$f_{\max}$ (Hz)	$\mathcal{K}_{\max}$	$I_{\max}$ (10^{38} kg m^2)	$T/W\vert_{\max}$ (10^{-1})
0.2	1	3.050	2.599	14.028	0.958	29.6	17.498	1715	0.684	3.775	1.269
	2	2.954	2.560	14.621	0.926	65.2	19.415	1594	0.641	3.694	1.107
	3	2.808	2.517	15.970	0.879	125.3	25.912	1391	0.568	3.621	0.857
0.3	1	2.817	2.431	12.780	0.979	27.9	15.770	1575	0.601	3.158	0.976
	2	2.743	2.407	13.314	0.940	59.5	17.590	1458	0.565	3.143	0.861
	3	2.633	2.380	14.116	0.908	105.5	22.861	1261	0.493	3.104	0.651
0.4	1	2.733	2.398	13.906	1.052	27.5	19.454	1661	0.613	2.972	1.005
	2	2.659	2.371	14.702	1.002	57.5	21.975	1530	0.576	2.965	0.885
	3	2.519	2.309	14.185	0.943	95.6	25.020	1225	0.466	2.841	0.580

feature, independent of the details of the EoS (Colpi et al., 1989), for example, the concept of the minimum mass involved in the case of a neutron star in a close binary system with a more compact partner (neutron star or black hole; (Suwa et al., 2018)). During evolution, the lower-mass neutron star transfers mass to the more massive object, a process that ultimately leads to approaching its minimum value. Finally, crossing this value, the neutron star reaches a nonequilibrium configuration (Haensel et al., 2002). In particular, it is pointed out by several authors that a neutron star will undergo an explosion if its mass drops to the minimum possible equilibrium value (Blinnikov et al., 1984; Colpi et al., 1989; Colpi et al., 1991; Sumiyoshi et al., 1998). In most studies, the minimum mass is studied in the framework of cold catalyzed nuclear matter. In the present work, previous studies are extended in order to include rotation and thermal effects, which are related to a more realistic process. The results are displayed in Table 7.6.

In the case of isothermal configurations, the increase in temperature leads to a significant increase of the minimum mass, especially for high values of temperature. On the other hand, the rotation effect is important only for high-temperature configurations. The latter occurs because of the low values of Kepler frequency at low temperatures. In this case, the difference in minimum mass between the non-rotating and maximally rotating configurations is almost imperceptible.

Similarly, in adiabatic cases, higher values of entropy per baryon lead to higher values of minimum mass (for a constant lepton fraction). Moreover, for constant entropy per baryon, neutron stars that are rich in leptons exhibit higher values of minimum mass. However, the most distinctive feature in isentropic configurations is the negligible effect of the rotation on the minimum mass, in most of the cases. The explanation of this behavior is similar to that of isothermal cases, that is, the low corresponding values of Kepler frequency.

Table 7.6: Minimum mass of isothermal and isentropic neutron stars. The abbreviation "N.R." corresponds to the non-rotating configuration, while "M.R." corresponds to the maximally rotating one.

$M_{\rm gr}^{\rm min}$ ($M_\odot$)	$T=0$ (MeV)	$T=1$ (MeV)	$T=2$ (MeV)	$T=5$ (MeV)	$T=10$ (MeV)	$T=15$ (MeV)	$T=20$ (MeV)	$T=30$ (MeV)	$T=40$ (MeV)
N.R.	0.080	0.098	0.172	0.353	0.652	0.893	1.116	1.471	1.720
M.R.	0.081	0.098	0.172	0.356	0.671	0.915	1.142	1.545	1.848

	$T=50$ (MeV)	$T=60$ (MeV)
	1.888	2.003
	2.053	2.242

	$Y_l=0.2$			$Y_l=0.3$			$Y_l=0.4$		
	$S=1$	$S=2$	$S=3$	$S=1$	$S=2$	$S=3$	$S=1$	$S=2$	$S=3$
	0.172	0.270	0.569	0.285	0.410	0.670	0.426	0.559	0.821
	0.186	0.318	0.590	0.320	0.417	0.683	0.432	0.569	0.823

7.7 Sequences of constant baryon mass and the threshold mass of cold, catalyzed neutron stars

Figure 7.14 displays sequences of constant baryon mass up to the one that corresponds to the maximum gravitational mass configuration in the case of cold catalyzed matter. From these sequences, it is clear that, differently from the gravitational mass where changes are negligible, as the frequency decreases, starting from the Kepler frequency, the star gets considerably more dense. The effect reaches its peak for baryon masses close to the one that corresponds to the maximum gravitational mass configuration ($M_b = 2.62\ M_\odot$), and it will be reflected in the particle composition and thermal properties. In addition, the region where a possible phase

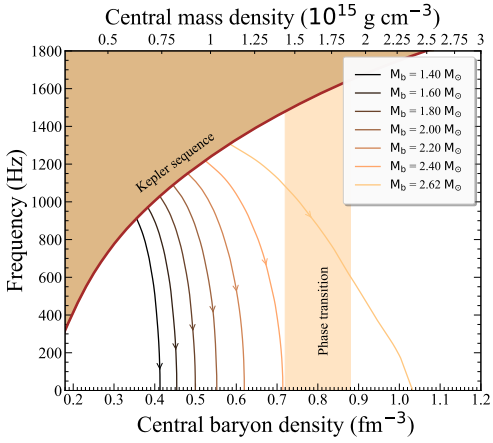

Figure 7.14: Frequency as a function of central stellar baryon density for constant baryon mass sequences. The shaded region represents the forbidden region for the star, where the boundary solid line marks the Kepler frequency. Arrows are shown to guide the evolution of the star. A region where a possible phase transition may occur is also noted (Baym et al., 2018). In addition, the central mass density is presented in the top axis corresponding to central baryon density.

transition may occur (0.72 fm$^{-3} \leq n_{\rm tr} \leq 0.88$ fm^{-3}; (Baym et al., 2018)) is indicated. The results of Baym et al. (Baym et al., 2018) are only indicative and simply provide a possible region of transition density (from baryonic to quark matter). Other similar studies predict similar or different corresponding regions. Obviously, more robust (theoretical and experimental) constraints concerning the phase transition are needed.

In this case, Figure 7.14 may help to indicate the expected region of the central densities (for a constant baryon mass) where a possible phase transition may take place during the evolution of a neutron star. In particular, this study may be useful for the evolution of pulsars and the appearance of the back-bending process (Glendenning, 2000).

Finally, for a given cold, catalyzed EoS, one can define the threshold binary mass that distinguishes the prompt ($M_{\rm st}^{\rm max} > M_{\rm thres}$) from the delayed ($M_{\rm st}^{\rm max} < M_{\rm thres}$) collapse. A relation that describes the threshold mass as a function of the compactness was found recently in Köppel et al. (Köppel et al., 2019) and is given by

$$M_{\rm thres} = M_{\rm st}^{\rm max} \left(3.06 - \frac{1.01}{1 - 1.34\beta_{\rm max}} \right), \tag{7.5}$$

where β is the compactness parameter of the star, defined as

$$\beta = \frac{G}{c^2} \frac{M}{R}, \tag{7.6}$$

and $\beta_{\rm max}$ corresponds to the maximum mass configuration. In our case, employing the values of $M_{\rm st}^{\rm max}$ and $\beta_{\rm max}$, it has been found that $M_{\rm thres} = 2.994\ M_\odot$. Although the remnant is expected to rotate differentially and not uniformly, the threshold mass is presented in this study in order to show that uniform rotation cannot reach the values of gravitational and baryon mass, as Table 7.4 indicates.

7.8 Sequences of constant baryon mass on rotating neutron stars at finite temperature

The sequences of constant baryon mass are a very useful way to study thermal effects on the evolution and instability conditions of hot neutron stars. However, as isothermal EoSs have been constructed, the same baryon mass configuration in the temperature range $[0, 60]$ MeV have been studied, and eventually constructed a sequence related to the cooling of a neutron star. In particular, the quantities under consideration were the Kepler frequency, the central baryon density, and the temperature of each EoS.

Figure 7.15(a) displays the Kepler frequency as a function of temperature for four baryon masses. As the temperature increases, the Kepler frequency presents a reverse behavior. More specifically, while until $T = 15$ MeV, the reduction of the Kepler frequency is rather abrupt, for higher temperatures, a smoother one is observed. The dependence of the Kepler frequency on the temperature is described by the formula

$$f(T) = a_0 + a_1 T^3 + a_2 \exp[a_3 T] \quad \text{(Hz)}, \tag{7.7}$$

where f and T are given in units of Hz and MeV, respectively, and the coefficients a_i, with $i = 0 - 3$, are presented in Table 7.7.

In addition, Figure 7.15(b) displays the Kepler frequency as a function of the central baryon density for four baryon masses. The central baryon density presents exceptional behavior in that as the temperature increases, the central baryon density is also increased, but for high values of temperature, it exhibits an inverse behavior. In any case, these effects are mild. However, it is worth noticing that the corresponding effect is sizable, leading to a reduction of two to three times the Kepler frequency. Furthermore, the most distinctive feature is the appearance of an almost linear relation between the Kepler frequency and the central baryon density for a constant value of temperature, especially for low ones. Moreover, and quite notably, it has been found that for high values of temperature ($T \geq 30$ MeV), every sequence of constant baryon mass not only presents similar behavior but also moves along a linear relation described as

$$f(n_b^c) = -473.144 + 2057.271 n_b^c \quad \text{(Hz)}, \tag{7.8}$$

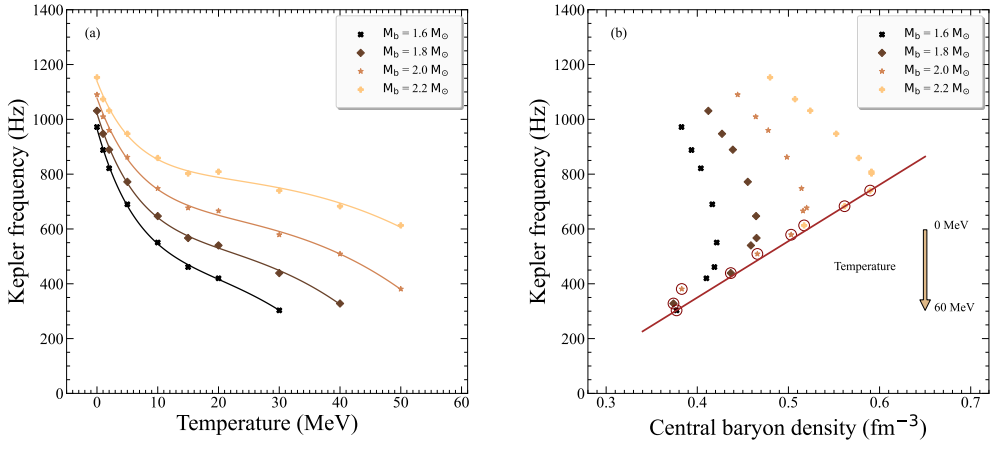

Figure 7.15: Kepler frequency as a function of (a) temperature and (b) central baryon density for constant baryon mass sequences. (a) Solid lines correspond to fits originated from Equation (7.7). (b) The solid line corresponds to Equation (7.8) and open circles mark the high-temperature region ($T \geq 30$ MeV).

Table 7.7: Coefficients of empirical relations (7.7) and (7.9) for baryon masses in the range $[1.6 - 2.2]\ M_\odot$.

Coefficients	Baryon Mass			
	$1.6\ M_\odot$	$1.8\ M_\odot$	$2.0\ M_\odot$	$2.2\ M_\odot$
$a_0\ (\times 10^2)$	4.259	5.284	6.414	7.863
$a_1\ (\times 10^{-3})$	-4.787	-3.202	-2.099	-1.443
$a_2\ (\times 10^2)$	5.401	4.929	4.363	3.530
$a_3\ (\times 10^{-1})$	-1.468	-1.443	-1.424	-1.636
$b_0\ (\times 10^{-1})$	4.273	4.466	4.798	5.470
$b_1\ (\times 10^{-2})$	-0.075	0.638	1.138	1.204
$b_2\ (\times 10^{-6})$	-1.699	-1.754	-1.405	-0.926
$b_3\ (\times 10^{-2})$	-4.473	-3.512	-3.609	-6.640
$b_4\ (\times 10^{-1})$	-3.299	-3.608	-3.357	-2.389

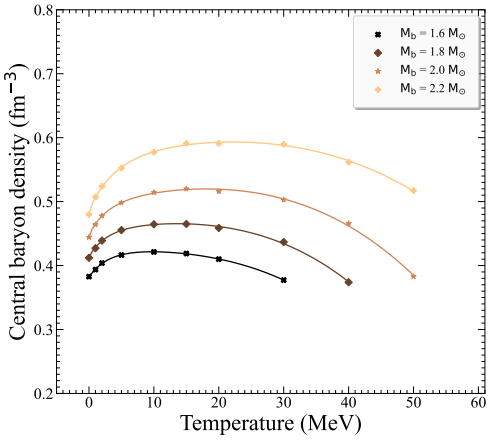

Figure 7.16: Central baryon density as a function of temperature for constant baryon mass sequences. Solid lines correspond to fits originated from Equation (7.9). The configuration corresponds to the mass-shedding limit.

where f and n_b^c are given in units of Hz and fm^{-3}, respectively. Equation (7.8) is very useful, since it directly relates the Kepler frequency with the central baryon density of a very hot neutron star, independently of the corresponding baryon mass. In addition, this relation defines the allowed region for rotation with the Kepler frequency of a hot neutron star for a specific value of the central baryon density, and vice versa.

Since it is interesting to study the dependence of the central baryon density on the temperature (for a neutron star spinning with the Kepler frequency), Figure 7.16 provides the central baryon density as a function of the temperature for four baryon masses. While for temperatures up to $T = 15$ MeV, the central baryon density is increased, for higher ones, it follows the opposite path, as its nonmonotonic behavior is presented. This behavior can be described by the formula

$$n_b^c(T) = b_0 + b_1 T^{1/2} + b_2 T^3 + b_3 \exp[b_4 T] \quad (\text{fm}^{-3}), \tag{7.9}$$

where n_b^c and T are given in units of fm^{-3} and MeV, respectively, and the coefficients b_i, with $i = 0 - 4$, are presented in Table 7.7.

It has to be noted that for a given value of baryon mass, the stability range of a neutron star is defined in a specific temperature range. This is the reason why, in the corresponding figures, there are no configurations for some temperatures and baryon masses.

7.9 Moment of inertia, Kerr parameter, and ratio T/W on rotating neutron stars

The study of rotating neutron stars offers much more information concerning the EoS compared to non-rotating ones. The present work is focused on studying the moment of inertia, the Kerr parameter, and the ratio of rotational kinetic to gravitational binding energy (T/W) at the mass-shedding limit.

Figure 7.17(a) displays the dimensionless moment of inertia as a function of the compactness parameter for isothermal neutron stars. The dimensionless moment of inertia provides an important constraint for the interior structure of neutron stars. Although for low values of temperature, $T \leq 2$ MeV, the dimensionless moment of inertia is higher than the cold neutron star, for temperatures $T > 2$ MeV, the reverse behavior is presented. This result points to the conclusion that the increase of temperature, except for some specific cases ($T < 2$ MeV), leads to lesser compact objects than the cold neutron star.

Figure 7.17(b) displays the dimensionless moment of inertia as a function of the compactness parameter for isentropic neutron stars. In general, the increase of the entropy per baryon with a constant lepton fraction, leads to lesser compact objects with lower values to a dimensional moment of inertia than the cold neutron star. There are some specific cases, $Y_l = 0.2$ and 0.3 and $S = 1$, where these values exceed the limit introduced by the cold neutron star.

A quantity directly related to black holes and neutron stars is the Kerr parameter (dimensionless spin parameter), which is defined as

$$\mathcal{K} \equiv \frac{c}{G}\frac{J}{M^2} = \frac{c}{G}\frac{I\Omega}{M^2}. \tag{7.10}$$

Its importance lies with the mass-shedding limit, where it takes the maximum allowed value. As shown in Koliogiannis & Moustakidis (Koliogiannis and Moustakidis, 2020), this limit represents an indicator of the final fate of the collapse of a rotating compact star. In fact, it was found in a recent work (Koliogiannis and Moustakidis, 2020) that the Kepler angular velocity for a cold

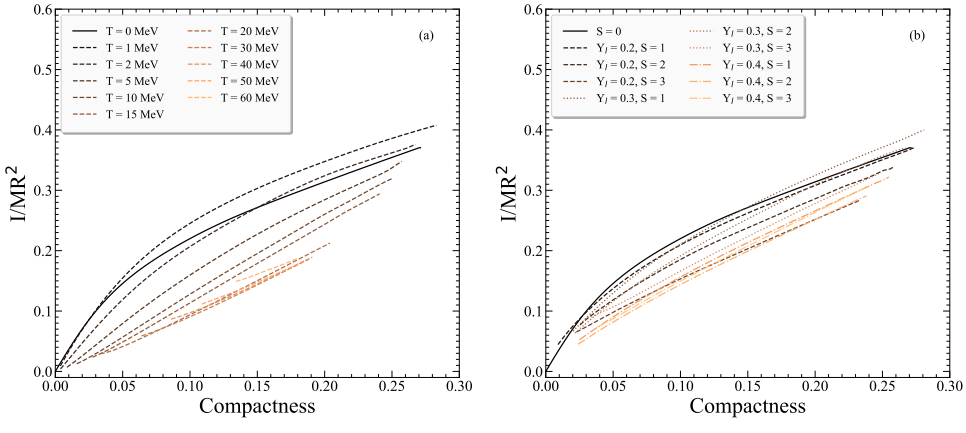

Figure 7.17: Dimensionless moment of inertia as a function of compactness parameter for (a) temperatures in the range $[0, 60]$ MeV and (b) lepton fractions and entropies per baryon in the ranges $[0.2, 0.4]$ and $[1, 3]$ k_B, respectively. The cold configuration is presented by the solid line, while hot configurations are presented by the dashed ones. The configuration corresponds to the mass-shedding limit.

neutron star is given by an almost EoS-independent formula,

$$\Omega_{\rm k} = 2\pi \mathcal{C}_{\rm rot} \left(\frac{M^{\rm rot}_{\rm max}}{M_\odot}\right)^{1/2} \left(\frac{10{\rm km}}{R^{\rm rot}_{\rm max}}\right)^{3/2}, \tag{7.11}$$

while the moment of inertia corresponding to the Kepler frequency is given by (see also (Shao et al., 2020))

$$\frac{I_{\rm k}}{M^{\rm rot}_{\rm max}(R^{\rm rot}_{\rm max})^2} \simeq 1.379\beta_{\rm max}, \tag{7.12}$$

where

$$\beta_{\rm max} = \frac{G}{c^2}\frac{M^{\rm rot}_{\rm max}}{R^{\rm rot}_{\rm max}}. \tag{7.13}$$

From Equations (7.10) - (7.12), it has been found that, in a very good approximation, the Kerr parameter, at the Kepler frequency (mass-shedding limit) for a cold, catalyzed neutron star is given by the simple universal expression

$$\mathcal{K}_{\rm k} \simeq 1.34\sqrt{\beta_{\rm max}}. \tag{7.14}$$

Considering that, for the majority of realistic cold EoSs, the relation $0.24 \leq \beta_{\rm max} \leq 0.32$ holds, it has been concluded that $0.66 \leq \mathcal{K}_{\rm k} \leq 0.76$.

Figure 7.18(a) displays the Kerr parameter as a function of the gravitational mass for isothermal neutron stars. The effect of the temperature has a dramatic impact on the Kerr parameter. As the temperature increases, the Kerr parameter follows a slightly decreasing trajectory, except for $T = 60$ MeV, a behavior that is also shown in Figure 7.18(b), where the Kerr parameter is plotted as a function of temperature for constant gravitational masses. It has to be noted that after $T = 30$ MeV, the Kerr parameter creates a plate for each gravitational mass configuration.

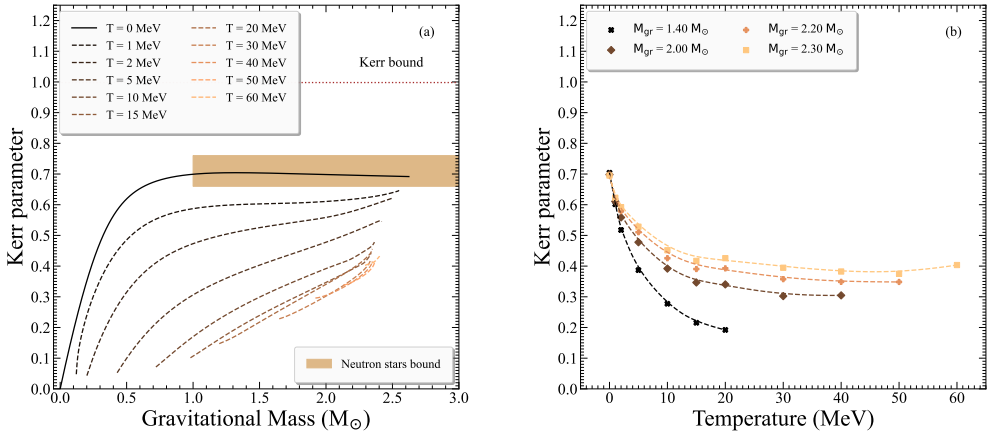

Figure 7.18: (a) Kerr parameter as a function of gravitational mass for temperatures in the range $[0, 60]$ MeV. The horizontal dotted line marks the Kerr bound for astrophysical Kerr black holes, $\mathcal{K}_{\rm B.H.} = 0.998$ (Thorne, 1974). The shaded region represents the limits for neutron stars from Equation (7.14). The cold configuration is presented by the solid line, while the hot configurations are presented by the dashed ones. (b) Kerr parameter as a function of temperature for constant gravitational mass. The crosses represent $M_{\rm gr} = 1.4\ M_\odot$, diamonds $M_{\rm gr} = 2\ M_\odot$, plus signs $M_{\rm gr} = 2.2\ M_\odot$, and squares $M_{\rm gr} = 2.3\ M_\odot$. The configuration corresponds to the mass-shedding limit.

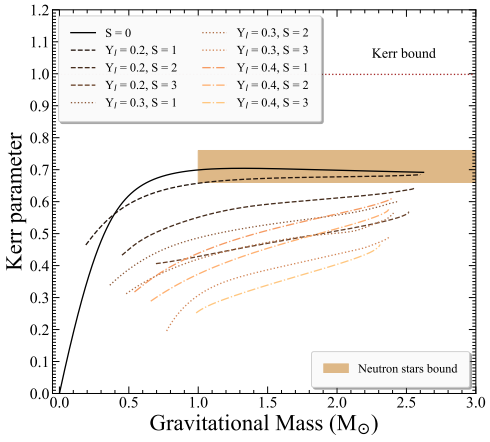

Figure 7.19: Kerr parameter as a function of gravitational mass for lepton fractions and entropies per baryon in the ranges $[0.2, 0.4]$ and $[1, 3]$ k_B, respectively. The horizontal dotted line marks the Kerr bound for astrophysical Kerr black holes, $\mathcal{K}_{\rm B.H.} = 0.998$ (Thorne, 1974). The shaded region represents the limits for neutron stars from Equation (7.14). The cold configuration is presented by the solid line. The configuration corresponds to the mass-shedding limit.

Figure 7.19 displays the Kerr parameter as a function of the gravitational mass for isentropic neutron stars. In this scenario, the interplay between the entropy per baryon and the lepton fraction leads to different behavior for the EoS. In particular, for a constant lepton fraction, as the entropy per baryon increases, the Kerr parameter decreases.

Having a limit for Kerr black holes (Thorne, 1974) and one for neutron stars from Equation (7.14) (see also Koliogiannis & Moustakidis (Koliogiannis and Moustakidis, 2020)), these values cannot be exceeded as the temperature in neutron stars increases. Therefore, the gravitational collapse of a hot, uniformly rotating neutron star, constrained to mass-energy and angular momentum conservation, cannot lead to a maximally rotating Kerr black hole. We note here that in the cold neutron star, for $M_{\rm gr} > 1\ M_\odot$, the Kerr parameter is almost independent on the gravitational mass. However, the Kerr parameter, in the isothermal and isentropic cases, is an increasing function of the gravitational mass. This unique interplay between the angular momentum and the gravitational mass is rather significant as the temperature in the interior of the neutron star increases.

Figure 7.20 display the angular velocity as a function of the ratio T/W for isothermal and isentropic neutron stars. Nonaxisymmetric peturbations are a way for a neutron star to emit gravitational waves. In neutron stars, the point that locates the nonaxisymmetric instability is defined via the ratio of rotational kinetic to gravitational binding energy T/W. Instabilities driven by gravitational radiation would set in at $T/W \sim 0.08$ for models with $M_{\rm gr} = 1.4\ M_\odot$ (Morsink et al., 1999). Figure 7.20 show that for sufficiently compact neutron stars (EoSs with $T \leq 1$ MeV for isothermal and EoSs with $Y_l = 0.2$ and $S = 1$ for isentropic), the nonaxisymmetric instability will set in before the mass-shedding limit is reached. The information that can be gained is that the maximum gravitational mass, as well as the angular velocity, for a specific EoS will be lowered. Furthermore, the increasing of temperature for isothermal neutron stars leads to the conclusion that for higher temperatures than $T = 2$ MeV, the instability never occurs. In the case of isentropic ones, the increasing of entropy per baryon avoids the instability.

From the relevant analysis on the quantities of this section, useful insight can be gained for the hot, rapidly rotating remnant (at least $T \geq 30$ MeV for isothermal EoSs, $S = 1$ and $Y_l = 0.2$ for isentropic ones) after the neutron star merger, which is a compact object with neutron star matter. The evolution of the remnant (immediately after the merger) will be one of the following

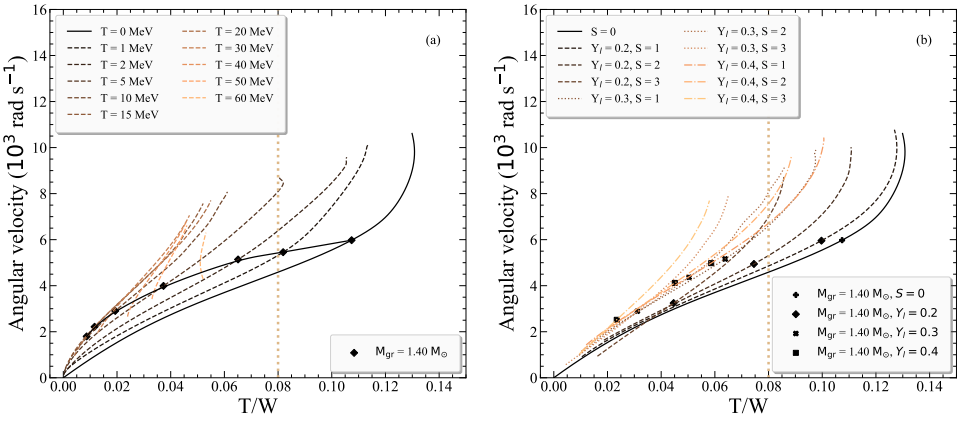

Figure 7.20: Angular velocity as a function of ratio of rotational kinetic to gravitational binding energy for (a) temperatures in the range $[0, 60]$ MeV and (b) lepton fractions and entropies per baryon in the ranges $[0.2, 0.4]$ and $[1, 3]$ k_B, respectively. Black diamonds represent the $M_{\rm gr} = 1.4\ M_\odot$ configuration. The vertical dotted line marks the critical value, $T/W = 0.08$, for gravitational radiation instabilities. The cold configuration is presented by the solid line, while the hot configurations are presented by the dashed ones. The configuration corresponds to the mass-shedding limit.

four cases: (a) the one that collapses directly into a black hole, (b) the one that initially forms a neutron star but collapses during disk accretion, (c) the one that does not collapse to a black hole until after the disk has fully accreted and the newly formed neutron star spins down, and (d) the one that, even after spin-down, remains a neutron star (Bernouzzi, 2020; Fryer et al., 2015). In the case where the two components of the binary neutron star system have nearly the same mass, the merged object exhibits fast differential rotation. Then, depending on the strength of the magnetic field, the object quickly goes into a uniform rotation. Moreover, neutrino cooling is responsible for the redistribution of the angular momentum. This process has a very short timescale (10-100 ms; (Bernouzzi, 2020; Fryer et al., 2015)). In general, the fate of the remnant in a neutron star merger is a complicated problem, where its solution combines the use of a reliable EoS and the development of corresponding simulations. Such studies are outside the scope of the present work.

Considering the maximum mass configuration at the mass-shedding limit, constraints on the hot, rapidly rotating remnant are possible through the dimensionless moment of inertia, the Kerr parameter, and the ratio T/W. In these cases, the compactness parameter is constraint to $\beta^{\rm iso}_{\rm rem} \leq 0.19$ and $\beta^{\rm ise}_{\rm rem} \leq 0.27$, while for the Kerr parameter, the maximum allowed value is at $\mathcal{K}^{\rm iso}_{\rm rem} = 0.42$ and $\mathcal{K}^{\rm ise}_{\rm rem} = 0.68$ (the superscripts "iso" and "ise", correspond to isothermal and isentropic profiles). Concerning the ratio T/W, the maximum value reaches up to $(T/W)^{\rm iso}_{\rm rem} = 0.05$ and $(T/W)^{\rm ise}_{\rm rem} = 0.127$. Considering all of the above, two different postulations, based on isothermal and isentropic neutron stars, can be made for the aftermath of a neutron star merger. In particular, in the isothermal case, it creates a lesser compact star than the cold neutron star with lower values of maximum gravitational mass and frequency, where, for the isentropic aftermath, the object is comparable to the cold one. In addition, while in the first case, the remnant that is formed is highly stable toward the dynamical instabilities, in the second one, it is unstable.

However, it has to be noted that this analysis concerns the uniform rotation. These values are expected to change if differential rotation is taken into account (Baumgarte et al., 2000; Morrison et al., 2004).

CHAPTER 8

Concluding remarks

In the first part of the research, different sequences of uniformly rotating neutron stars have been constructed for a large number of hadronic EoSs based on various theoretical nuclear models. This research performs an extended analysis of the bulk properties of neutron stars in correlation with the mass-shedding limit (Keplerian frequency). To be more specific, a calculation of their gravitational and rest mass, equatorial and polar radii, dimensionless angular momentum, angular velocity, moment of inertia, and eccentricity was considered. Relations between the Keplerian frequency and the bulk properties of neutron stars have been found and shown in the corresponding figures. These universal relations may impose constraints on the radius of a neutron star when its mass and Keplerian frequency is well fixed simultaneously. For example, this is the case of a millisecond pulsar (in a binary system) which acquired angular momentum by accretion and became a maximally rotating one with measured mass (Lattimer, 2017).

The dependence of moment of inertia, eccentricity, and Kerr parameter on the total gravitational mass at the Keplerian sequence is also obtained. In all cases, the EoSs presented similar behavior, so as a follow-up, the dependence of these parameters on the gravitational mass at the maximum mass configuration has been studied. We have concluded that moment of inertia and Kerr parameter can provide us with universal relations as a function of the gravitational mass at the maximum mass configuration for the Keplerian frequency. The effect of the eccentricity at the maximum mass configuration for the Keplerian frequency is also interesting on the corresponding gravitational mass, where eccentricity behaves as an EoS-independent property. Moreover, it has been found that the Kerr parameter reaches a maximum value at around 0.75 (stiffest EoS) for neutron stars. The importance of this result falls under the fact that the gravitational collapse of a uniformly rotating neutron star, constrained to mass-energy and angular momentum conservation, cannot lead to a naked singularity, or in other words, a maximally rotating Kerr black hole (Lo and Lin, 2011).

As a limiting case in our study, an EoS suitable to describe quark stars and one with the appearance of hyperons at high densities are presented. In the non-rotating case, the results are in good agreement with the hadronic EoSs, whereas in the maximally-rotating one, the difference from linearity is noticeable. Moreover, concerning the Kerr parameter, it is undeniable that its study on quark stars requires a different approach. Although a thorough study is needed, it can be seen that the values of the Kerr parameter of quark stars are significantly larger, not only from neutron stars but also from black holes. The latter can be helpful as an indicator to identify maximally-rotating quark stars (Lo and Lin, 2011). However, a detailed study must be done to acquire the EoS's possible effects on quark stars and their similarities with neutron stars. Concerning the hyperonic EoS, while its consistency with the 23 presented hadronic EoSs, allows it to be studied with them, a detailed study mainly based on hyperonic EoSs, would be more suitable.

Normal and supramassive sequences of constant rest mass for a specific EoS have been constructed. The corresponding figures present the stability and instability region of a neutron star. This is possible by plotting the evolution of a neutron star along the constant rest mass sequences. The extraordinary effect of supramassive ones is that they can inform us for the gravitational collapse to a black hole. The gravitational collapse of a rotating neutron star to a black hole creates a black hole with almost the same mass and angular momentum as the initial star (small amount of total mass and angular momentum carried away by gravitation radiation (Baiotti et al., 2005)), and therefore, the same Kerr parameter. Henceforth, this effect may provide an observable precursor to the gravitational collapse to a black hole. It is essential to add here that this effect will remain valid for all the EoSs studied in this research.

In order to imply possible constraints on the EoS, the LSRMS for the variety of the EoSs and the dimensionless moment of inertia have been constructed. In particular, they are presented in a figure of the angular velocity as a function of the Kerr parameter and of the dimensionless moment of inertia as a function of the compactness parameter, respectively. In both cases, a window is extracted where these properties can lie. In the first case, concerning the LSRMS, because this sequence is the one that corresponds to the maximum mass configuration at the non-rotating model, this is also the window where the EoS can lie, constraining simultaneously the angular velocity and spin parameter (or Kerr parameter) on neutron stars. In the second case, the formed window can help us constrain the moment of inertia and compactness parameter. The latter can impose strong constraints on the radius of neutron stars, which is one of the open problems in nuclear astrophysics.

Afterward, an update on the work of Lattimer and Prakash (Lattimer and Prakash, 2005) using EoSs consistent with the current observed limits of neutron star mass (Antoniadis et al., 2013; Arzoumanian et al., 2018; Cromartie et al., 2019; Demorest et al., 2010; Fonseca et al., 2016; Linares et al., 2018), is made. In this work, we propose the possible existence of an empirical solution, similar to the Tolman VII analytical solution, for neutron stars, using as a guide the maximally-rotating configuration to describe both the non-rotating and the maximally-rotating configuration. This solution can help define the ultimate density of cold baryonic matter by setting an absolute upper limit at the central energy density. The latter can be a valuable insight because it can inform us on the appearance of a phase transition in the star's interior and its leading to the back-bending phenomenon in pulsars.

Finally, the effects of the EoSs on the braking index of pulsars were studied. As an intrinsic property of a neutron star's structure, the braking index can inform us about the rate of change of angular velocity. Although we know it is prolonged, after the 70% of Keplerian angular velocity, the braking index is undergoing significant changes through the influence of the rest mass. This specific area, from 70% through the 100% of Keplerian angular velocity, may provide useful insights into the constitution of the dense nuclear matter.

In the second part of the research, a suggestion for a new method to constrain the neutron star EoS utilizing the stability condition introduced by Chandrasekhar (Chandrasekhar, 1964a) is presented. It has been found that the predicted critical adiabatic index, as a function of the compactness, for most EoSs considered here (although they differ considerably at their maximum masses and in how their masses are related to radii), satisfies a universal relation. In particular, exploiting these results leads to a model-independent expression for the critical adiabatic index as a function of compactness. The above finding may be added to the rest approximately EoS-independent relations (Breu and Rezzolla, 2016; Maselli et al., 2017; Ravenhall and Pethick, 1994; Silva and Yunes, 2017; Silva et al., 2016; Yagi and Yunes, 2013a,b, 2017; Yagi et al., 2014). These universal relations break degeneracies among astrophysical observations and lead to a variety of applications. We also found that observations of highly rotating neutron stars may help to impose valuable constraints on the EoSs, by using the dependence of maximum frequency on the compactness parameter corresponding to the maximum mass configuration of a non-rotating neutron star and, consequently, on the adiabatic index (instability limit). Additional theoretical

and observational measurements of the bulk neutron star properties close to the maximum-mass configuration will help to impose robust constraints on the neutron star EoS or, at least, to minimize the numbers of the proposed EoSs.

The last part of the research is focused on hot nuclear matter. Thermal pressure support in the isolated neutron stars and in the matter of merging (postmerger phase, remnant) must be better understood. In this study, we have attempted to gain insight into these issues by constructing and using a set of thermodynamically self-consistent EoSs (isothermal and isentropic) and constructing non-rotating and uniformly rotating axisymmetric equilibrium sequences. Such an approximation may be acceptable for a first-order study of hot, rapidly rotating remnants of neutron star mergers and protoneutron stars.

The nuclear model, used in the present work, provides some advantages compared to other models, mainly that (a) the thermal effects (both in isothermal and isentropic profiles) have been included in a self-consistent way, (b) the model is flexible enough to produce EoSs from very stiff to very soft by properly modifying the density dependence of the symmetry energy, (c) the parameterization of the model is also flexible to reproduce the properties of other microscopic calculations concerning both the SNM and the PNM, (d) the momentum dependence of the potential interaction (which is absent in the majority of the proposed models) is in accordance with the terrestrial studies and experiments of heavy-ion reactions for both low and high densities and temperatures, and (e) the model ensures the causal behavior of the EoS at high densities (even at densities higher than the ones of maximum mass configuration). Future work could extend the applications on both prior and postmerger processes, including thermal effects on tidal polarizability and other bulk properties, simulations of the evolution of the merger, and processes of protoneutron stars and supernovae.

The LS220 EoSs are employed for the low-density region ($n_b \leq 0.08$ fm^{-3}) of hot neutron stars. For each temperature or entropy per baryon, the lowest value of the baryon density is defined at 10^{-13} fm^{-3}. We found that the value of the mass is completely unaffected by the specific choice of the lowest value of the baryon density located at the star's surface. However, as expected, the uncertainty on the value of the radius is not negligible, especially for high values of temperature (or entropy per baryon), where estimations give rise to errors at a few percent, obviously depending on the temperature (see also (Raduta et al., 2020)).

Neutron stars can rotate extremely fast at the stage of being born or in the process of merging. While the Kepler frequency is an absolute limit on rotation, there are additional instabilities by which rotation may be limited if they occur at lower frequencies. However, this study is focused on the effect of thermal pressure. In particular, the thermal pressure becomes less important as we reach the neutron star's interior. However, this is not the case for the exterior region, where the bloat of the envelope takes place (Kaplan et al., 2014). Hence, while hot configurations have lower frequencies than cold ones in the case of isothermal neutron stars, isentropic neutron stars can possibly exceed the cold limit.

The baryon mass is the dominant quantity that manifests the thermal effects in neutron stars. The baryon mass that a neutron star can support depends sensitively on the temperature, as hot neutron stars lead to lower baryon masses. Connecting this property with the merger remnant, we study the supramassive limit. In the cold case, the baryon mass is $3.085\ M_\odot$, while a hot one at $T = 30$ MeV is $2.427\ M_\odot$ and one at $S = 1$ is $3.05\ M_\odot$. These limits correspond to merger components (assuming equal masses of components) of ~ 1.5425, ~ 1.2135, and $\sim 1.525\ M_\odot$ baryon masses, respectively. In particular, the immediate aftermath of GW170817 (Abbott et al., 2017) and GW190425 (Abbott et al., 2020a) had created a hot, rapidly rotating remnant possibly at its mass-shedding limit. Although it is most likely rotating differentially, the uniform rotation approach can provide useful insight into the EoS. In the case of GW170817, a remnant with a total mass of $\sim 2.7\ M_\odot$ has been created. In correlation with the MDI+APR1 EoS, with respect to baryon mass, while the uniform rotation of cold and isentropic neutron stars can support this remnant, isothermal ones might not. Moving on to the GW190425 event, the remnant of

$\sim 3.7\ M_\odot$ cannot exist supported only by uniform rotation. However, if differential rotation is added, leading to higher masses, hot neutron stars can probably support the remnant in both cases.

A very recent event, GW190814 (Abbott et al., 2020b), had a component with a mass of $\sim 2.6\ M_\odot$. Until this moment, it was believed to be either the lightest black hole or the most massive neutron star (Most et al., 2020). However, an approach in Most et al. (Most et al., 2020) suggests that this star was rapidly spinning with $\mathcal{K}$ in the range $[0.49, 0.68]$. Our study fully supports this scenario, as its mass and Kerr parameter coincides with the supramassive limit of the MDI+APR1 EoS in both cold catalyzed and isentropic matter with $S = 1$ and $Y_l = 0.2$. The latter may indicate that we have observed a neutron star close to or at its mass-shedding limit, being one step closer to measuring the Kepler frequency and imposing additional constraints on the EoS.

Moment of inertia is a quantity that informs us about the distribution of matter in the star as it continuously changes its angular velocity and loses angular momentum due to radiation. We observed that hot neutron stars, both isothermal and isentropic, have lower values than cold neutron stars. This effect originates from the unique interplay between the gravitational mass and the equatorial radius.

The Kerr parameter can be crucial as an indicator of the collapse to a black hole. Our relevant study shows that the maximum allowed value for this parameter is defined via the cold neutron star; thermal support indicates lower values of the Kerr parameter. The endpoint is that thermal support cannot lead a star to collapse into a maximally rotating Kerr black hole. On the other hand, the effect on the star is fascinating. Although in the cold case, after $\sim 1\ M_\odot$, the Kerr parameter is stabilized at a constant value, when the temperature is added, the Kerr parameter becomes an increasing function of the gravitational mass, leading to a maximum value.

The evidence related to gravitational collapse to a black hole and the existence of stable supramassive neutron stars is the ratio T/W. In the present study, the focus is turned on the case of gravitational collapse. Taking into account only the instabilities originating from gravitational radiation, the critical value of this ratio is ~ 0.08 for the $M_{\rm gr} = 1.4\ M_\odot$ configuration (Morsink et al., 1999). As in the case of the Kerr parameter, thermal support leads to lower values for the ratio T/W. Consequently, instabilities driven by gravitational radiation never occur in a hot, rapidly rotating neutron star. However, in the specific cases of $S = 1$ with $Y_l = 0.2$ and $T < 2$ MeV, the ratio T/W deviates from the limit toward higher values. In this case, the critical value of T/W may set the limit for the maximum gravitational mass and frequency. It is worth mentioning that studies related to the effect of the temperature on the Kerr parameter and the ratio T/W are scarce, and their existence may open a new window in neutron star studies.

An effective way to interpret the effects of temperature on the EoS is the evolutionary sequences of constant baryon mass. From these sequences, the interest is focused on the central baryon density and its dependence on the Kepler frequency. Specifically, for temperatures $T \geq 30$ MeV, a linear relation exists between these quantities, leading to a universal behavior and description for the central baryon density at the mass-shedding limit. Finally, it is worth mentioning that this relation defines the allowed region of the pair of the central baryon density and corresponding Kepler frequency for a rotating hot neutron star at its mass-shedding limit.

Future work should address the above analysis by considering rotating configurations based on differential laws in addition to the uniform rotation. Finally, the threshold mass, the hot, rapidly rotating remnant, and the possible phase transition region should be thoroughly investigated, as the LIGO and Virgo collaboration will provide us with more events of neutron star mergers.

In the near future, neutron star mergers and measurements of gravitational waves, besides being a powerful tool to study compact objects, such as neutron stars and black holes, will be able to provide us with the Keplerian frequency of these objects. In fact, although the remnant formed in the immediate aftermath of the GW170817 merger is believed to have been differentially rotating and not uniformly, it contains sufficient angular momentum to be near

its mass-shedding limit (Lattimer, 2019). The observational measurement of the Keplerian frequency, the temperature distribution in hot neutron stars, and the possible observable effects for the phase transition, along with the theoretical predictions, would provide severe constraints on the structure of neutron stars and especially on the high-density region of the EoS of nuclear matter.

NOTE

Parts of the dissertation have been published in the following three research papers, namely

- P. Koliogiannis and C. Moustakidis, Constraints on the equation of state from the stability condition of neutron stars. *Astrophysics and Space Science*, 364(3):52, Mar 2019 (Koliogiannis and Moustakidis, 2019)
- P.S. Koliogiannis and Ch.C. Moustakidis, Effects of the equation of state on the bulk properties of maximally rotating neutron stars. *Physical Review C*, 101:015805, Jan 2020 (Koliogiannis and Moustakidis, 2020)
- P.S. Koliogiannis and Ch.C. Moustakidis, Thermodynamical Description of Hot, Rapidly Rotating Neutron Stars, Protoneutron Stars, and Neutron Star Merger Remnants. *The Astrophysical Journal*, 912:69, May 2021 (Koliogiannis and Moustakidis, 2021)

CHAPTER 9

Appendix

9.1 Observed frequency limit

Lattimer and Prakash derived a relation in Ref. (Lattimer and Prakash, 2004), which gives the Keplerian frequency of a rotating neutron star, in terms of radius R and mass M of the corresponding non-rotating neutron star. The relation is

$$f_k = 1045 \left(\frac{M}{M_\odot}\right)^{1/2} \left(\frac{10\ \text{km}}{R}\right)^{3/2} \quad \text{(Hz)}, \tag{9.1}$$

which can be written as $f_k \approx 0.5701 f_S$, where f_S is the Keplerian rate for a rigid Newtonian sphere, and it is given by the equation

$$f_S = 1833 \left(\frac{M}{M_\odot}\right)^{1/2} \left(\frac{10\ \text{km}}{R}\right)^{3/2} \text{(Hz)}. \tag{9.2}$$

Following the work of Riahi et al. (Riahi et al., 2019), in order to find a more accurate relation, a relation have been constructed, based on a three order polynomial fit in terms of mass and radius of the corresponding non-rotating neutron star, given by the form

$$\begin{aligned} f_k/f_S &= 0.559 + 2.69 \left(\frac{M}{M_\odot}\right)\left(\frac{\text{km}}{R}\right) - 20.28 \left[\left(\frac{M}{M_\odot}\right)\left(\frac{\text{km}}{R}\right)\right]^2 \\ &+ 55.74 \left[\left(\frac{M}{M_\odot}\right)\left(\frac{\text{km}}{R}\right)\right]^3, \end{aligned} \tag{9.3}$$

with error up to 4%, in comparison with Lattimer and Prakash where the error was up to 30%.

For the observed frequency of the fastest known pulsar, PSR J1748-2446ad, which rotates with a frequency of 716 Hz, the relation (9.3) is obtained and its schematic presentation is presented in Figure 5.1.

9.2 Analytical solution - Tolman VII

The basic ingredients of the analytical solution - Tolman VII of Einstein's equations for a non-rotating spherical symmetric object, which in this case is a neutron star, are presented below.

The metric functions are defined as follows

$$e^{-\lambda} = 1 - \beta x^2 (5 - 3x^2), \quad e^{\nu} = \left(1 - \frac{5\beta}{3}\right) \cos^2 \phi, \tag{9.4}$$

where

$$x = \frac{r}{R}, \quad \phi = \frac{w_1 - w}{2} + \phi_1, \quad \phi_1 = \tan^{-1}\sqrt{\frac{\beta}{3(1-2\beta)}}$$

and

$$w = \ln\left(x^2 - \frac{5}{6} + \sqrt{\frac{e^{-\lambda}}{3\beta}}\right), \quad w_1 = \ln\left(\frac{1}{6} + \sqrt{\frac{1-2\beta}{3\beta}}\right).$$

The energy density and the pressure read as

$$\frac{\mathcal{E}(x)}{\mathcal{E}_c} = (1-x^2), \quad \mathcal{E}_c = \frac{15Mc^2}{8\pi R^3}, \tag{9.5}$$

$$\frac{P(x)}{\mathcal{E}_c} = \frac{2}{15}\sqrt{\frac{3e^{-\lambda}}{\beta}}\tan\phi - \frac{1}{3} + \frac{x^2}{5}. \tag{9.6}$$

There are some constraints related to the validity of the Tolman VII - analytical solution. In particular, the central pressure value becomes infinite for $\beta = 0.3862$, while the speed of sound remains less than that of light only for $\beta < 0.2698$ (Moustakidis, 2017). This solution leads to a stable configuration only for $\beta < 0.3428$ (Moustakidis, 2017).

The integrals' numerical integration related to the definition of $\langle\gamma\rangle$ and $\gamma_{\rm cr}$ can be easily performed. However, it is difficult to perceive the final results following this procedure. The former is accessible only in some approximated cases, e.g., Newtonian and post-Newtonian limits. In the following, we try to generalize the finding of Chandrasekhar (Chandrasekhar, 1964a) to even higher compactness values where the relativistic effects become important. The expression of the critical adiabatic index, with the help of the TOV equations (6.2), (6.3), using the trial function $\xi(r) = re^{\nu/2}$ (in order to be consistent with the pioneering work of Chandrasekhar (Chandrasekhar, 1964a)), and performing a Taylor expansion inside the integrals in each case, led to for the Uniform and the Tolman VII solution that is (see also (Merafina and Ruffini, 1989))

$$\gamma_{\rm cr}(\beta) = \frac{4}{3} + \frac{38}{42}\beta\mathcal{P}(\beta), \tag{9.7}$$

where, for the Uniform solution, $\mathcal{P}(\beta)$ takes the form:

$$\mathcal{P}_{\rm Uniform}(\beta) = 1 + 2.13\beta + 4.65\beta^2 + 10.22\beta^3 + \mathcal{O}(\beta^4), \tag{9.8}$$

and for the Tolman VII solution:

$$\mathcal{P}_{\rm Tolman}(\beta) = 1.19 + 2.93\beta + 7.34\beta^2 + 19.36\beta^3 + \mathcal{O}(\beta^4). \tag{9.9}$$

Obviously, the approximation (9.7)), using Equation (9.8), to a linear term, confirms the Chandrasekhar expression (6.12). The above expressions are good approximations for $\beta < 0.2$. However, they fail for higher values of β and, consequently, additional terms must be included. Specifically, $\gamma_{\rm cr}$ increases very fast for $\beta > 0.25$ due to the strong effects of general relativity.

9.3 Matching process

We employ a thermodynamic consistency method to match the two EoSs (those corresponding to the core and the crust) (Margaritis et al., 2021). In particular, the method is based on the $P(n)$ and n relation, where the baryon density n is considered an independent variable. A detailed presentation of the method is given in Ref. (Fortin et al., 2016). In the first region, which corresponds to the crust (hereafter denoted with the index 1), the relation $P_{\rm cr}(n) \equiv P_1(n)$

holds. In the second one, which corresponds to the core (hereafter denoted with the index 2), the relation $P_{\rm core}(n) \equiv P_2(n)$ holds. Moreover, it is considered that the matching region (mr) lies between the two densities n_1 and n_2, where $n_2 > n_1$, and the EoS is denoted as $P_{\rm mr}(n)$. For the matching region a linear dependence of $P_{\rm mr}(n)$ on n is employed and by considering the continuity relations, $P_{\rm mr}(n_1) = P_1(n_1)$ and $P_{\rm mr}(n_2) = P_2(n_2)$, the relation for the matching region is

$$P_{\rm mr}(n) = P_1(n_1) + \alpha(n - n_1), \tag{9.10}$$

where

$$\alpha = \frac{P_2(n_2) - P_1(n_1)}{n_2 - n_1}.$$

In the matching region and considering that $\mathcal{E}_{\rm mr}(n) = n\mu_{\rm mr}(n) - P_{\rm mr}(n)$ (where $\mu = d\mathcal{E}/dn$), the chemical potential $\mu_{\rm mr}(n)$ is given by

$$\mu_{\rm mr}(n) = \mu_1(n_1) + \int_{n_1}^{n} \frac{dP_{\rm mr}(n)}{n}, \tag{9.11}$$

where $\mu_1(n_1) = (P_1 + \mathcal{E}_1)/n_1$ and

$$\mu(n_2) = \mu_1(n_1) + \int_{n_1}^{n_2} \frac{dP_{\rm mr}(n)}{n}. \tag{9.12}$$

However, in general, $\mu_{\rm mr}(n_2) \neq \mu_2(n_2)$ (where $\mu_2 = (P_2 + \mathcal{E}_2)/n_2$). In this case, in order to satisfy the thermodynamically consistent EoS for $n > n_2$, the difference $\Delta\mu = \mu_{\rm mr}(n_2) - \mu_2(n_2)$ is defined.

Summarizing, the EoSs of each of the three regions, are specified as follows:

(1) For the crust ($n < n_1$) the EoS given in Ref. (Baym et al., 1971) is considered.

(2) For the matching region ($n_1 < n < n_2$) the pressure is given by Equation (9.10) and the energy density by $\mathcal{E}_{\rm mr}(n) = n\mu_{\rm mr}(n) - P_{\rm mr}(n)$ where

$$\mu_{\rm mr}(n) = \mu_1(n_1) + \alpha \ln\left(\frac{n}{n_1}\right), \tag{9.13}$$

and also

$$P_{\rm mr}(\mu) = P_1(n_1) + \alpha n_1 \left(e^{\frac{\mu-\mu_1}{\alpha}} - 1\right). \tag{9.14}$$

(3) For the core ($n > n_2$) the pressure $P_2(n)$ is employed while the corresponding energy density $\mathcal{E}_2(n)$ will be given by $\mathcal{E}_2(n) = \mathcal{E}(n) + n\Delta\mu$.

Finally, the speed of sound in the matching region will be given by the expression

$$\frac{v_{\rm s}}{c} \equiv \sqrt{\frac{\partial P}{\partial \mathcal{E}}} = \sqrt{\frac{\alpha}{\mu_1 + \alpha \ln(\frac{n}{n_1})}}. \tag{9.15}$$

In a part of the research, three different kinds of matching are being employed. In the first one, called TC_1, the selected densities n_1 and n_2 lie symmetrically among the critical density $n_{\rm t}$ within the crust and the core, respectively. In the second one, called TC_2, the density of the core n_2 is identified as the transition density and n_1 lies in the crust, while in the third case, called TC_3, the crust density n_1 is identified with $n_{\rm t}$ and n_2 lies in the core.

9.4 Numerical Code

The general relativistic models of neutron stars have been calculated by means of the code developed by Gourgoulhon et al. (Gourgoulhon et al., 1999), which relies on the multidomain spectral method of Bonazzola et al. (Bonazzola et al., 1998). This code is based on the C++ library LORENE (LOREBE (LORENE, 1998)), a software package for numerical relativity freely available under GNU license. The main characteristics of the numerical code are as follows.

- The EoS is a barotropic one, $P = P(n)$, in a tabular form that includes the baryon density, energy density, and pressure.
- The whole space is divided into three domains as follows:
  - D1, the interior of the star;
  - D2, an intermediate domain whose inner boundary is the surface of the star and outer boundary is a sphere located at $r = 2r_{\text{eq}}$ (where r_{eq} is the equatorial coordinate radius of the star); and
  - D3, the external domain whose inner boundary is the outer boundary of D2 and that extends up to infinity.
- The mapping adaptation is using one domain.
- The points in θ, ϕ, and r are $N_\theta = 1 \times 25$, $N_\phi = 1 \times 1$, and $N_r = 3 \times 49$, respectively.
- The initial frequency of the rotating star is 100 Hz and, in low-frequency areas (< 100 Hz), $10/50$ Hz.
- The global numerical error is evaluated by means of the virial identities, GRV2 and GRV3, where the latter is a relativistic generalization of the classical virial theorem. For the configurations presented in this research, the relative errors are of order 10^{-6}.

List of Figures

List of Tables

CHAPTER 10

Bibliography

B. P. Abbott et al. Gw170817: Observation of gravitational waves from a binary neutron star inspiral. *Physical Review Letters*, 119:161101, Oct 2017. doi:10.1103/PhysRevLett.119.161101. URL https://link.aps.org/doi/10.1103/PhysRevLett.119.161101.

B. P. Abbott et al. GW190425: Observation of a compact binary coalescence with total mass $\sim$ 3.4 M $\odot$. *The Astrophysical Journal*, 892(1):L3, mar 2020a. doi:10.3847/2041-8213/ab75f5. URL https://doi.org/10.3847%2F2041-8213%2Fab75f5.

R. Abbott et al. GW190814: Gravitational waves from the coalescence of a 23 solar mass black hole with a 2.6 solar mass compact object. *The Astrophysical Journal*, 896(2):L44, jun 2020b. doi:10.3847/2041-8213/ab960f. URL https://doi.org/10.3847%2F2041-8213%2Fab960f.

M. A. Abramowicz and R. V. Wagoner. Slowly rotating, relativistic stars. *The Astrophysical Journal*, 226:1063–1078, Dec. 1978. doi:10.1086/156683.

B. K. Agrawal, R. Kumar, and S. K. Dhiman. Correlations in the properties of static and rapidly rotating compact stars. *Physical Review D*, 77:087301, Apr 2008. doi:10.1103/PhysRevD.77.087301. URL https://link.aps.org/doi/10.1103/PhysRevD.77.087301.

A. Akmal, V. R. Pandharipande, and D. G. Ravenhall. Equation of state of nucleon matter and neutron star structure. *Physical Review C*, 58:1804–1828, Sep 1998. doi:10.1103/PhysRevC.58.1804. URL https://link.aps.org/doi/10.1103/PhysRevC.58.1804.

J. Alsing, H. O. Silva, and E. Berti. Evidence for a maximum mass cut-off in the neutron star mass distribution and constraints on the equation of state. *Monthly Notices of the Royal Astronomical Society*, 478(1):1377–1391, 04 2018. ISSN 0035-8711. doi:10.1093/mnras/sty1065. URL https://doi.org/10.1093/mnras/sty1065.

E. Annala, T. Gorda, A. Kurkela, J. Nättilä, and A. Vuorinen. Evidence for quark-matter cores in massive neutron stars. *Nature Physics*, 16:907–910, september 2020. ISSN 1745-2481. doi:10.1038/s41567-020-0914-9. URL https://doi.org/10.1038/s41567-020-0914-9.

J. Antoniadis, P. Freire, N. Wex, T. Tauris, R. Lynch, et al. A massive pulsar in a compact relativistic binary. *Science*, 340:1233232, 2013. doi:10.1126/science.1233232.

Z. Arzoumanian, S. Bogdanov, J. Cordes, K. Gendreau, D. Lai, J. Lattimer, B. Link, A. Lommen, C. Miller, P. Ray, R. Rutledge, T. Strohmayer, C. Wilson-Hodge, and K. Wood. X-ray timing of neutron stars, astrophysical probes of extreme physics, 2009. URL https://arxiv.org/abs/0902.3264.

Z. Arzoumanian, A. Brazier, S. Burke-Spolaor, S. Chamberlin, S. Chatterjee, et al. The NANOGrav 11-year Data Set: High-precision Timing of 45 Millisecond Pulsars. *The Astrophysical Journal*, 235:37, 2018. doi:10.3847/1538-4365/aab5b0.

W. Baade and F. Zwicky. Cosmic rays from super-novae. *Proceedings of the National Academy of Sciences*, 20:259–263, May 1934. doi:10.1073/pnas.20.5.25. URL https://www.pnas.org/doi/10.1073/pnas.20.5.259.

D. C. Backer, S. R. Kulkarni, C. Heiles, M. M. Davis, and W. M. Goss. A millisecond pulsar. *Nature*, 300(5893):615–618, Dec 1982. ISSN 1476-4687. doi:10.1038/300615a0. URL https://doi.org/10.1038/300615a0.

P. Bagchi, A. Das, B. Layek, and A. M. Srivastava. Effects of phase transition induced density fluctuations on pulsar dynamics. *Physics Letters B*, 747:120–124, 2015. ISSN 0370-2693. doi:https://doi.org/10.1016/j.physletb.2015.05.055. URL https://www.sciencedirect.com/science/article/pii/S0370269315003925.

L. Baiotti, I. Hawke, L. Rezzolla, and E. Schnetter. Gravitational-wave emission from rotating gravitational collapse in three dimensions. *Physical Review Letters*, 94:131101, Apr 2005. doi:10.1103/PhysRevLett.94.131101. URL https://link.aps.org/doi/10.1103/PhysRevLett.94.131101.

S. Balberg and S. L. Shapiro. The properties of matter in white dwarfs and neutron stars, 2000. URL https://arxiv.org/abs/astro-ph/0004317.

M. Baldo and G. Burgio. The nuclear symmetry energy. *Progress in Particle and Nuclear Physics*, 91:203 – 258, 2016. ISSN 0146-6410. doi:https://doi.org/10.1016/j.ppnp.2016.06.006. URL http://www.sciencedirect.com/science/article/pii/S0146641016300254.

J. M. Bardeen, K. S. Thorne, and D. W. Meltzer. A Catalogue of Methods for Studying the Normal Modes of Radial Pulsation of General-Relativistic Stellar Models. *The Astrophysical Journal*, 145:505, Aug. 1966. doi:10.1086/148791.

N. D. Batra, K. P. Nunna, and S. Banik. Properties of rapidly rotating hot neutron stars with antikaon condensates at constant entropy per baryon. *Physical Review C*, 98:035801, Sep 2018. doi:10.1103/PhysRevC.98.035801. URL https://link.aps.org/doi/10.1103/PhysRevC.98.035801.

T. W. Baumgarte, S. L. Shapiro, and M. Shibata. On the maximum mass of differentially rotating neutron stars. *The Astrophysical Journal*, 528(1):L29–L32, jan 2000. doi:10.1086/312425. URL https://doi.org/10.1086%2F312425.

A. Bauswein, H.-T. Janka, and R. Oechslin. Testing approximations of thermal effects in neutron star merger simulations. *Physical Review D*, 82:084043, Oct 2010. doi:10.1103/PhysRevD.82.084043. URL https://link.aps.org/doi/10.1103/PhysRevD.82.084043.

A. Bauswein, O. Just, H.-T. Janka, and N. Stergioulas. Neutron-star radius constraints from gw170817 and future detections. *The Astrophysical Journal Letters*, 850(2):L34, nov 2017. doi:10.3847/2041-8213/aa9994. URL https://dx.doi.org/10.3847/2041-8213/aa9994.

G. Baym, C. Pethick, and D. Pines. Superfluidity in neutron stars. *Nature*, 224(5220):673–674, Nov 1969. ISSN 1476-4687. doi:10.1038/224673a0. URL https://doi.org/10.1038/224673a0.

G. Baym, C. Pethick, and P. Sutherland. The ground state of matter at high densities: Equation of state and stellar models. *The Astrophysical Journal*, 170:299–317, dec 1971. doi:10.1086/151216.

G. Baym, T. Hatsuda, T. Kojo, P. D. Powell, Y. Song, and T. Takatsuka. From hadrons to quarks in neutron stars: a review. *Reports on Progress in Physics,*, 81(5):056902, mar 2018. doi:10.1088/1361-6633/aaae14. URL https://doi.org/10.1088%2F1361-6633%2Faaae14.

M. Bejger, T. Bulik, and P. Haensel. Constraints on the dense matter equation of state from the measurements of PSR J0737-3039A moment of inertia and PSR J0751+1807 mass. *Monthly Notices of the Royal Astronomical Society*, 364(2):635–639, 12 2005. ISSN 0035-8711. doi:10.1111/j.1365-2966.2005.09575.x. URL https://doi.org/10.1111/j.1365-2966.2005.09575.x.

M. Bejger, D. Blaschke, P. Haensel, J. L. Zdunik, and M. Fortin. Consequences of a strong phase transition in the dense matter equation of state for the rotational evolution of neutron stars. *Astronomy and Astrophysics*, 600:A39, 2017. doi:10.1051/0004-6361/201629580. URL https://doi.org/10.1051/0004-6361/201629580.

O. Benhar, V. Ferrari, L. Gualtieri, and S. Marassi. Perturbative approach to the structure of rapidly rotating neutron stars. *Physical Review D*, 72:044028, Aug 2005. doi:10.1103/PhysRevD.72.044028. URL https://link.aps.org/doi/10.1103/PhysRevD.72.044028.

S. Bernouzzi. Neutron star merger remnants. *General Relativity and Gravitation*, 52:108, apr 2020. doi:https://doi.org/10.1007/s10714-020-02752-5.

G. Bertsch and S. D. Gupta. A guide to microscopic models for intermediate energy heavy ion collisions. *Physics Reports*, 160(4):189 – 233, 1988. ISSN 0370-1573. doi:https://doi.org/10.1016/0370-1573(88)90170-6. URL http://www.sciencedirect.com/science/article/pii/0370157388901706.

H. Bethe, G. Brown, J. Applegate, and J. Lattimer. Equation of state in the gravitational collapse of stars. *Nuclear Physics A*, 324(2):487 – 533, 1979. ISSN 0375-9474. doi:https://doi.org/10.1016/0375-9474(79)90596-7. URL http://www.sciencedirect.com/science/article/pii/0375947479905967.

S. I. Blinnikov, I. D. Novikov, T. V. Perevodchikova, and A. G. Polnarev. Exploding Neutron Stars in Close Binaries. *Soviet Astronomy Letters*, 10:177–179, Apr. 1984. doi:10.48550/arXiv.1808.05287.

S. A. Bludman. Stability of General-Relativistic Polytropes. *The Astrophysical Journal*, 183:637–648, July 1973a. doi:10.1086/152253.

S. A. Bludman. Simple Calculation of Critical Parameters of Neutron Stars. *The Astrophysical Journal*, 183:649–656, July 1973b. doi:10.1086/152254.

I. Bombaci and D. Logoteta. Equation of state of dense nuclear matter and neutron star structure from nuclear chiral interactions. *Astronomy and Astrophysics*, 609:A128, 2018. doi:10.1051/0004-6361/201731604. URL https://doi.org/10.1051/0004-6361/201731604.

S. Bonazzola, E. Gourgoulhon, and J.-A. Marck. Numerical approach for high precision 3d relativistic star models. *Physical Review D*, 58:104020, Oct 1998. doi:10.1103/PhysRevD.58.104020. URL https://link.aps.org/doi/10.1103/PhysRevD.58.104020.

R. L. Bowers, A. M. Gleeson, and R. D. Pedigo. Relativistic superdense matter in cold systems: Applications. *Physical Review D*, 12:3056–3068, Nov 1975. doi:10.1103/PhysRevD.12.3056. URL https://link.aps.org/doi/10.1103/PhysRevD.12.3056.

C. Breu and L. Rezzolla. Maximum mass, moment of inertia and compactness of relativistic stars. *Monthly Notices of the Royal Astronomical Society*, 459(1):646–656, 03 2016. ISSN 0035-8711. doi:10.1093/mnras/stw575. URL https://doi.org/10.1093/mnras/stw575.

G. Brown, H. Bethe, and G. Baym. Supernova theory. *Nuclear Physics A*, 375(3):481 – 532, 1982. ISSN 0375-9474. doi:https://doi.org/10.1016/0375-9474(82)90025-2. URL http://www.sciencedirect.com/science/article/pii/0375947482900252.

H. A. Buchdahl. General relativistic fluid spheres. *Physical Review*, 116:1027–1034, Nov 1959a. doi:10.1103/PhysRev.116.1027. URL https://link.aps.org/doi/10.1103/PhysRev.116.1027.

H. A. Buchdahl. General-relativistic fluid spheres. iii. a static gaseous model. *The Astrophysical Journal*, 147:310, Jan 1959b. doi:10.1086/149001. URL https://ui.adsabs.harvard.edu/abs/1967ApJ...147..310B/abstract.

G. F. Burgio and H.-J. Schulze. The maximum and minimum mass of protoneutron stars in the brueckner theory. *The Astrophysical Journal*, 518:A17, 2010. doi:10.1051/0004-6361/201014308. URL https://doi.org/10.1051/0004-6361/201014308.

G. F. Burgio, M. Baldo, O. E. Nicotra, and H.-J. Schulze. A microscopic equation of state for protoneutron stars. *The Astrophysical Journal Supplement Series*, 308(1):387–394, Apr 2007. ISSN 1572-946X. doi:10.1007/s10509-007-9360-8. URL https://doi.org/10.1007/s10509-007-9360-8.

E. Chabanat, P. Bonche, P. Haensel, J. Meyer, and R. Schaeffer. A skyrme parametrization from subnuclear to neutron star densities. *Nuclear Physics A*, 627(4):710–746, 1997. ISSN 0375-9474. doi:https://doi.org/10.1016/S0375-9474(97)00596-4. URL https://www.sciencedirect.com/science/article/pii/S0375947497005964.

S. Chakrabarti, T. Delsate, N. Gürlebeck, and J. Steinhoff. $I-Q$ relation for rapidly rotating neutron stars. *Physical Review Letters*, 112:201102, May 2014a. doi:10.1103/PhysRevLett.112.201102. URL https://link.aps.org/doi/10.1103/PhysRevLett.112.201102.

S. Chakrabarti, T. Delsate, N. Gürlebeck, and J. Steinhoff. $i-q$ relation for rapidly rotating neutron stars. *Physical Review Letters*, 112:201102, May 2014b. doi:10.1103/PhysRevLett.112.201102. URL https://link.aps.org/doi/10.1103/PhysRevLett.112.201102.

R. Chan, L. Herrera, and N. O. Santos. Dynamical instability for shearing viscous collapse. *Monthly Notices of the Royal Astronomical Society*, 267(3):637–646, 04 1994. ISSN 0035-8711. doi:10.1093/mnras/267.3.637. URL https://doi.org/10.1093/mnras/267.3.637.

S. Chandrasekhar. The dynamical instability of gaseous masses approaching the schwarzschild limit in general relativity. *The Astrophysical Journal*, 140:417, Aug 1964a. doi:10.1086/147938. URL https://ui.adsabs.harvard.edu/abs/1964ApJ...140..417C/abstract.

S. Chandrasekhar. Dynamical instability of gaseous masses approaching the schwarzschild limit in general relativity. *Physical Review Letters*, 12:114–116, Jan 1964b. doi:10.1103/PhysRevLett.12.114. URL https://link.aps.org/doi/10.1103/PhysRevLett.12.114.

D. Chatterjee and I. Vidaña. Do hyperons exist in the interior of neutron stars? *The European Physical Journal A*, 52:29, feb 2016. doi:10.1140/epja/i2016-16029-x. URL https://doi.org/10.1140/epja/i2016-16029-x.

L.-W. Chen, C. M. Ko, and B.-A. Li. Determination of the stiffness of the nuclear symmetry energy from isospin diffusion. *Physical Review Letters*, 94:032701, Jan 2005. doi:10.1103/PhysRevLett.94.032701. URL https://link.aps.org/doi/10.1103/PhysRevLett.94.032701.

W.-C. Chen and J. Piekarewicz. Compactness of neutron stars. *Physical Review Letters*, 115: 161101, Oct 2015. doi:10.1103/PhysRevLett.115.161101. URL https://link.aps.org/doi/10.1103/PhysRevLett.115.161101.

F. Cipolletta, C. Cherubini, S. Filippi, J. A. Rueda, and R. Ruffini. Fast rotating neutron stars with realistic nuclear matter equation of state. *Physical Review D*, 92:023007, Jul 2015. doi:10.1103/PhysRevD.92.023007. URL https://link.aps.org/doi/10.1103/PhysRevD.92.023007.

F. Cipolletta, C. Cherubini, S. Filippi, J. A. Rueda, and R. Ruffini. Last stable orbit around rapidly rotating neutron stars. *Physical Review D*, 96:024046, Jul 2017. doi:10.1103/PhysRevD.96.024046. URL https://link.aps.org/doi/10.1103/PhysRevD.96.024046.

S. A. Colgate and R. H. White. The Hydrodynamic Behavior of Supernovae Explosions. *The Astrophysical Journal*, 143:626, Mar. 1966. doi:10.1086/148549.

M. Colpi, S. L. Shapiro, and S. A. Teukolsky. Exploding neutron stars near the minimum mass. *The Astrophysical Journal*, 339(4):318–338, apr 1989. doi:10.1086/167299.

M. Colpi, S. L. Shapiro, and S. A. Teukolsky. Explosion of a Rotating Neutron Star near the Minimum Mass. *The Astrophysical Journal*, 369:422, Mar. 1991. doi:10.1086/169771.

C. Constantinou, B. Muccioli, M. Prakash, and J. M. Lattimer. Thermal properties of supernova matter: The bulk homogeneous phase. *Physical Review C*, 89:065802, Jun 2014. doi:10.1103/PhysRevC.89.065802. URL https://link.aps.org/doi/10.1103/PhysRevC.89.065802.

C. Constantinou, B. Muccioli, M. Prakash, and J. M. Lattimer. Thermal properties of hot and dense matter with finite range interactions. *Physical Review C*, 92:025801, Aug 2015. doi:10.1103/PhysRevC.92.025801. URL https://link.aps.org/doi/10.1103/PhysRevC.92.025801.

G. B. Cook, S. L. Shapiro, and S. A. Teukolsky. Spin-up of a rapidly rotating star by angular momentum loss: Effects of general relativity. *The Astrophysical Journal*, 398:203, Oct 1992. doi:10.1086/171849. URL https://ui.adsabs.harvard.edu/abs/1992ApJ...398..203C/abstract.

G. B. Cook, S. L. Shapiro, and S. A. Teukolsky. Rapidly rotating polytropes in general relativity. *The Astrophysical Journal*, 422:227, Feb 1994a. doi:10.1086/173721. URL https://ui.adsabs.harvard.edu/abs/1994ApJ...422..227C/abstract.

G. B. Cook, S. L. Shapiro, and S. A. Teukolsky. Recycling pulsars to millisecond periods in general relativity. *The Astrophysical Journal Letters*, 423:L117, Mar 1994b. doi:10.1086/187250. URL https://ui.adsabs.harvard.edu/abs/1994ApJ...423L.117C/abstract.

G. B. Cook, S. L. Shapiro, and S. A. Teukolsky. Rapidly rotating neutron stars in general relativity: Realistic equations of state. *The Astrophysical Journal*, 424:823, Apr 1994c. doi:10.1086/173934. URL https://ui.adsabs.harvard.edu/abs/1994ApJ...424..823C/abstract.

H. Cromartie, E. Fonseca, S. Ransom, P. B. Demorest, Z. Arzoumanian, et al. Relativistic Shapiro delay measurements of an extremely massive millisecond pulsar. *Nature Astronomy*, 2019. doi:10.1038/s41550-019-0880-2.

L. P. Csernai, G. Fai, C. Gale, and E. Osnes. Nuclear equation of state with momentum-dependent interactions. *Physical Review C*, 46:736–747, Aug 1992. doi:10.1103/PhysRevC.46.736. URL https://link.aps.org/doi/10.1103/PhysRevC.46.736.

A. da Silva Schneider, E. O'Connor, E. Granqvist, A. Betranhandy, and S. M. Couch. Equation of state and progenitor dependence of stellar-mass black hole formation. *The Astrophysical Journal*, 894(1):4, apr 2020. doi:10.3847/1538-4357/ab8308. URL https://doi.org/10.3847/1538-4357/ab8308.

E. N. E. v. Dalen, C. Fuchs, and A. Faessler. Momentum, density, and isospin dependence of symmetric and asymmetric nuclear matter properties. *Physical Review C*, 72:065803, Dec 2005. doi:10.1103/PhysRevC.72.065803. URL https://link.aps.org/doi/10.1103/PhysRevC.72.065803.

C. Das, R. Sahu, and A. Mishra. Equation of state of supernova matter. *Physical Review C*, 75:015807, Jan 2007. doi:10.1103/PhysRevC.75.015807. URL https://link.aps.org/doi/10.1103/PhysRevC.75.015807.

C. B. Das, S. Das Gupta, C. Gale, and B.-A. Li. Momentum dependence of symmetry potential in asymmetric nuclear matter for transport model calculations. *Physical Review C*, 67:034611, Mar 2003. doi:10.1103/PhysRevC.67.034611. URL https://link.aps.org/doi/10.1103/PhysRevC.67.034611.

M. Delgaty and K. Lake. Physical acceptability of isolated, static, spherically symmetric, perfect fluid solutions of einstein's equations. *Computer Physics Communications*, 115(2):395–415, 1998. ISSN 0010-4655. doi:https://doi.org/10.1016/S0010-4655(98)00130-1. URL https://www.sciencedirect.com/science/article/pii/S0010465598001301. Computer Algebra in Physics Research.

P. Demorest, T. Pennucci, S. Ransom, et al. A two-solar-mass neutron star measured using shapiro delay. *Nature*, 467:1081–1083, oct 2010. doi:https://doi.org/10.1038/nature09466.

S. K. Dhiman, R. Kumar, and B. K. Agrawal. Nonrotating and rotating neutron stars in the extended field theoretical model. *Physical Review C*, 76:045801, Oct 2007. doi:10.1103/PhysRevC.76.045801. URL https://link.aps.org/doi/10.1103/PhysRevC.76.045801.

D. D. Doneva, S. S. Yazadjiev, N. Stergioulas, and K. D. Kokkotas. Rapidly rotating neutron stars in scalar-tensor theories of gravity. *Physical Review D*, 88:084060, Oct 2013. doi:10.1103/PhysRevD.88.084060. URL https://link.aps.org/doi/10.1103/PhysRevD.88.084060.

F. Douchin and P. Haensel. A unified equation of state of dense matter and neutron star structure. *Astronomy and Astrophysics*, 380(1):151–167, 2001. doi:10.1051/0004-6361:20011402. URL https://doi.org/10.1051/0004-6361:20011402.

edited by W. Becker. *Neutron Stars and Pulsars (Astrophysics and Space Science Library Vol. 357)*. Springer, Berlin, 2009.

M. Farine, J. Pearson, and F. Tondeur. Nuclear-matter incompressibility from fits of generalized skyrme force to breathing-mode energies. *Nuclear Physics A*, 615(2):135–161, 1997. ISSN 0375-9474. doi:https://doi.org/10.1016/S0375-9474(96)00453-8. URL https://www.sciencedirect.com/science/article/pii/S0375947496004538.

A. L. Fetter and J. D. Walecka. *Quantum Theory of Many-Particle Systems*. Dover,Mineola,New York, 2003.

R. P. Feynman, N. Metropolis, and E. Teller. Equations of state of elements based on the generalized fermi-thomas theory. *Physical Review*, 75:1561–1573, May 1949. doi:10.1103/PhysRev.75.1561. URL https://link.aps.org/doi/10.1103/PhysRev.75.1561.

A. Figura, J.-J. Lu, G. F. Burgio, Z.-H. Li, and H.-J. Schulze. Hybrid equation of state approach in binary neutron-star merger simulations. *Physical Review D*, 102:043006, Aug 2020. doi:10.1103/PhysRevD.102.043006. URL https://link.aps.org/doi/10.1103/PhysRevD.102.043006.

E. Fonseca, T. T. Pennucci, J. A. Ellis, I. H. Stairs, D. J. Nice, S. M. Ransom, P. B. Demorest, Z. Arzoumanian, K. Crowter, T. Dolch, R. D. Ferdman, M. E. Gonzalez, G. Jones, M. L. Jones, M. T. Lam, L. Levin, M. A. McLaughlin, K. Stovall, J. K. Swiggum, and W. Zhu. The NANOGRAV nine-year data set: mass and geometric measurements of binary millisecond pulsars. *The Astrophysical Journal*, 832(2):167, dec 2016. doi:10.3847/0004-637x/832/2/167. URL https://doi.org/10.3847%2F0004-637x%2F832%2F2%2F167.

M. Fortin, C. Providência, A. R. Raduta, F. Gulminelli, J. L. Zdunik, P. Haensel, and M. Bejger. Neutron star radii and crusts: Uncertainties and unified equations of state. *Physical Review C*, 94:035804, Sep 2016. doi:10.1103/PhysRevC.94.035804. URL https://link.aps.org/doi/10.1103/PhysRevC.94.035804.

M. Fortin, G. Taranto, G. F. Burgio, P. Haensel, H.-J. Schulze, and J. L. Zdunik. Thermal states of neutron stars with a consistent model of interior. *Monthly Notices of the Royal Astronomical Society*, 475(4):5010–5022, 01 2018. ISSN 0035-8711. doi:10.1093/mnras/sty147. URL https://doi.org/10.1093/mnras/sty147.

J. L. Friedman and J. R. Ipser. On the maximum mass of a uniformly rotating neutron star. *The Astrophysical Journal*, 314:594, mar 1987. doi:10.1086/165088.

J. L. Friedman and N. Stergioulas. *Rotating Relativistic Stars*. Cambridge Monographs on Mathematical Physics. Cambridge University Press, 2013. doi:10.1017/CBO9780511977596.

J. L. Friedman, J. R. Ipser, and L. Parker. Rapidly rotating neutron star models. *The Astrophysical Journal*, 304:115, may 1986. doi:10.1086/164149.

J. L. Friedman, J. R. Ipser, and R. D. Sorkin. Turning point method for axisymmetric stability of rotating relativistic stars. *The Astrophysical Journal*, 325:722, feb 1988. doi:10.1086/166043.

J. L. Friedman, J. R. Ipser, and L. Parker. Implications of a half-millisecond pulsar. *Physical Review Letters*, 62:3015–3019, Jun 1989. doi:10.1103/PhysRevLett.62.3015. URL https://link.aps.org/doi/10.1103/PhysRevLett.62.3015.

C. L. Fryer, K. Belczynski, E. Ramirez-Ruiz, S. Rosswog, G. Shen, and A. W. Steiner. The Fate Of The Compact Remnant In Neutron Star Mergers. *The Astrophysical Journal*, 812 (1):24, oct 2015. doi:10.1088/0004-637x/812/1/24. URL https://doi.org/10.1088%2F0004-637x%2F812%2F1%2F24.

E. Gaertig and K. D. Kokkotas. Relativistic g-modes in rapidly rotating neutron stars. *Physical Review D*, 80:064026, Sep 2009. doi:10.1103/PhysRevD.80.064026. URL https://link.aps.org/doi/10.1103/PhysRevD.80.064026.

T. Gaitanos and M. Kaskulov. Momentum dependent mean-field dynamics of compressed nuclear matter and neutron stars. *Nuclear Physics A*, 899:133–169, 2013. ISSN 0375-9474. doi:https://doi.org/10.1016/j.nuclphysa.2013.01.002. URL https://www.sciencedirect.com/science/article/pii/S0375947413000067.

T. Gaitanos and M. Kaskulov. Toward relativistic mean-field description of $\bar{N}$–nucleus reactions. *Nuclear Physics A*, 940:181–193, 2015. ISSN 0375-9474. doi:https://doi.org/10.1016/j.nuclphysa.2015.04.006. URL https://www.sciencedirect.com/science/article/pii/S0375947415001025.

C. Gale, G. Bertsch, and S. Das Gupta. Heavy-ion collision theory with momentum-dependent interactions. *Physical Review C*, 35:1666–1671, May 1987. doi:10.1103/PhysRevC.35.1666. URL https://link.aps.org/doi/10.1103/PhysRevC.35.1666.

C. Gale, G. M. Welke, M. Prakash, S. J. Lee, and S. Das Gupta. Transverse momenta, nuclear equation of state, and momentum-dependent interactions in heavy-ion collisions. *Physical Review C*, 41:1545–1552, Apr 1990. doi:10.1103/PhysRevC.41.1545. URL https://link.aps.org/doi/10.1103/PhysRevC.41.1545.

R. Giacconi, H. Gursky, E. Kellogg, E. Schreier, and H. Tananbaum. Discovery of Periodic X-Ray Pulsations in Centaurus X-3 from UHURU. *The Astrophysical Journal*, 167:L67, July 1971. doi:10.1086/180762.

E. N. Glass and A. Harpaz. The stability of relativistic gas spheres. *Monthly Notices of the Royal Astronomical Society*, 202(1):159–171, 01 1983. ISSN 0035-8711. doi:10.1093/mnras/202.1.159. URL https://doi.org/10.1093/mnras/202.1.159.

N. Glendenning. *Compact Stars: Nuclear Physics, Particle Physics, and General Relativity*. Springer, Berlin, 2000.

N. K. Glendenning. Limiting rotational period of neutron stars. *Physical Review D*, 46:4161–4168, Nov 1992. doi:10.1103/PhysRevD.46.4161. URL https://link.aps.org/doi/10.1103/PhysRevD.46.4161.

N. K. Glendenning. Pulsar signal of deconfinement. *Nuclear Physics A*, 638(1):239c–248c, 1998. ISSN 0375-9474. doi:https://doi.org/10.1016/S0375-9474(98)00355-8. URL https://www.sciencedirect.com/science/article/pii/S0375947498003558. Quark Matter '97.

N. K. Glendenning and F. Weber. Impact of frame dragging on the kepler frequency of relativistic stars. *Physical Review D*, 50:3836–3841, Sep 1994. doi:10.1103/PhysRevD.50.3836. URL https://link.aps.org/doi/10.1103/PhysRevD.50.3836.

N. K. Glendenning, S. Pei, and F. Weber. Signal of quark deconfinement in the timing structure of pulsar spin-down. *Physical Review Letters*, 79:1603–1606, Sep 1997. doi:10.1103/PhysRevLett.79.1603. URL https://link.aps.org/doi/10.1103/PhysRevLett.79.1603.

D. L. Goodstein. *States of Matter*. Dove,New York, 1985.

E. Gourgoulhon, P. Haensel, R. Livine, E. Paluch, S. Bonazzola, and J. Marck. Fast rotation of strange stars. *The Astrophysical Journal*, 349:851–862, Sep 1999. URL http://articles.adsabs.harvard.edu/pdf/1999A%26A...349..851G.

J. O. Goussard, P. Haensel, and J. L. Zdunik. Rapid uniform rotation of protoneutron stars. *Astronomy and Astrophysics*, 321:822–834, May 1997. doi:10.48550/arXiv.astro-ph/9610265.

P. Haensel and J. L. Zdunik. A submillisecond pulsar and the equation of state of dense matter. *Nature*, 340:617–619, Aug 1989. doi:10.1038/340617a0. URL https://doi.org/10.1038/340617a0.

P. Haensel, M. Salgado, and S. Bonazzola. Equation of state of dense matter and maximum rotation frequency of neutron stars. *Astronomy and Astrophysics*, 296:745, Apr. 1995.

P. Haensel, J. P. Lasota, and J. L. Zdunik. On the minimum period of uniformly rotating neutron stars. *Astronomy and Astrophysics*, 344:151–153, Apr. 1999.

P. Haensel, J. L. Zdunik, and F. Douchin. Equation of state of dense matter and the minimum mass of cold neutron stars. *Astronomy and Astrophysics*, 385(1):301–307, 2002. doi:10.1051/0004-6361:20020131. URL https://doi.org/10.1051/0004-6361:20020131.

P. Haensel, A. Potekhin, and D. Yakovlev. *Neutron Stars 1: Equation of State and Structure*. Springer-Verlag, New York, 2007.

P. Haensel, J. L. Zdunik, and M. Bejger. Fast rotation of neutron stars and equation of state of dense matter. *New Astronomy Reviews*, 51(10):785–790, 2008. ISSN 1387-6473. doi:https://doi.org/10.1016/j.newar.2008.03.007. URL https://www.sciencedirect.com/science/article/pii/S1387647308000092. Jean-Pierre Lasota, X-ray Binaries, Accretion Disks and Compact Stars.

P. Haensel, J. L. Zdunik, M. Bejger, and J. M. Lattimer. Keplerian frequency of uniformly rotating neutron stars and strange stars. *Astronomy and Astrophysics*, 502(2):605–610, 2009. doi:10.1051/0004-6361/200811605. URL https://doi.org/10.1051/0004-6361/200811605.

P. Haensel, M. Bejger, M. Fortin, and L. Zdunik. $I-Q$ relation for rapidly rotating neutron stars. *The European Physical Journal A*, 52:59, Mar 2016. doi:10.1140/epja/i2016-16059-4. URL https://doi.org/10.1140/epja/i2016-16059-4.

V. Hambaryan, V. Suleimanov, F. Haberl, A. D. Schwope, R. Neuhäuser, M. Hohle, and K. Werner. The compactness of the isolated neutron star rx20.4-3125. *Astronomy and Astrophysics*, 601:A108, 2017. doi:10.1051/0004-6361/201630368. URL https://doi.org/10.1051/0004-6361/201630368.

O. Hamil, J. R. Stone, M. Urbanec, and G. Urbancová. Braking index of isolated pulsars. *Physical Review D*, 91:063007, Mar 2015. doi:10.1103/PhysRevD.91.063007. URL https://link.aps.org/doi/10.1103/PhysRevD.91.063007.

B. Harrison, K. Thorne, M. Wakano, and J. Wheeler. *Gravitational Theory and Gravitational Collapse*. Chigago University Press, Chicago, 1965.

M.-A. Hashimoto, K. Oyamatsu, and Y. Eriguchi. Upper Limit of the Angular Velocity of Neutron Stars. *The Astrophysical Journal*, 436:257, Nov. 1994. doi:10.1086/174899.

B. Haskell, J. L. Zdunik, M. Fortin, M. Bejger, R. Wijnands, and A. Patruno. Fundamental physics and the absence of sub-millisecond pulsars. *Astronomy and Astrophysics*, 620:A69, 2018. doi:10.1051/0004-6361/201833521. URL https://doi.org/10.1051/0004-6361/201833521.

K. Hebeler and A. Schwenk. Chiral three-nucleon forces and neutron matter. *Physical Review C*, 82:014314, Jul 2010. doi:10.1103/PhysRevC.82.014314. URL https://link.aps.org/doi/10.1103/PhysRevC.82.014314.

K. Hebeler, J. M. Lattimer, C. J. Pethick, and A. Schwenk. Equation of state and neutron star properties constrained by nuclear physics and observation. *The Astrophysical Journal*, 773 (1):11, jul 2013. doi:10.1088/0004-637X/773/1/11. URL https://dx.doi.org/10.1088/0004-637X/773/1/11.

H. Heiselberg and M. Hjorth-Jensen. Phase transitions in rotating neutron stars. *Physical Review Letters*, 80:5485–5488, Jun 1998. doi:10.1103/PhysRevLett.80.5485. URL https://link.aps.org/doi/10.1103/PhysRevLett.80.5485.

H. Heiselberg and M. Hjorth-Jensen. Phases of dense matter in neutron stars. *Physics Reports*, 328(5):237 – 327, 2000. ISSN 0370-1573. doi:https://doi.org/10.1016/S0370-1573(99)00110-6. URL http://www.sciencedirect.com/science/article/pii/S0370157399001106.

L. Herrera, G. Le Denmat, and N. O. Santos. Dynamical instability for non-adiabatic spherical collapse. *Monthly Notices of the Royal Astronomical Society*, 237(1):257–268, 03 1989. ISSN 0035-8711. doi:10.1093/mnras/237.1.257. URL https://doi.org/10.1093/mnras/237.1.257.

J. W. T. Hessels, S. M. Ransom, I. H. Stairs, P. C. C. Freire, V. M. Kaspi, and F. Camilo. A radio pulsar spinning at 716 hz. *Science*, 311(5769):1901–1904, 2006. doi:10.1126/science.1123430. URL https://www.science.org/doi/abs/10.1126/science.1123430.

A. Hewish and S. E. Okoye. Evidence for an unusual source of high radio brightness temperature in the crab nebula. *Nature*, 207(4992):59–60, Jul 1965. doi:10.1038/207059a0.

A. Hewish, S. Bell, J. Pilkington, P. Scott, and R. Collins. Observation of a Rapidly Pulsating Radio Source. *The Astrophysical Journal*, 217:709–713, Feb. 1968. doi:10.1038/217709a0. URL https://doi.org/10.1038/217709a0.

W. Hiscock and L. Lindblom. Stability and causality in dissipative relativistic fluids. *Annals of Physics (N.Y.)*, 151:466, 1983. doi:10.1016/0003-4916(83)90288-9.

F. Hoyle, J. Narlikar, and J. Wheeler. Electromagnetic waves from very dense stars. *Nature*, 203: 914–916, Feb 1964. doi:10.1038/203914a0. URL https://doi.org/10.1038/203914a0.

R. A. Hulse and J. H. Taylor. Discovery of a pulsar in a binary system. *The Astrophysical Journal*, 195:L51–L53, Jan 1975. doi:10.1086/181708.

K. Iida and K. Sato. Spin down of neutron stars and compositional transitions in the cold crustal matter. *The Astrophysical Journal*, 477(1):294, mar 1997. doi:10.1086/303685. URL https://dx.doi.org/10.1086/303685.

J. R. Ipser. On the stability of ultrarelativistic stars. *Astrophysics and Space Science*, 7:361, Jun 1970. doi:10.1007/BF00653277. URL https://doi.org/10.1007/BF00653277.

J. D. Kaplan, C. D. Ott, E. P. O'Connor, K. Kiuchi, L. Roberts, and M. Duez. The influence of thermal pressure on equilibrium models of hypermassive neutron star merger remnants. *The Astrophysical Journal*, 790(1):19, jun 2014. doi:10.1088/0004-637x/790/1/19. URL https://doi.org/10.1088%2F0004-637x%2F790%2F1%2F19.

K. D. Kokkotas and J. Ruoff. Radial oscillations of relativistic stars*. *Astronomy and Astrophysics*, 366(2):565–572, 2001. doi:10.1051/0004-6361:20000216. URL https://doi.org/10.1051/0004-6361:20000216.

P. Koliogiannis and C. Moustakidis. Constraints on the equation of state from the stability condition of neutron stars. *Astrophysics and Space Science*, 364(3):52, Mar 2019. doi:10.1007/s10509-019-3539-7. URL https://doi.org/10.1007/s10509-019-3539-7.

P. S. Koliogiannis and C. C. Moustakidis. Effects of the equation of state on the bulk properties of maximally rotating neutron stars. *Physical Review C*, 101:015805, Jan 2020. doi:10.1103/PhysRevC.101.015805. URL https://link.aps.org/doi/10.1103/PhysRevC.101.015805.

P. S. Koliogiannis and C. C. Moustakidis. Thermodynamical description of hot, rapidly rotating neutron stars, protoneutron stars, and neutron star merger remnants. *The Astrophysical Journal*, 912(1):69, may 2021. doi:10.3847/1538-4357/abe542. URL https://dx.doi.org/10.3847/1538-4357/abe542.

S. Koranda, N. Stergioulas, and J. L. Friedman. Upper limits set by causality on the rotation and mass of uniformly rotating relativistic stars. *The Astrophysical Journal*, 488(2):799, oct 1997. doi:10.1086/304714. URL https://dx.doi.org/10.1086/304714.

C. Kouveliotou, S. Dieters, T. Strohmayer, J. van Paradijs, G. J. Fishman, C. A. Meegan, K. Hurley, J. Kommers, I. Smith, D. Frail, and T. Murakami. An x-ray pulsar with a superstrong magnetic field in the soft γ-ray repeater sgr1806 - 20. *Nature*, 393(6682):235–237, May 1998. ISSN 1476-4687. doi:10.1038/30410. URL https://doi.org/10.1038/30410.

R. Kozack and D. Madland. Prediction of intermediate-energy neutron scattering observables from a dirac optical potential. *Nuclear Physics A*, 509(4):664–672, 1990. ISSN 0375-9474. doi:https://doi.org/10.1016/0375-9474(90)90247-J. URL https://www.sciencedirect.com/science/article/pii/037594749090247J.

R. Kozack and D. G. Madland. Dirac optical potentials for nucleon scattering by ^{208}Pb at intermediate energies. *Physical Review C*, 39:1461–1474, Apr 1989. doi:10.1103/PhysRevC.39.1461. URL https://link.aps.org/doi/10.1103/PhysRevC.39.1461.

D. Kramer, H. Stephani, M. A. MacCallum, and E. Hert. *Exact Solutions of Einstein's Field Equations*. Deutsche Verlag der Wissenschaften, Berlin/Cambridge University Press, Cambridge, 1980.

P. G. Krastev, B.-A. Li, and A. Worley. Constraining properties of rapidly rotating neutron stars using data from heavy-ion collisions. *The Astrophysical Journal*, 676(2):1170, apr 2008. doi:10.1086/528736. URL https://dx.doi.org/10.1086/528736.

S. Köppel, L. Bovard, and L. Rezzolla. A general-relativistic determination of the threshold mass to prompt collapse in binary neutron star mergers. *The Astrophysical Journal*, 872(1):L16, feb 2019. doi:10.3847/2041-8213/ab0210. URL https://doi.org/10.3847%2F2041-8213%2Fab0210.

D. Q. Lamb, J. M. Lattimer, C. J. Pethick, and D. G. Ravenhall. Hot dense matter and stellar collapse. *Physical Review Letters*, 41:1623–1626, Dec 1978. doi:10.1103/PhysRevLett.41.1623. URL https://link.aps.org/doi/10.1103/PhysRevLett.41.1623.

L. D. Landau and E. M. Lifshitz. *Statistical physics. Pt.1*. Elsevier, Butterworth-Heinemann, 1969.

A. Lane. Isobaric spin dependence of the optical potential and quasi-elastic (p, n) reactions. *Nuclear Physics*, 35:676–685, 1962. ISSN 0029-5582. doi:https://doi.org/10.1016/0029-5582(62)90153-0. URL https://www.sciencedirect.com/science/article/pii/0029558262901530.

P. D. Lasky, B. Haskell, V. Ravi, E. J. Howell, and D. M. Coward. Nuclear equation of state from observations of short gamma-ray burst remnants. *Physical Review D*, 89:047302, Feb 2014. doi:10.1103/PhysRevD.89.047302. URL https://link.aps.org/doi/10.1103/PhysRevD.89.047302.

J.-P. Lasota, P. Haensel, and M. A. Abramowicz. Fast Rotation of Neutron Stars. *The Astrophysical Journal*, 456:300, Jan. 1996. doi:10.1086/176650.

J. M. Lattimer. The equation of state of hot dense matter and supernovae. *Annual Review of Nuclear and Particle Science*, 31(1):337–374, 1981. doi:10.1146/annurev.ns.31.120181.002005. URL https://doi.org/10.1146/annurev.ns.31.120181.002005.

J. M. Lattimer. Neutron star equation of state. *New Astronomy Reviews*, 54(3):101–109, 2010. ISSN 1387-6473. doi:https://doi.org/10.1016/j.newar.2010.09.013. URL https://www.sciencedirect.com/science/article/pii/S1387647310000564. Proceedings: A Life With Stars.

J. M. Lattimer. The nuclear equation of state and neutron star masses. *Annual Review of Nuclear and Particle Science*, 62(1):485–515, 2012. doi:10.1146/annurev-nucl-102711-095018. URL https://doi.org/10.1146/annurev-nucl-102711-095018.

J. M. Lattimer. Neutron stars. *General Relativity and Gravitation*, 46:1713, 2014. ISSN 1387-6473. doi:10.1007/s10714-014-1713-3. URL https://doi.org/10.1007/s10714-014-1713-3.

J. M. Lattimer. Introduction to neutron stars. *AIP Conference Proceedings*, 1645(1):61–78, 2015. doi:10.1063/1.4909560. URL https://aip.scitation.org/doi/abs/10.1063/1.4909560.

J. M. Lattimer. *Perspectives on the Equation of State in Neutron Stars*, volume 14, chapter 010801, page 6. The Physical Society of Japan, 2017. doi:10.7566/JPSCP.14.010801. URL https://journals.jps.jp/doi/abs/10.7566/JPSCP.14.010801.

J. M. Lattimer. Neutron star mass and radius measurements. *Universe*, 5(7), 2019. ISSN 2218-1997. doi:10.3390/universe5070159. URL https://www.mdpi.com/2218-1997/5/7/159.

J. M. Lattimer and M. Prakash. Neutron star structure and the equation of state. *The Astrophysical Journal*, 550(1):426, mar 2001. doi:10.1086/319702. URL https://dx.doi.org/10.1086/319702.

J. M. Lattimer and M. Prakash. The physics of neutron stars. *Science*, 304(5670):536–542, 2004. doi:10.1126/science.1090720. URL https://www.science.org/doi/abs/10.1126/science.1090720.

J. M. Lattimer and M. Prakash. Ultimate energy density of observable cold baryonic matter. *Physical Review Letters*, 94:111101, Mar 2005. doi:10.1103/PhysRevLett.94.111101. URL https://link.aps.org/doi/10.1103/PhysRevLett.94.111101.

J. M. Lattimer and M. Prakash. *Quarks, Nuclei and Stars: Memorial Volume Dedicated to Gerald E. Brown*. World Scientific, Singapore, 2011.

J. M. Lattimer and M. Prakash. The equation of state of hot, dense matter and neutron stars. *Physics Reports*, 621:127 – 164, 2016. ISSN 0370-1573. doi:https://doi.org/10.1016/j.physrep.2015.12.005. URL http://www.sciencedirect.com/science/article/pii/S0370157315005396. Memorial Volume in Honor of Gerald E. Brown.

J. M. Lattimer and D. G. Ravenhall. Neutron star matter at high temperatures and densities. i. bulk properties of nuclear matter. *The Astrophysical Journal*, 223:314–323, Jul 1978. doi:10.1086/156265. URL https://ui.adsabs.harvard.edu/abs/1978ApJ...223..314L/abstract.

J. M. Lattimer and D. N. Schramm. Black-Hole-Neutron-Star Collisions. *The Astrophysical Journal*, 192:L145, Sept. 1974. doi:10.1086/181612.

J. M. Lattimer and B. F. Schutz. Constraining the equation of state with moment of inertia measurements. *The Astrophysical Journal*, 629(2):979, aug 2005. doi:10.1086/431543. URL https://dx.doi.org/10.1086/431543.

J. M. Lattimer and F. D. Swesty. A generalized equation of state for hot, dense matter. *Nuclear Physics A*, 535(2):331 – 376, 1991. ISSN 0375-9474. doi:https://doi.org/10.1016/0375-9474(91)90452-C. URL http://www.sciencedirect.com/science/article/pii/037594749190452C.

J. M. Lattimer, M. Prakash, D. Masak, and A. Yahil. Rapidly rotating pulsars and the equation of state. *The Astrophysical Journal*, 355:241, 1990. doi:10.1086/168758. URL https://ui.adsabs.harvard.edu/abs/1990ApJ...355..241L/abstract.

B.-A. Li. Constraining the neutron-proton effective mass splitting in neutron-rich matter. *Physical Review C*, 69:064602, Jun 2004. doi:10.1103/PhysRevC.69.064602. URL https://link.aps.org/doi/10.1103/PhysRevC.69.064602.

B.-A. Li and W.-U. Schröder. *Isospin Physics in Heavy-Ion Collisions at Intermediate Energies*. New York: Nova Science, 2001.

B.-A. Li, C. B. Das, S. Das Gupta, and C. Gale. Momentum dependence of the symmetry potential and nuclear reactions induced by neutron-rich nuclei at ria. *Physical Review C*, 69: 011603, Jan 2004a. doi:10.1103/PhysRevC.69.011603. URL https://link.aps.org/doi/10.1103/PhysRevC.69.011603.

B.-A. Li, C. B. Das, S. D. Gupta, and C. Gale. Effects of momentum-dependent symmetry potential on heavy-ion collisions induced by neutron-rich nuclei. *Nuclear Physics A*, 735(3): 563 – 584, 2004b. ISSN 0375-9474. doi:https://doi.org/10.1016/j.nuclphysa.2004.02.016. URL http://www.sciencedirect.com/science/article/pii/S0375947404002052.

B.-A. Li, L.-W. Chen, and C. M. Ko. Recent progress and new challenges in isospin physics with heavy-ion reactions. *Physics Reports*, 464(4):113 – 281, 2008. ISSN 0370-1573. doi:https://doi.org/10.1016/j.physrep.2008.04.005. URL http://www.sciencedirect.com/science/article/pii/S0370157308001269.

B.-A. Li, B.-J. Cai, L.-W. Chen, and J. Xu. Nucleon effective masses in neutron-rich matter. *Progress in Particle and Nuclear Physics*, 99:29–119, 2018. ISSN 0146-6410. doi:https://doi.org/10.1016/j.ppnp.2018.01.001. URL https://www.sciencedirect.com/science/article/pii/S0146641018300012.

F. Li, J.-J. Lu, Z.-H. Li, C.-Y. Chen, G. F. Burgio, and H.-J. Schulze. Accurate nuclear symmetry energy at finite temperature within a brueckner-hartree-fock approach. *Physical Review C*,

103:024307, Feb 2021. doi:10.1103/PhysRevC.103.024307. URL https://link.aps.org/doi/10.1103/PhysRevC.103.024307.

G. Q. Li and R. Machleidt. Momentum-dependent mean field based upon the dirac-brueckner approach for nuclear matter. *Physical Review C*, 48:2707–2713, Dec 1993. doi:10.1103/PhysRevC.48.2707. URL https://link.aps.org/doi/10.1103/PhysRevC.48.2707.

J. J. Li, A. Sedrakian, and F. Weber. Rapidly rotating δ-resonance-admixed hypernuclear compact stars. *Physics Letters B*, 810:135812, 2020. ISSN 0370-2693. doi:https://doi.org/10.1016/j.physletb.2020.135812. URL http://www.sciencedirect.com/science/article/pii/S0370269320306158.

M. Linares, T. Shahbaz, and J. Casares. Peering into the Dark Side: Magnesium Lines Establish a Massive Neutron Star in PSR J2215+5135. *The Astrophysical Journal*, 859:54, 2018. doi:10.3847/1538-4357/aabde6.

L. Lindblom. Estimates of the Maximum Angular Velocity of Rotating Neutron Stars. *The Astrophysical Journal*, 303:146, Apr. 1986. doi:10.1086/164061.

L. Lindblom and S. L. Detweiler. The quadrupole oscillations of neutron stars. *The Astrophysical Journal Supplement Series*, 53:73–92, Sept. 1983. doi:10.1086/190884.

K.-W. Lo and L.-M. Lin. The spin parameter of uniformly rotating compact stars. *The Astrophysical Journal*, 728(1):12, jan 2011. doi:10.1088/0004-637X/728/1/12. URL https://dx.doi.org/10.1088/0004-637X/728/1/12.

LORENE. Lorene: Langage objet pour la relativité numérique, 1998. URL http://lorene.obspm.fr/.

D. Lorimer and M. Kramer. *Handbook of Pulsar Astronomy*. Cambridge University Press, Cambridge, 2005.

D. R. Lorimer. Binary and millisecond pulsars. *Living Reviews in Relativity*, 11:8, Nov 2008. doi:10.12942/lrr-2008-8. URL https://doi.org/10.12942/lrr-2008-8.

J.-J. Lu, Z.-H. Li, G. F. Burgio, A. Figura, and H.-J. Schulze. Hot neutron stars with microscopic equations of state. *Physical Review C*, 100:054335, Nov 2019. doi:10.1103/PhysRevC.100.054335. URL https://link.aps.org/doi/10.1103/PhysRevC.100.054335.

A. G. Lyne, C. A. Jordan, F. Graham-Smith, C. M. Espinoza, B. W. Stappers, and P. Weltevrede. 45 years of rotation of the Crab pulsar. *Monthly Notices of the Royal Astronomical Society*, 446(1):857–864, 11 2014. ISSN 0035-8711. doi:10.1093/mnras/stu2118. URL https://doi.org/10.1093/mnras/stu2118.

R. N. Manchester, G. B. Hobbs, A. Teoh, and M. Hobbs. The australia telescope national facility pulsar catalogue. *The Astronomical Journal*, 129(4):1993, apr 2005. doi:10.1086/428488. URL https://dx.doi.org/10.1086/428488.

B. Margalit and B. D. Metzger. Constraining the maximum mass of neutron stars from multi-messenger observations of gw170817. *The Astrophysical Journal Letters*, 850(2):L19, nov 2017. doi:10.3847/2041-8213/aa991c. URL https://dx.doi.org/10.3847/2041-8213/aa991c.

C. Margaritis, P. S. Koliogiannis, A. Kanakis-Pegios, and C. C. Moustakidis. Crust-core interface and bulk neutron star properties. *Physical Review C*, 104:025805, Aug 2021. doi:10.1103/PhysRevC.104.025805. URL https://link.aps.org/doi/10.1103/PhysRevC.104.025805.

M. Marques, M. Oertel, M. Hempel, and J. Novak. New temperature dependent hyperonic equation of state: Application to rotating neutron star models and $i-q$ relations. *Physical Review C*, 96:045806, Oct 2017. doi:10.1103/PhysRevC.96.045806. URL https://link.aps.org/doi/10.1103/PhysRevC.96.045806.

A. Maselli, P. Pnigouras, N. G. Nielsen, C. Kouvaris, and K. D. Kokkotas. Dark stars: Gravitational and electromagnetic observables. *Physical Review D*, 96:023005, Jul 2017. doi:10.1103/PhysRevD.96.023005. URL https://link.aps.org/doi/10.1103/PhysRevD.96.023005.

M. Merafina and R. Ruffini. Systems of selfgravitating classical particles with a cutoff in their distribution function. *Astronomy and Astrophysics*, 221(1):4–19, Aug. 1989.

M. C. Miller and F. K. Lamb. Bounds on the compactness of neutron stars from brightness oscillations during x-ray bursts. *The Astrophysical Journal*, 499(1):L37, may 1998. doi:10.1086/311335. URL https://dx.doi.org/10.1086/311335.

C. Misner, K. Thorne, and J. Wheeler. *Gravitation*. Freeman, San Francisco, 1973.

M. Modarres. Lowest-order constrained variational calculation for hot asymmetric nuclear matter. *Journal of Physics G: Nuclear and Particle Physics*, 23(8):923–937, aug 1997. doi:10.1088/0954-3899/23/8/007. URL https://doi.org/10.1088%2F0954-3899%2F23%2F8%2F007.

I. A. Morrison, T. W. Baumgarte, and S. L. Shapiro. Effect of differential rotation on the maximum mass of neutron stars: Realistic nuclear equations of state. *The Astrophysical Journal*, 610(2): 941–947, aug 2004. doi:10.1086/421897. URL https://doi.org/10.1086%2F421897.

S. M. Morsink, N. Stergioulas, and S. R. Blattnig. Quasi-normal modes of rotating relativistic stars: Neutral modes for realistic equations of state. *The Astrophysical Journal*, 510(2): 854–861, jan 1999. doi:10.1086/306630. URL https://doi.org/10.1086%2F306630.

E. R. Most, L. J. Papenfort, L. R. Weih, and L. Rezzolla. A lower bound on the maximum mass if the secondary in GW190814 was once a rapidly spinning neutron star. *Monthly Notices of the Royal Astronomical Society: Letters*, 499(1):L82–L86, 09 2020. ISSN 1745-3925. doi:10.1093/mnrasl/slaa168. URL https://doi.org/10.1093/mnrasl/slaa168.

C. Moustakidis. The stability of relativistic stars and the role of the adiabatic index. *General Relativity and Gravitation*, 49:68, Apr 2017. doi:10.1007/s10714-017-2232-9. URL https://doi.org/10.1007/s10714-017-2232-9.

C. C. Moustakidis. Thermal effects on nuclear symmetry energy with a momentum-dependent effective interaction. *Physical Review C*, 76:025805, Aug 2007. doi:10.1103/PhysRevC.76.025805. URL https://link.aps.org/doi/10.1103/PhysRevC.76.025805.

C. C. Moustakidis. Temperature and momentum dependence of single-particle properties in hot asymmetric nuclear matter. *Physical Review C*, 78:054323, Nov 2008. doi:10.1103/PhysRevC.78.054323. URL https://link.aps.org/doi/10.1103/PhysRevC.78.054323.

C. C. Moustakidis. Equation of state for dense supernova matter. *International Journal of Modern Physics D*, 18(08):1205–1226, 2009. doi:10.1142/S0218271809015023. URL https://doi.org/10.1142/S0218271809015023.

C. C. Moustakidis and C. P. Panos. Equation of state for β-stable hot nuclear matter. *Physical Review C*, 79:045806, Apr 2009. doi:10.1103/PhysRevC.79.045806. URL https://link.aps.org/doi/10.1103/PhysRevC.79.045806.

H. Nariai. On some static solutions of Einstein's gravitational field equations in a spherically symmetric case. *Scientific Reports of the Tohoku University Eighth Ser.*, 34:160, Jan. 1950.

H. Nariai. On a new cosmological solution of Einstein's field equations of gravitation. *Scientific Reports of the Tohoku University Eighth Ser.*, 35:46, Jan. 1951.

H. Nariai. On some static solutions of einstein's gravitational field equations in a spherically symmetric case. *General Relativity and Gravitation*, 31:951–961, Jun 1999. doi:10.1023/A:1026698508110. URL https://doi.org/10.1023/A:1026698508110.

P. Negi and M. Durgapal. Relativistic supermassive stars. *Astrophysics and Space Science*, 275:185, Feb 2001. doi:10.1023/A:1002707730439. URL https://doi.org/10.1023/A:1002707730439.

P. S. Negi and M. C. Durgapal. Stable ultracompact objects. *General Relativity and Gravitation*, 31:13, Jan 1999. doi:10.1023/A:1018807219245. URL https://doi.org/10.1023/A:1018807219245.

O. E. Nicotra, M. Baldo, G. F. Burgio, and H.-J. Schulze. Protoneutron stars within the brueckner-bethe-goldstone theory. *The Astrophysical Journal*, 451(1):213–222, 2006. doi:10.1051/0004-6361:20053670. URL https://doi.org/10.1051/0004-6361:20053670.

J. R. Oppenheimer and G. M. Volkoff. On massive neutron cores. *Physical Review*, 55:374–381, Feb 1939. doi:10.1103/PhysRev.55.374. URL https://link.aps.org/doi/10.1103/PhysRev.55.374.

V. Pandharipande and R. Smith. Nuclear matter calculations with mean scalar fields. *Physics Letters B*, 59(1):15–18, 1975. ISSN 0370-2693. doi:https://doi.org/10.1016/0370-2693(75)90143-4. URL https://www.sciencedirect.com/science/article/pii/0370269375901434.

M. C. Papazoglou and C. C. Moustakidis. R-mode constraints from neutron star equation of state. *Astrophysics and Space Science*, 361:98, Feb 2016. doi:10.1007/s10509-016-2692-5. URL https://doi.org/10.1007/s10509-016-2692-5.

V. Paschalidis and N. Stergioulas. Rotating stars in relativity. *Living Reviews in Relativity*, 20:7, Nov 2017. doi:10.1007/s41114-017-0008-x. URL https://doi.org/10.1007/s41114-017-0008-x.

A. Patruno, B. Haskell, and N. Andersson. The spin distribution of fast-spinning neutron stars in low-mass x-ray binaries: Evidence for two subpopulations. *The Astrophysical Journal*, 850 (1):106, nov 2017. doi:10.3847/1538-4357/aa927a. URL https://dx.doi.org/10.3847/1538-4357/aa927a.

A. Perego, S. Bernouzzi, and D. Radie. Thermodynamics conditions of matter in neutron star mergers. *The European Physical Journal A*, 55:124, 2019. doi:https://doi.org/10.1140/epja/i2019-12810-7.

M. Piarulli, I. Bombaci, D. Logoteta, A. Lovato, and R. B. Wiringa. Benchmark calculations of pure neutron matter with realistic nucleon-nucleon interactions. *Physical Review C*, 101: 045801, Apr 2020. doi:10.1103/PhysRevC.101.045801. URL https://link.aps.org/doi/10.1103/PhysRevC.101.045801.

J. H. Piddington. Pulsars and magnetic amplification. *Nature*, 222(5197):965–966, Jun 1969. ISSN 1476-4687. doi:10.1038/222965a0. URL https://doi.org/10.1038/222965a0.

J. A. Pons, S. Reddy, M. Prakash, J. M. Lattimer, and J. A. Miralles. Evolution of proto–neutron stars. *The Astrophysical Journal*, 513(2):780–804, mar 1999. doi:10.1086/306889. URL https://doi.org/10.1086%2F306889.

M. Prakash. *The Equation of State and Neutron Star*. unpublished, 1994.

M. Prakash. Neutron stars as probes of extreme energy density matter. *Pramana - Journal of Physics*, 84:924–941, may 2015. doi:10.1007/s12043-015-0979-7. URL https://doi.org/10.1007/s12043-015-0979-7.

M. Prakash, T. T. S. Kuo, and S. Das Gupta. Momentum dependence, boltzmann-uehling-uhlenbeck calculations, and transverse momenta. *Physical Review C*, 37:2253–2256, May 1988. doi:10.1103/PhysRevC.37.2253. URL https://link.aps.org/doi/10.1103/PhysRevC.37.2253.

M. Prakash, I. Bombaci, M. Prakash, P. J. Ellis, J. M. Lattimer, and R. Knorren. Composition and structure of protoneutron stars. *Physics Report*, 280(1):1 – 77, 1997. ISSN 0370-1573. doi:https://doi.org/10.1016/S0370-1573(96)00023-3. URL http://www.sciencedirect.com/science/article/pii/S0370157396000233.

M. Prakash, J. Lattimer, J. Pons, A. Steiner, and S. Reddy. Evolution of a neutron star from its birth to old age. *Lecture Notes Physics*, 578:364–423, 2001. doi:10.1007/3-540-44578-1.

V. P. Psonis, C. C. Moustakidis, and S. E. Massen. Nuclear symmetry energy effects on neutron stars properties. *Modern Physics Letters A*, 22:1233–1253, 2007. doi:https://doi.org/10.1142/S0217732307023572.

V. Radhakrishnan and R. N. Manchester. Detection of a change of state in the pulsar psr 0833-45. *Nature*, 222(5190):228–229, Apr 1969. ISSN 1476-4687. doi:10.1038/222228a0. URL https://doi.org/10.1038/222228a0.

D. Radice, S. Bernuzzi, and A. Perego. The dynamics of binary neutron star mergers and gw170817. *Annual Review of Nuclear and Particle Science*, 70(1):null, 2020. doi:10.1146/annurev-nucl-013120-114541. URL https://doi.org/10.1146/annurev-nucl-013120-114541.

A. R. Raduta, M. Oertel, and A. Sedrakian. Proto-neutron stars with heavy baryons and universal relations. *Monthly Notices of the Royal Astronomical Society*, 499(1):914–931, 08 2020. ISSN 0035-8711. doi:10.1093/mnras/staa2491. URL https://doi.org/10.1093/mnras/staa2491.

A. M. Raghoonundun and D. W. Hobill. Possible physical realizations of the tolman vii solution. *Physical Review D*, 92:124005, Dec 2015. doi:10.1103/PhysRevD.92.124005. URL https://link.aps.org/doi/10.1103/PhysRevD.92.124005.

C. A. Raithel, F. Özel, and D. Psaltis. Finite-temperature extension for cold neutron star equations of state. *The Astrophysical Journal*, 875(1):12, apr 2019. doi:10.3847/1538-4357/ab08ea. URL https://doi.org/10.3847%2F1538-4357%2Fab08ea.

D. G. Ravenhall and C. J. Pethick. Neutron Star Moments of Inertia. *The Astrophysical Journal*, 424:846, Apr. 1994. doi:10.1086/173935.

V. Ravi and P. D. Lasky. The birth of black holes: neutron star collapse times, gamma-ray bursts and fast radio bursts. *Monthly Notices of the Royal Astronomical Society*, 441(3):2433–2439, 05 2014. ISSN 0035-8711. doi:10.1093/mnras/stu720. URL https://doi.org/10.1093/mnras/stu720.

P. E. Reichley and G. S. Downs. Observed decrease in the periods of pulsar psr 0833–45. *Nature*, 222(5190):229–230, Apr 1969. ISSN 1476-4687. doi:10.1038/222229a0. URL https://doi.org/10.1038/222229a0.

R. Riahi, S. Z. Kalantari, and J. A. Rueda. Universal relations for the keplerian sequence of rotating neutron stars. *Physical Review D*, 99:043004, Feb 2019. doi:10.1103/PhysRevD.99.043004. URL https://link.aps.org/doi/10.1103/PhysRevD.99.043004.

A. G. Rosso, F. Vissani, and M. C. Volpe. Measuring the neutron star compactness and binding energy with supernova neutrinos. *Journal of Cosmology and Astroparticle Physics*, 2017 (11):036, nov 2017. doi:10.1088/1475-7516/2017/11/036. URL https://dx.doi.org/10.1088/1475-7516/2017/11/036.

M. Salgado, S. Bonazzola, E. Gourgoulhon, and P. Haensel. High precision rotating neutron star models. II. Large sample of neutron star properties. *Astronomy and Astrophysics Supplement Series*, 108:455–459, Dec. 1994a.

M. Salgado, S. Bonazzola, E. Gourgoulhon, and P. Haensel. High precision rotating neutron star models. I. Analysis of neutron star properties. *Astronomy and Astrophysics*, 291:155–170, Nov. 1994b.

F. Sammarruca, R. Machleidt, and R. Millerson. Temperature effects on the neutron matter equation of state obtained from chiral effective field theory. *Modern Physics Letters A*, 35 (19):2050156, 2020. doi:10.1142/S0217732320501564. URL https://doi.org/10.1142/S0217732320501564.

N. Sarin, P. D. Lasky, and G. Ashton. Gravitational waves or deconfined quarks: What causes the premature collapse of neutron stars born in short gamma-ray bursts? *Physical Review D*, 101:063021, Mar 2020. doi:10.1103/PhysRevD.101.063021. URL https://link.aps.org/doi/10.1103/PhysRevD.101.063021.

B. Schutz. *A First Course in General Relativity*. Cambridge Univer- sity Press, Cambridge, 1985.

D. Sen. Nuclear matter at finite temperature and static properties of proto-neutron star. *Journal of Physics G: Nuclear and Particle Physics*, Nov 2020. ISSN 1361-6471. doi:10.1088/1361-6471/abcb9e. URL http://dx.doi.org/10.1088/1361-6471/abcb9e.

X. L. Shang, A. Li, Z. Q. Miao, G. F. Burgio, and H.-J. Schulze. Nucleon effective mass in hot dense matter. *Physical Review C*, 101:065801, Jun 2020. doi:10.1103/PhysRevC.101.065801. URL https://link.aps.org/doi/10.1103/PhysRevC.101.065801.

D.-S. Shao, S.-P. Tang, X. Sheng, J.-L. Jiang, Y.-Z. Wang, Z.-P. Jin, Y.-Z. Fan, and D.-M. Wei. Estimating the maximum gravitational mass of nonrotating neutron stars from the gw170817/grb 170817a/at2017gfo observation. *Physical Review D*, 101:063029, Mar 2020. doi:10.1103/PhysRevD.101.063029. URL https://link.aps.org/doi/10.1103/PhysRevD.101.063029.

S. L. Shapiro and S. A. Teukolsky. *Black Holes, White Dwarfs, and Neutron Stars*. John Wiley & Sons, New York, 1983.

S. L. Shapiro, S. A. Teukolsky, and I. Wasserman. Testing nuclear theory using the 0.5 ms pulsar. *Nature*, 340:451–452, Aug 1989. doi:10.1038/340451a0. URL https://doi.org/10.1038/340451a0.

M. Sharif and Z. Yousaf. Role of adiabatic index on the evolution of spherical gravitational collapse in palatini f(r) gravity. *Astrophysics and Space Science*, 355: 317, Feb 2015. doi:10.1007/s10509-014-2179-1. URL https://doi.org/10.1007/s10509-014-2179-1.

B. K. Sharma, M. Centelles, X. Viñas, M. Baldo, and G. F. Burgio. Unified equation of state for neutron stars on a microscopic basis. *Astronomy and Astrophysics*, 584:A103, 2015. doi:10.1051/0004-6361/201526642. URL https://doi.org/10.1051/0004-6361/201526642.

G. Shen, C. J. Horowitz, and E. O'Connor. Second relativistic mean field and virial equation of state for astrophysical simulations. *Physical Review C*, 83:065808, Jun 2011. doi:10.1103/PhysRevC.83.065808. URL https://link.aps.org/doi/10.1103/PhysRevC.83.065808.

H. Shen, H. Toki, K. Oyamatsu, and K. Sumiyoshi. Relativistic equation of state of nuclear matter for supernova and neutron star. *Nuclear Physics A*, 637(3):435 – 450, 1998. ISSN 0375-9474. doi:https://doi.org/10.1016/S0375-9474(98)00236-X. URL http://www.sciencedirect.com/science/article/pii/S037594749800236X.

M. Shibata. Collapse of rotating supramassive neutron stars to black holes: Fully general relativistic simulations. *The Astrophysical Journal*, 595(2):992, oct 2003. doi:10.1086/377435. URL https://dx.doi.org/10.1086/377435.

M. Shibata, T. W. Baumgarte, and S. L. Shapiro. Stability and collapse of rapidly rotating, supramassive neutron stars: 3d simulations in general relativity. *Physical Review D*, 61: 044012, Jan 2000. doi:10.1103/PhysRevD.61.044012. URL https://link.aps.org/doi/10.1103/PhysRevD.61.044012.

H. O. Silva and N. Yunes. I-love-q to the extreme. *Classical and Quantum Gravity*, 35(1): 015005, dec 2017. doi:10.1088/1361-6382/aa995a. URL https://dx.doi.org/10.1088/1361-6382/aa995a.

H. O. Silva, H. Sotani, and E. Berti. Low-mass neutron stars: universal relations, the nuclear symmetry energy and gravitational radiation. *Monthly Notices of the Royal Astronomical Society*, 459(4):4378–4388, 04 2016. ISSN 0035-8711. doi:10.1093/mnras/stw969. URL https://doi.org/10.1093/mnras/stw969.

S. Soma and D. Bandyopadhyay. Properties of binary components and remnant in GW170817 using equations of state in finite temperature field theory models. *The Astrophysical Journal*, 890(2):139, feb 2020. doi:10.3847/1538-4357/ab6a9e. URL https://doi.org/10.3847%2F1538-4357%2Fab6a9e.

R. D. Sorkin. A stability criterion for many parameter equilibrium families. *The Astrophysical Journal*, 257:847, jun 1982. doi:10.1086/160034.

H. Sotani and K. D. Kokkotas. Compactness of neutron stars and tolman vii solutions in scalar-tensor gravity. *Physical Review D*, 97:124034, Jun 2018. doi:10.1103/PhysRevD.97.124034. URL https://link.aps.org/doi/10.1103/PhysRevD.97.124034.

N. Stergioulas. Rotating stars in relativity. *Living Reviews in Relativity*, 1:8, jun 1998. doi:10.12942/lrr-1998-8. URL https://doi.org/10.12942/lrr-1998-8.

N. Stergioulas. Rotating stars in relativity. *Living Reviews in Relativity*, 6:3, 2003. doi:10.12942/lrr-2003-3. URL https://doi.org/10.12942/lrr-2003-3.

N. Stergioulas and J. L. Friedman. Comparing Models of Rapidly Rotating Relativistic Stars Constructed by Two Numerical Methods. *The Astrophysical Journal*, 444:306, May 1995. doi:10.1086/175605.

I.-S. Suh and G. J. Mathews. Cold ideal equation of state for strongly magnetized neutron star matter: Effects on muon production and pion condensation. *The Astrophysical Journal*, 546 (2):1126–1136, jan 2001. doi:10.1086/318277. URL https://doi.org/10.1086/318277.

K. Sumiyoshi and H. Toki. Relativistic equation of state of nuclear matter for the supernova explosion and the birth of neutron stars. *The Astrophysical Journal*, 422:700, feb 1994. doi:10.1086/173763.

K. Sumiyoshi, S. Yamada, H. Suzuki, and W. Hillebrandt. The fate of a neutron star just below the minimum mass: does it explode? *The Astrophysical Journal*, 334:159–168, June 1998. doi:10.48550/arXiv.astro-ph/9707230.

K. Sumiyoshi, J. a Ibáñez, and J. V. Romero. Thermal history and structure of rotating protoneutron stars with relativistic equation of state. *Astronomy and Astrophysics*, 134(1):39–52, 1999. doi:10.1051/aas:1999123. URL https://doi.org/10.1051/aas:1999123.

Y. Suwa, T. Yoshida, M. Shibata, H. Umeda, and K. Takahashi. On the minimum mass of neutron stars. *Monthly Notices of the Royal Astronomical Society*, 481(3):3305–3312, 09 2018. ISSN 0035-8711. doi:10.1093/mnras/sty2460. URL https://doi.org/10.1093/mnras/sty2460.

K. Takami, L. Rezzolla, and S. Yoshida. A quasi-radial stability criterion for rotating relativistic stars. *Monthly Notices of the Royal Astronomical Society: Letters*, 416(1):L1–L5, 09 2011. ISSN 1745-3925. doi:10.1111/j.1745-3933.2011.01085.x. URL https://doi.org/10.1111/j.1745-3933.2011.01085.x.

T. Takatsuka. Hot Neutron Stars at Birth and Related Problems. *Progress of Theoretical Physics*, 95(5):901–912, 05 1996. ISSN 0033-068X. doi:10.1143/PTP.95.901. URL https://doi.org/10.1143/PTP.95.901.

T. Takatsuka, S. Nishizaki, and J. Hiura. Particular Properties of Dense Supernova Matter. *Progress of Theoretical Physics*, 92(4):779–802, 10 1994. ISSN 0033-068X. doi:10.1143/ptp/92.4.779. URL https://doi.org/10.1143/ptp/92.4.779.

N. H. Tan, D. T. Loan, D. T. Khoa, and J. Margueron. Mean-field study of hot β-stable protoneutron star matter: Impact of the symmetry energy and nucleon effective mass. *Physical Review C*, 93:035806, Mar 2016. doi:10.1103/PhysRevC.93.035806. URL https://link.aps.org/doi/10.1103/PhysRevC.93.035806.

J. H. Taylor, L. A. Fowler, and P. M. McCulloch. Measurements of general relativistic effects in the binary pulsar psr1913 + 16. *Nature*, 277(5696):437–440, Feb 1979. ISSN 1476-4687. doi:10.1038/277437a0. URL https://doi.org/10.1038/277437a0.

K. S. Thorne. Disk-accretion onto a black hole. ii. evolution of the hole. *The Astrophysical Journal*, 191:507–520, Jul 1974. doi:https://doi.org/10.1086/152991.

R. C. Tolman. Static solutions of einstein's field equations for spheres of fluid. *Physical Review*, 55:364–373, Feb 1939. doi:10.1103/PhysRev.55.364. URL https://link.aps.org/doi/10.1103/PhysRev.55.364.

L. Tolos, M. Centelles, and A. Ramos. The equation of state for the nucleonic and hyperonic core of neutron stars. *Publications of the Astronomical Society of Australia*, 34:e065, 2017a. doi:10.1017/pasa.2017.60.

L. Tolos, M. Centelles, and A. Ramos. The equation of state for the nucleonic and hyperonic core of neutron stars. *Publications of the Astronomical Society of Australia*, 34:e065, 2017b. doi:10.1017/pasa.2017.60.

R. F. Tooper. General relativistic polytropic fluid spheres. *The Astrophysical Journal*, 140:434, Aug 1964. doi:10.1086/147939. URL https://ui.adsabs.harvard.edu/abs/1964ApJ...140..434T/abstract.

R. F. Tooper. Adiabatic Fluid Spheres in General Relativity. *The Astrophysical Journal*, 142: 1541, Nov. 1965. doi:10.1086/148435.

A. Tsokaros, M. Ruiz, S. L. Shapiro, L. Sun, and K. b. o. Uryū. Great impostors: Extremely compact, merging binary neutron stars in the mass gap posing as binary black holes. *Physical Review Letters*, 124:071101, Feb 2020. doi:10.1103/PhysRevLett.124.071101. URL https://link.aps.org/doi/10.1103/PhysRevLett.124.071101.

E. van Dalen, C. Fuchs, and A. Faessler. The relativistic dirac–brueckner approach to asymmetric nuclear matter. *Nuclear Physics A*, 744:227–248, 2004. ISSN 0375-9474. doi:https://doi.org/10.1016/j.nuclphysa.2004.08.019. URL https://www.sciencedirect.com/science/article/pii/S0375947404008711.

E. N. E. van Dalen, C. Fuchs, and A. Faessler. Effective nucleon masses in symmetric and asymmetric nuclear matter. *Physical Review Letters*, 95:022302, Jul 2005. doi:10.1103/PhysRevLett.95.022302. URL https://link.aps.org/doi/10.1103/PhysRevLett.95.022302.

K. S. Virbhadra. Relativistic images of schwarzschild black hole lensing. *Physical Review D*, 79:083004, Apr 2009. doi:10.1103/PhysRevD.79.083004. URL https://link.aps.org/doi/10.1103/PhysRevD.79.083004.

K. S. Virbhadra and G. F. R. Ellis. Schwarzschild black hole lensing. *Physical Review D*, 62: 084003, Sep 2000. doi:10.1103/PhysRevD.62.084003. URL https://link.aps.org/doi/10.1103/PhysRevD.62.084003.

K. S. Virbhadra and G. F. R. Ellis. Gravitational lensing by naked singularities. *Physical Review D*, 65:103004, May 2002. doi:10.1103/PhysRevD.65.103004. URL https://link.aps.org/doi/10.1103/PhysRevD.65.103004.

K. S. Virbhadra and C. R. Keeton. Time delay and magnification centroid due to gravitational lensing by black holes and naked singularities. *Physical Review D*, 77:124014, Jun 2008. doi:10.1103/PhysRevD.77.124014. URL https://link.aps.org/doi/10.1103/PhysRevD.77.124014.

J. Walecka. A theory of highly condensed matter. *Annals of Physics*, 83(2):491–529, 1974. ISSN 0003-4916. doi:https://doi.org/10.1016/0003-4916(74)90208-5. URL https://www.sciencedirect.com/science/article/pii/0003491674902085.

F. M. Walter, S. J. Wolk, and R. Neuhäuser. Discovery of a nearby isolated neutron star. *Nature*, 379(6562):233–235, Jan 1996. ISSN 1476-4687. doi:10.1038/379233a0. URL https://doi.org/10.1038/379233a0.

F. Weber. *Pulsars as astrophysical laboratories for nuclear and particle physics*. UK: Institute of Physics, Bristol, 1996.

F. Weber. *Pulsars as Astrophysical Laboratories for Nuclear and Particle Physics*. Taylor & Francis, London, 1999.

F. Weber and N. Glendenning. Exact versus approximate solution of einstein's equations for rotating neutron stars. *Physics Letters B*, 265(1):1–5, 1991. ISSN 0370-2693. doi:https://doi.org/10.1016/0370-2693(91)90002-8. URL https://www.sciencedirect.com/science/article/pii/0370269391900028.

F. Weber and N. K. Glendenning. Application of the Improved Hartle Method for the Construction of General Relativistic Rotating Neutron Star Models. *The Astrophysical Journal*, 390:541, May 1992. doi:10.1086/171304.

J.-B. Wei, G. F. Burgio, H.-J. Schulze, and D. Zappalà. Cooling of hybrid neutron stars with microscopic equations of state. *Monthly Notices of the Royal Astronomical Society*, 498(1): 344–354, 06 2020. ISSN 0035-8711. doi:10.1093/mnras/staa1879. URL https://doi.org/10.1093/mnras/staa1879.

L. R. Weih, E. R. Most, and L. Rezzolla. On the stability and maximum mass of differentially rotating relativistic stars. *Monthly Notices of the Royal Astronomical Society: Letters*, 473 (1):L126–L130, 11 2017. ISSN 1745-3925. doi:10.1093/mnrasl/slx178. URL https://doi.org/10.1093/mnrasl/slx178.

S. Weinberg. *Gravitational and Cosmology: Principles and Applications of the General Theory of Relativity*. Wiley, New York, 1972.

C. Wellenhofer, J. W. Holt, and N. Kaiser. Thermodynamics of isospin-asymmetric nuclear matter from chiral effective field theory. *Physical Review C*, 92:015801, Jul 2015. doi:10.1103/PhysRevC.92.015801. URL https://link.aps.org/doi/10.1103/PhysRevC.92.015801.

R. B. Wiringa. Single-particle potential in dense nuclear matter. *Physical Review C*, 38:2967–2970, Dec 1988. doi:10.1103/PhysRevC.38.2967. URL https://link.aps.org/doi/10.1103/PhysRevC.38.2967.

R. B. Wiringa, V. Fiks, and A. Fabrocini. Equation of state for dense nucleon matter. *Physical Review C*, 38:1010–1037, Aug 1988. doi:10.1103/PhysRevC.38.1010. URL https://link.aps.org/doi/10.1103/PhysRevC.38.1010.

J. Xu, L.-W. Chen, B.-A. Li, and H.-R. Ma. Temperature effects on the nuclear symmetry energy and symmetry free energy with an isospin and momentum dependent interaction. *Physical Review C*, 75:014607, Jan 2007a. doi:10.1103/PhysRevC.75.014607. URL https://link.aps.org/doi/10.1103/PhysRevC.75.014607.

J. Xu, L.-W. Chen, B.-A. Li, and H.-R. Ma. Effects of isospin and momentum dependent interactions on liquid–gas phase transition in hot asymmetric nuclear matter. *Physics Letters B*, 650(5): 348 – 353, 2007b. ISSN 0370-2693. doi:https://doi.org/10.1016/j.physletb.2007.05.035. URL http://www.sciencedirect.com/science/article/pii/S0370269307006132.

K. Yagi and N. Yunes. I-love-q: Unexpected universal relations for neutron stars and quark stars. *Science*, 341(6144):365–368, 2013a. doi:10.1126/science.1236462. URL https://www.science.org/doi/abs/10.1126/science.1236462.

K. Yagi and N. Yunes. I-love-q relations in neutron stars and their applications to astrophysics, gravitational waves, and fundamental physics. *Physical Review D*, 88:023009, Jul 2013b. doi:10.1103/PhysRevD.88.023009. URL https://link.aps.org/doi/10.1103/PhysRevD.88.023009.

K. Yagi and N. Yunes. Approximate universal relations for neutron stars and quark stars. *Physics Reports*, 681:1–72, 2017. ISSN 0370-1573. doi:https://doi.org/10.1016/j.physrep.2017.03.002. URL https://www.sciencedirect.com/science/article/pii/S0370157317300492.

K. Yagi, L. C. Stein, G. Pappas, N. Yunes, and T. A. Apostolatos. Why i-love-q: Explaining why universality emerges in compact objects. *Physical Review D*, 90:063010, Sep 2014. doi:10.1103/PhysRevD.90.063010. URL https://link.aps.org/doi/10.1103/PhysRevD.90.063010.

D. Yakovlev and C. Pethick. Neutron star cooling. *Astronomy and Astrophysics*, 42(1):169–210, 2004. doi:10.1146/annurev.astro.42.053102.134013. URL https://doi.org/10.1146/annurev.astro.42.053102.134013.

H. Yasin, S. Schäfer, A. Arcones, and A. Schwenk. Equation of state effects in core-collapse supernovae. *Physical Review Letters*, 124:092701, Mar 2020. doi:10.1103/PhysRevLett.124.092701. URL https://link.aps.org/doi/10.1103/PhysRevLett.124.092701.

S. S. Yazadjiev, D. D. Doneva, and K. D. Kokkotas. Rapidly rotating neutron stars in $\mathcal{R}$-squared gravity. *Physical Review D*, 91:084018, Apr 2015. doi:10.1103/PhysRevD.91.084018. URL https://link.aps.org/doi/10.1103/PhysRevD.91.084018.

Z. Yousaf and M. Z. u. H. Bhatti. Cavity evolution and instability constraints of relativistic interiors. *The European Physical Journal C*, 76:267, Jan 2016. doi:10.1140/epjc/s10052-016-4109-6. URL https://doi.org/10.1140/epjc/s10052-016-4109-6.

J. L. Zdunik, M. Bejger, P. Haensel, and E. Gourgoulhon. Phase transitions in rotating neutron stars cores: back bending, stability, corequakes, and pulsar timing. *Astronomy and Astrophysics*, 450 (2):747–758, 2006. doi:10.1051/0004-6361:20054260. URL https://doi.org/10.1051/0004-6361:20054260.

Y. Zeldovich and I. Novikov. *Relativistic Astrophysics, vol. I.* University of Chigago Press, Chicago, 1978.

N.-B. Zhang and B.-A. Li. Extracting nuclear symmetry energies at high densities from observations of neutron stars and gravitational waves. *The European Physical Journal A*, 55: 39, Mar 2019. doi:10.1140/epja/i2019-12700-0. URL https://doi.org/10.1140/epja/i2019-12700-0.

N. B. Zhang, B. Qi, S. Y. Wang, S. L. Ge, and B. Y. Sun. Keplerian frequency of uniformly rotating neutron stars in relativistic mean field theory. *International Journal of Modern Physics E*, 22(11):1350085, 2013. doi:10.1142/S0218301313500857. URL https://doi.org/10.1142/S0218301313500857.